Tidally- and Wind-Driven Horizontal Flow Patterns on Intertidal Flats in the Wadden Sea

An Assessment using Subgrid Modeling Technique

Reinder Boorsma

TU Delft

Rijkswaterstaat
Ministerie van Infrastructuur en Waterstaat

Nelen & Schuurmans

Tidally- and Wind-Driven Horizontal Flow Patterns on Intertidal Flats in the Wadden Sea

An Assessment using Subgrid Modeling Technique

by

Reinder Boorsma

to obtain the degree of Master of Science
at the Delft University of Technology,
to be defended publicly on April 22nd, 2024

Student number:	4690524	
Project duration:	February, 2023 - April, 2024	
Thesis committee:	Dr. ir. B.C. van Prooijen	TU Delft, chair
	Dr. ir. R.J. Labeur	TU Delft
	Dr. ir. A. Colina Alonso	TU Delft
	Dr. J. de Vries	Rijkswaterstaat
	Dr. N.D. Volp	Nelen & Schuurmans

Cover: Gouwenaar (n.d.)

TU Delft

Rijkswaterstaat
Ministerie van Infrastructuur en Waterstaat

Nelen & Schuurmans

Preface

With this thesis, I conclude my master's in Hydraulic Engineering at Delft University of Technology. This past year of research has helped me realize the true complexity and beauty of the Wadden Sea. I am grateful for the unique opportunity to carry out my research in collaboration with both Rijkswaterstaat and Nelen & Schuurmans. It has been very insightful to get acquainted with these organizations and learn about some of the latest developments in the field.

I would like to take this opportunity to express my sincere gratitude to the entire committee for their continued guidance over the past year. Special thanks to Bram van Prooijen for chairing the committee and offering great insights during the progress meetings. I am grateful to Nicolette Volp and Jurre de Vries for the many sessions in which they provided me with valuable feedback that helped me move in the right direction. I appreciate the constructive feedback of Robert Jan Labeur which helped improve the quality of my research. Thanks to Ana Colina Alonso and Stijn Overmeen for their short-notice availability and great help with problem solving. My gratitude goes out to Ernst Lofvers, Theo Gerkema, and Aditi Mitra for their interest in my work and for their valuable advice.

I am also grateful to my fellow students of the 'masterhok'. We had some fruitful discussion, and our friendly banter about the many hardships of life at times greatly contributed to preserving my sanity. Lastly, I would like to thank my friends and my family (*tige tank!*) for their unconditional support during my career as a student, and for making the past six years a very enjoyable time.

Reinder Boorsma
Delft, April 2024

Abstract

The Wadden Sea is of great ecological importance. This is why it was designated as UNESCO World Heritage Site. Key elements in the Wadden Sea are the extensive intertidal flats. These contain vast amounts of life and serve as feeding grounds for millions of birds. Furthermore, intertidal flats provide ecosystem services such as coastal protection and cycling of nutrients. It follows that it is important to be able to understand and predict how these vital elements of the highly dynamic Wadden Sea change over time. The existence and evolution of intertidal flats rely on the intricate balance between erosion and sedimentation caused by the forcing of wind, waves, and the tide. Exact horizontal flow patterns on intertidal flats are not fully understood, especially under the influence of wind.

This study aims to systematically investigate the tidally- and wind-driven horizontal flow patterns on the scale of an intertidal flat in the western Dutch Wadden Sea. To do so, existing literature is assessed and a subgrid-based hydrodynamic model of the Dutch Wadden Sea is created. A difficulty most hydrodynamic models face when investigating flow patterns on intertidal flats is the cyclic wetting and drying. A wetting-and-drying algorithm is required to resolve the flow patterns near the wet/dry interface. Several types of wetting-and-drying algorithms exist, each with unique advantages and limitations. Subgrid modeling technique does not require a wetting-and-drying algorithm as wetting and drying is automatic, fully resolving flow patterns from the moment of inundation to the moment of drying. The adequacy of using a subgrid-based hydrodynamic model to achieve the aim of the research is investigated through a comparison of simulations with different settings. Computational grid resolutions are manipulated on the scale of the intertidal flat, along with whether subgrid modeling technique is applied. The tidally- and wind-driven horizontal flow patterns are assessed using simulations in which the phase of the spring-neap tidal cycle is manipulated, along with whether wind forcing is applied. These scenarios are applied to two non-fringing intertidal flats with different geometries.

Simulations show that subgrid modeling technique is beneficial for representing the impact of small-scale bathymetric features on the flow pattern while using a coarser computational grid. In the estuarine setting of the western Dutch Wadden Sea and estuaries with similar hydraulic boundary conditions, subgrid modeling technique offers an increase in how well the flow pattern is represented compared to simulations using interpolated bathymetry and the same computational grid resolution. The automatic wetting and drying is crucial for representing shallow flows, especially at depths where measurements and other hydrodynamic models face difficulties. This can help provide insight into the processes that drive flow in the western Dutch Wadden and similar estuaries.

Results indicate that the horizontal flow patterns on intertidal flats follow the water level gradient between surrounding channels and are influenced by the intertidal flat geometry (i.e. size, bed elevation, and degree to which the intertidal flat is intersected by tidal channels), hydraulic boundary condition (i.e. phase of the spring-neap tidal cycle, asymmetry of the tidal wave), and wind forcing (which can completely alter hydrodynamics at several scales).

In absence of wind forcing, flow patterns on intertidal flats follow from water level gradients. Intertidal flats cyclically inundate during flood and dry during ebb. This leads to a maximum of four peaks in absolute velocity per tidal cycle, of which two follow from physics on the scale of an intertidal flat and two from the basin-scale tide. There is a phase difference between the High Water slack tide on the intertidal flat and in the surrounding channels. If the intertidal flat is intersected by channels and/or the bed elevation is low, no significant water level difference builds up in the channels surrounding the intertidal flat, and flow follows the basin-scale water level gradient. If intersecting channels are absent and/or the bed elevation is high, a water level difference can build up. Once water levels exceed the intertidal flat elevation such that a water level gradient is established, flow follows the gradient. The size of the intertidal flat influences the magnitude of the water level gradient and thereby flow velocities. Tidal asymmetry seems to increase from relatively symmetrical in time during neap tide to asymmetrical

during spring tide. The phase of the spring-neap tidal cycle affects the rising and falling rates of the tide. This impacts water level gradients and thereby flow velocities.

Unidirectional wind forcing of 15 m/s both from the east and the west alters the hydrodynamics on several scales. On the scale of an intertidal flat, wind shear accelerates flow in the wind direction and decelartes flow opposite the wind direction, resulting in a substantial shift in how water enters and leaves the intertidal flat. Furthermore, wind has a depth-dependent impact on flow patterns at the intertidal flat. Compared to the situation without wind forcing, the flow pattern on the upper intertidal flat is completely altered, and the flow pattern on the lower intertidal flat is substantially altered. The combination of basin-scale water level set-up or set-down with wind shear on the scale of an intertidal flat causes a large spatial variability in exposure times.

This report contributes to the knowledge on horizontal flow patterns on intertidal flats, benefiting studies into ecology, navigational maintenance, flood protection, and the ability of intertidal flats to keep up with sea level rise. While the flow pattern plays a significant role, it is not solely responsible for morphological change. Moving forward, continued research into the drivers of the morphological change of intertidal flats will be crucial for informed management of ecologically valuable estuarine areas like the Wadden Sea.

Contents

Nomenclature

Abbreviations

Abbreviation	Definition
AT	Average Tide (model scenario)
EW	Easterly Wind (model scenario)
GBO	Grienderwaard - Ballastplaat - vlakte van Oosterbierum (intertidal flats complex)
HR	Higher-Resolution (model scenario)
HW	High Water
IB	Interpolated Bathymetry (model scenario)
LW	Low Water
NAP	Normaal Amsterdams Peil (Dutch Ordnance Datum)
NT	Neap Tide (model scenario)
ST	Spring Tide (model scenario)
WW	Westerly Wind (model scenario)

Glossary

Term	Definition
Morphology	Shape and structure of a coastal system.
Tidal basin	Coastal subsystem. Fills and empties with water as the tide rises and falls.
Intertidal flat	Morphological element of a tidal basin which periodically wets and dries.
Tidal channel	Moderate to large channel characterized by bidirectional tidal flow. These surround intertidal flats and in some cases intersect them.
Tidal gully	Element of the intertidal flat which plays a role in drainage. Has a smaller size than the tidal channel.
Intertidal flat geometry	Shape of the intertidal flat: size, elevation, and degree to which the intertidal flat is incised by tidal channels and gullies.

1

Introduction

1.1. Background

The Wadden Sea, extending from the Netherlands to Denmark, is the largest connected area in the world that is covered by intertidal flats (Reise et al., 2010). A map of this area is shown in Figure 1.1. Barrier islands, tidal channels, intertidal flats, gullies, and salt marshes are visible. Due to the uniqueness of its physical system and its value to ecology, the Wadden Sea was designated as a UNESCO World Heritage Site in 2009. It hosts around 5,000 species of flora and fauna (UNESCO World Heritage Centre, n.d.). Around 10-12 million migratory birds per year feed in the Wadden Sea (Reise et al., 2010). Therefore, the ecological importance of the Wadden Sea extends beyond its boundaries (Reise et al., 2010; UNESCO World Heritage Centre, n.d.).

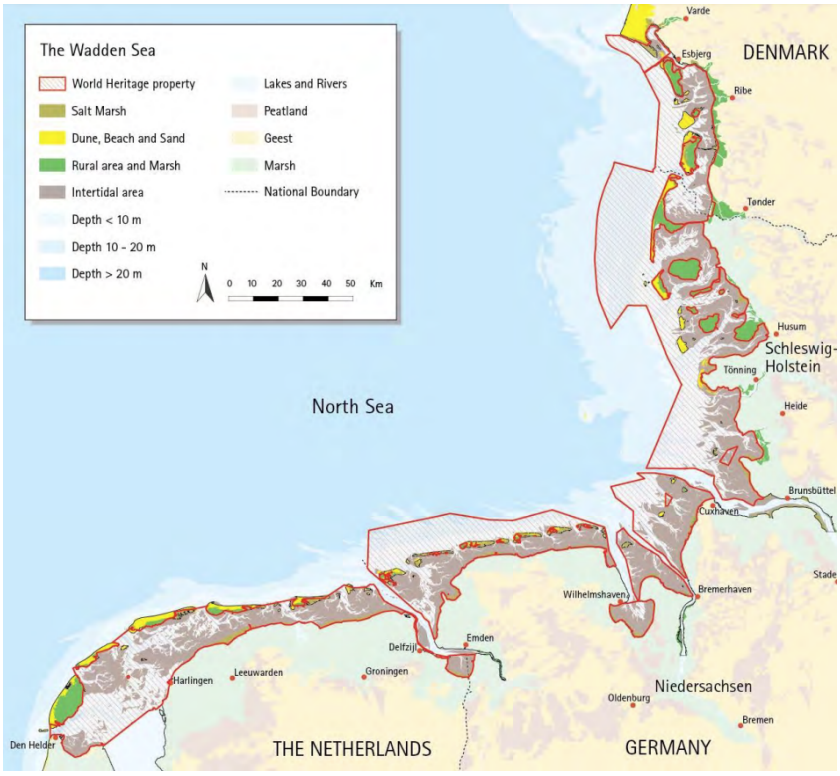

Figure 1.1: Overview of the Dutch, German, and Danish Wadden Sea (Common Wadden Sea Secretariat, 2016).

The Wadden Sea system is highly dynamic. It is affected by sea level rise, changing climate conditions, and human pressures. Water flow on the system scale is driven by wind and tidal forcing (Duran-Matute et al., 2014). In addition to these forcing mechanisms, freshwater influx affects the flow on the scale of channel-shoal systems. In response to the flow, sand and mud are transported. The closures of the Zuiderzee in 1932 and the Lauwerszee in 1969 increased the tidal range and induced morphological changes in the Dutch Wadden Sea (Bosboom & Stive, 2021). The morphodynamics and hydrodynamics in the western Dutch Wadden Sea are still adapting to the Zuiderzee closure (Grasmeijer et al., 2022). Of all morphological elements in the Wadden Sea, Wang et al. (2012) suggest that the least knowledge exists on the intertidal zone.

Intertidal flats

The intertidal zone is the area located between the highest and lowest tidal water levels. This zone is inundated as the tide enters the Wadden Sea and exposed as the tide recedes. The intertidal zone is characterized by intertidal flat complexes. These house a considerable mass of benthic and microbial lifeforms (Heip et al., 1995), which are an important food source for birds (Piersma et al., 1993). Intertidal flat complexes may provide several ecosystem services. These include coastal protection through sediment stabilization, improvement of water quality, and cycling of nutrients (Coen et al., 2007; Hope et al., 2020; Paterson et al., 2009).

Because of their key role in the Wadden Sea system, it is important to understand how intertidal flats change over time. As flow in the Wadden Sea system as a whole is highly dynamic, the morphology of intertidal flats is also highly dynamic. The existence and evolution of intertidal flats rely on an intricate balance between erosion and sedimentation caused by hydrodynamic forcing. Erosion exceeding sedimentation and/or sea level rise can lead an intertidal flat to 'drown' and disappear (van Goor et al., 2003). A lot of work has been done on the drowning of intertidal flats (e.g. Huismans et al. (2022)). The detailed flow patterns on intertidal flats, however, have only been studied to a limited extent. Insights into the detailed flow patterns on intertidal flats are required to understand how they affect the ecology, as well as to improve the understanding on the morphological change of intertidal flats.

Wind forcing is an aspect that cannot be ignored when analyzing flow patterns on intertidal flats. Two studies investigated the impact of wind on the horizontal flow patterns on a single intertidal flat in the Eastern Scheldt (de Vet et al., 2018) and western Dutch Wadden Sea (Colosimo et al., 2020). These studies found that compared to the direction of the tidal current, wind forcing can substantially alter the direction of currents on intertidal flats. If tidal velocities are small, wind can even reverse the flow direction with respect to the tidal current flow direction. Duran-Matute et al. (2016) found that on the scale of the western Dutch Wadden Sea, wind is the main driver of tide-averaged volume transport through tidal inlets. This indicates that wind plays an important role in steering the system-scale hydrodynamics. These studies confirmed that wind has a substantial effect on flow patterns both on intertidal flats and on the scale of the western Dutch Wadden Sea. How wind forcing impacts the detailed flow patterns on intertidal flats is a knowledge gap.

Process-based hydrodynamic models

To gain insight into the flow patterns on intertidal flats (and how wind affects these), process-based hydrodynamic models can be used. These models encounter several difficulties in simulating flow patterns on intertidal flats. The limited availability of water level and velocity measurements in the intertidal zone complicates setting up a model with valid hydrodynamics on intertidal flats. The cyclic wetting and drying of intertidal flats creates an additional issue. Wetting-and-drying algorithms are required to resolve flow patterns near the wet-dry interface (Medeiros & Hagen, 2013). Subgrid modeling technique does not face this difficulty, as wetting and drying is automatic (Casulli, 2009). This technique takes into account bathymetric information with a higher resolution than the computational grid resolution by using a subgrid. This provides the additional benefit of capturing the interaction of small-scale geometric features with the flow.

1.2. Problem statement

Several aspects of flow on intertidal flats have been studied. However, no previous research has systematically assessed the detailed horizontal flow patterns on the scale of an intertidal flat and how these are influenced by wind forcing. It is important to assess these flow patterns for their effect on intertidal flat ecology and because they force the morphological evolution of intertidal flats. An important aspect in addressing the research gap is the method typically applied to study flow patterns on intertidal flats: process-based hydrodynamic models. These encounter several difficulties in investigating horizontal flow patterns on intertidal flats, including the handling of wetting and drying and the difficulties with validating model outcomes. Subgrid modeling technique can address some of the difficulties in investigating flow patterns on intertidal flats, as this method automatically handles wetting and drying and does not neglect small-scale geometric feature. As of yet, no validated subgrid-based hydrodynamic model of the Dutch Wadden Sea exists.

1.3. Research questions

This study seeks to systematically assess the detailed horizontal flow patterns on the scale of an intertidal flat. To do so, a subgrid-based hydrodynamic model of the Dutch Wadden Sea is created. The subgrid-based hydrodynamic model is applied to explain the mechanisms that cause horizontal flow patterns on intertidal flats, and how horizontal flow patterns are affected by wind forcing. The following research questions are posed:

'What determines the horizontal flow patterns on intertidal flats in the western Dutch Wadden Sea, and how does wind influence these flow patterns?'

Sub-question 1: *How adequate is the subgrid modeling technique for capturing the interaction between higher-resolution bathymetry and flow compared to higher-resolution models without subgrid modeling technique?*

Sub-question 2: *What are the tidally-driven horizontal flow patterns on intertidal flats, and how do they develop within a tidal cycle and over the duration of a spring-neap cycle?*

Sub-question 3: *How does varying wind forcing impact horizontal flow patterns on intertidal flats?*

1.4. Methodology

This study aims to systematically assess the detailed horizontal flow patterns on the scale of an intertidal flat. To do so, existing knowledge on the tidally- and wind-driven flow patterns on intertidal flats is assessed through a literature review (chapter 2). A subgrid-based hydrodynamic model of the Dutch Wadden Sea is created (chapter 3). The skill of the model in simulating flow patterns on intertidal flats is investigated. To gain insight into the identified knowledge gaps, model scenarios are formulated in which the following factors are manipulated: computational grid resolution, whether subgrid modeling technique is applied, phase of the spring-neap tidal cycle, and whether wind forcing is applied (chapter 4). The model scenarios are applied to two intertidal flat complexes with different geometries. The adequacy of using subgrid modeling technique to represent flow patterns on intertidal flats is assessed (chapter 5), and analyses are performed on the model results to identify the tidally- and wind-driven flow patterns on intertidal flats (chapter 6). Findings are synthesized, discussed, and implications of findings are stated (chapter 7). Finally, conclusions are drawn and recommendations are formulated (chapter 8).

2

Literature review

In this chapter, the study area of the Dutch Wadden Sea is further described. Insights from the literature on tidally- and wind-driven flow patterns on intertidal flats are provided. It is described how process-based models can be used to provide an overview of flow patterns on intertidal flats, and the issue that these models face when handling wetting and drying is presented. The subgrid modeling technique that does not face this issue is introduced, and its validity for estuarine application is discussed.

2.1. Study area

The Wadden Sea is a multiple tidal inlet system that consists of the following large-scale morphological elements: barrier islands, ebb-tidal deltas, tidal inlets, and tidal basins. Water enters and exits tidal basins through tidal inlets. Where tidal basins border each other, there is a tidal divide. This is a line over which minimal exchange of water occurs. An overview of the Dutch Wadden Sea is given in Figure 2.1, along with indicative locations of tidal divides. This study focuses on the western Dutch Wadden Sea, which consists of the Marsdiep, Eijerlandse gat, and Vlie basins.

Figure 2.1: Overview of the Dutch Wadden Sea. Names of tidal basins and indicative tidal divides are shown. Adapted from European Union (2024).

Within tidal basins, there is a subtidal zone (always inundated), and an intertidal zone (temporarily inundated over the tidal cycle). Key morphological elements in the intertidal zone are intertidal flats. There is a difference between fringing intertidal flats, which are connected to the coast, and non-fringing intertidal flats. Most of the literature focuses on fringing intertidal flats. Fringing intertidal flats develop

in response to waves and the tide. They retreat due to ebb-dominance (Pritchard et al., 2002) and waves (Friedrichs, 2011), whereas the tide (Friedrichs, 2011) and abundant sediment supply (e.g. from a river; Yang et al. (2008)) cause accretion. How most of these mechanisms interact with the intertidal flat is not dependent on the presence of a coast. Thus, it is assumed that most mechanisms can be extended to non-fringing intertidal flats. The flow pattern, on the other hand, does differ. Due to the absence of a closed coastal boundary, the flow pattern on non-fringing intertidal flats (and its effect on morphology) differs from that of fringing intertidal flats.

2.2. Flow patterns on intertidal flats

Flow in the Wadden Sea is driven by the tide, wind, waves, and to some degree by baroclinic forcing. In the following paragraphs, flow patterns and the boundary conditions that affect these are schematized for a conceptual non-fringing intertidal flat in a tidal basin. The intertidal flat is indicated in beige, with surrounding channels indicated in blue. Surrounding intertidal areas are not shown. The tidal inlet is located to the north and the coast is located to the south. Therefore, the flood tide enters from above and the ebb tide leaves in the same direction. Currents are indicated in blue.

The general pattern of inundation and drying of intertidal flats is schematized in Figure 2.2. As the water levels in the channels around the intertidal flat rise, the intertidal flat inundates evenly from all sides (Figure 2.2a). As water levels in the tidal channels around the intertidal flat drop, drying occurs evenly (Figure 2.2b). In the final stages of drying, flow concentrates in gullies (Figure 2.2c).

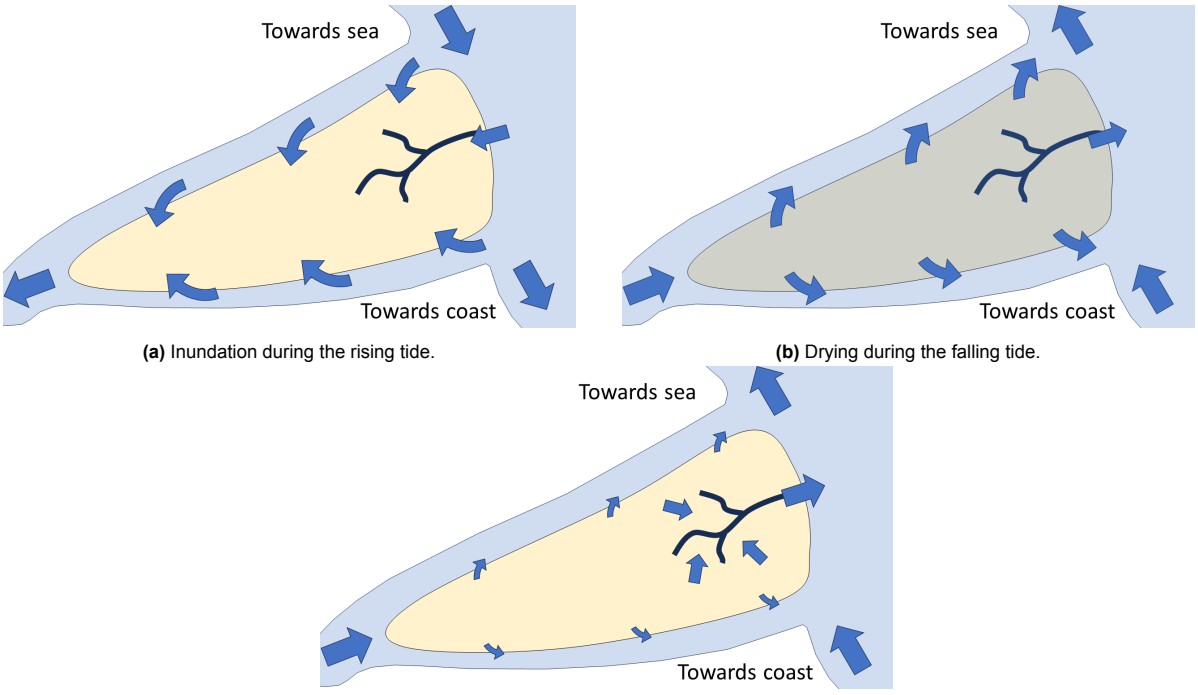

(a) Inundation during the rising tide.

(b) Drying during the falling tide.

(c) Drying during the last stage of the falling tide. Flow concentrates in gullies.

Figure 2.2: The cycle of inundation and drying on an intertidal flat.

De Vet et al. (2018) studied the non-fringing Roggenplaat in the Eastern Scheldt. This intertidal flat has shoal-like geometry. The extent to which tidal channels and gullies intersect the intertidal flat is low. The hydraulic conditions in the Eastern Scheldt and Wadden Sea are somewhat comparable, as they have a comparable tidal range, water depths, and wind climate. Bathymetry differs, as the degree to which intertidal flats in the Wadden Sea are intersected by tidal channels and gullies is generally higher than at the Roggenplaat. Thus, findings based on the Roggenplaat can be extended only to some degree to the intertidal flats in the Wadden Sea. De Vet et al. (2018) found that while geometrical features

are important for local flow patterns on the intertidal flat, the net flow direction over the intertidal flat does not result from geometrical features on the intertidal flat. The effect that geometrical features such as humps and gullies had on flow patterns on intertidal shoals like the Roggenplaat is schematized in Figure 2.3. The hump and gully alter flow locally, on a smaller scale than the intertidal flat scale.

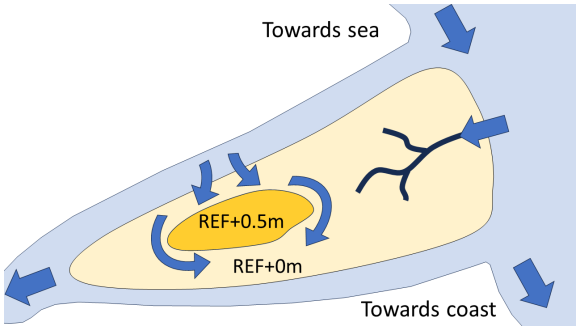

Figure 2.3: The effect of geometrical intertidal flat features on tidally-driven flow patterns on an intertidal flat.

2.2.1. Tide

In absence of meteorological forcing, the tide drives flow over intertidal flats by creating water level gradients over intertidal flats. De Vet et al. (2018) state that water level gradients over intertidal flats originate from two sources: spatial differences in tidal water levels (Figure 2.4a), and a spatial difference in the timing of the tide in surrounding channels (Figure 2.4b). At the Roggenplaat, spatial differences in tidal water levels caused water level gradients. Due to the different geometries of intertidal flats in the Wadden Sea, the cause of water level gradients may differ.

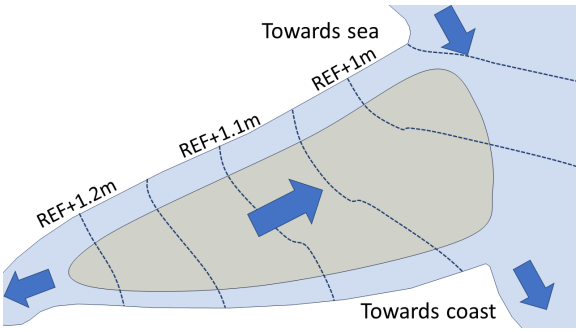

(a) Net flow induced by a spatial difference in water levels.

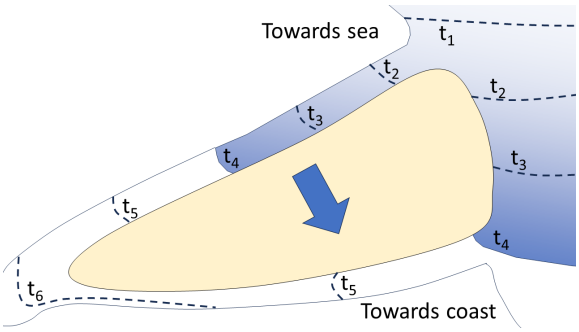

(b) Net flow induced by a spatial difference in the timing of the tide.

Figure 2.4: The two tidally-driven mechanisms generating water level gradients over an intertidal flat.

The spring-neap tidal cycle affects the tidal range and therefore the rate at which the water level rises. The effect on the general pattern of inundation and drying of intertidal flats is hypothesized. Due to an increase in flood water levels, higher intertidal flat elevations inundate during spring tide only. Conversely, lower intertidal flat elevations dry only during the lower ebb water levels. Due to the lower tidal range during neap tide, lower elevations remain inundated during ebb while higher elevations do not inundate during flood. For an intertidal flat on which net flow is driven by water level gradients (Figure 2.4a), discharge over the intertidal flat is proportional to the High Water (HW) level (de Vet et al., 2018).

As the tidal wave propagates from deep water into (relatively) shallow water, the water level signal of the tidal wave can become asymmetrical in time (phase) and space (tidal amplitude). Two important causes are continuity and bottom friction (Bosboom & Stive, 2021). According to the continuity equation, the tidal wave propagates at celerity $c = \sqrt{gH}$ (in which g is gravitational acceleration and H is water depth), implying different celerities during high and low tide. Similarly, the relative importance of friction is larger when water depths are small and smaller when water depths are larger. This also implies a distortion of the tidal signal. Asymmetries in tidal amplitudes translate to asymmetries in ebb and flood velocities.

These are important for tidally-averaged sediment transport of coarse sediments. Asymmetries in time affect the duration of Low Water (LW) and HW slack periods, during which fine sediments can settle. Due to their effect on velocities over the tidal cycle, tidal asymmetries are likely to induce a net tidally-averaged sediment transport over the intertidal flat (Le Hir et al., 2000), thereby inducing morphological change.

2.2.2. Wind and waves

Wave energy from the North Sea barely enters the Wadden Sea, as most wave energy is dissipated on the ebb-tidal deltas (Oost et al., 2017) or barrier islands. Waves in the Wadden Sea are therefore mostly limited to smaller, locally generated waves. Findings from Le Hir et al. (2000) and Hunt et al. (2015) indicate that wind-driven circulation can substantially alter the hydrodynamic regime both in an entire estuary and within the intertidal zone. Therefore, the role of wind-driven currents should be considered when assessing the flow patterns on intertidal flats.

Wind impacts the flow patterns at different scales. When wind is directed towards a coast, water is pushed up against the coast. This leads to basin-scale water level set-up, or set-down for wind directed from the coast. Duran-Matute et al. (2016) show in the western Dutch Wadden Sea that westerly wind of 13 m/s causes a water level set-up of up to 1.3m near the coast, while an easterly wind of 13 m/s causes water level set-down of up to 0.7m. Water level set-up and set-down affect the water level gradients that drive the flow over intertidal flats (Figure 2.5a).

On the scale of the intertidal flat, wind shear causes an additional impact on the flow pattern. De Vet et al. (2018) approximated with a simplified momentum equation that wind velocities of a factor 40 times the tidal velocities on an intertidal flat significantly alter the horizontal flow patterns on the intertidal flat (Figure 2.5b). The significant effect of wind on horizontal flow patterns is confirmed by the research of Colosimo et al. (2020), who formulated a tide-wind interaction model to predict wind-driven reversal of the tidal current. They found that wind is most effective at altering flow patterns when tidal velocities are smallest. De Vet et al. (2018) and Colosimo et al. (2020) focused on the effect of wind compared to tidal velocities. However, the impact of wind also varies with water depth. As water depths decrease, the impact of wind on flow patterns increases. How wind forcing impacts the detailed flow patterns on intertidal flats is a knowledge gap.

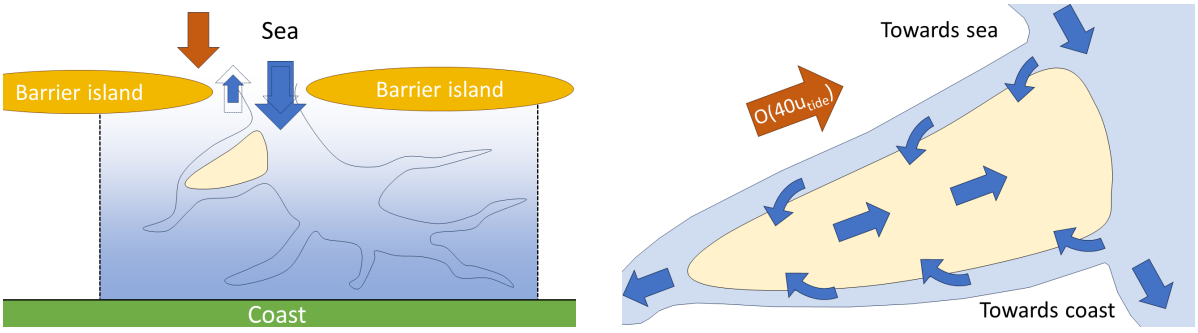

(a) Wind-driven water level set-up in a tidal basin.

(b) Local wind-driven currents dominate tidal currents.

Figure 2.5: The effect of wind on flow patterns on an intertidal flat and on the water level gradients that drive these. Wind direction indicated in orange.

2.3. Modeling flow on intertidal flats

To gain insight into flow on intertidal flats, process-based models can be used. Examples of process-based models that have been used in the Dutch Wadden Sea are Delft3D (e.g. Jordan et al. (2021) and van Weerdenburg et al. (2021)), and the General Estuarine Transport Model (GETM) (e.g. Duran-Matute et al. (2014) and Gräwe et al. (2016)). Process-based models aim to reproduce reality by numerically solving equations that represent water flow, and in which all relevant physical processes are encapsulated. There are several challenges in accurately modeling flow on intertidal flats with process-based models when small length scales are of interest.

In process-based models, higher-resolution bathymetric data is traditionally averaged to the resolution of the computational cell. In doing so, small-scale bathymetric features such as small gullies and humps are neglected. Gullies are sharp incisions with steep walls, while humps have gentler gradients. Therefore, the errors between actual bathymetry and averaged bathymetry are most notable for gullies. As gullies are important in conveying discharge, especially during the drying of intertidal flats (Figure 2.2c), neglecting small-scale geometric features of intertidal flats likely causes a systematic bias in which discharges are underestimated. A knowledge gap is the exact effect of averaging of higher-resolution bathymetric data to lower resolutions on simulated flow patterns.

The wet-dry interface poses a discontinuity which changes its position at subsequent timesteps. In process-based models, it can be computationally demanding to accurately track the wet-dry interface. On top of this, concerns regarding the conservation of mass and numerical stability play a role. There are Lagrangian and Eulerian wetting-drying approaches, with Eulerian approaches being more attractive for practical implementations because of their fixed mesh (Funke et al., 2011). Eulerian wetting-and-drying algorithms can be divided into four groups: thin film, element removal, depth extrapolation, and negative depth (Medeiros & Hagen, 2013). Table 2.1 gives an overview of the strengths and weaknesses of these methods. It is apparent that there is no single 'best' one when handling wetting and drying. When dealing with wetting and drying, subgrid modeling technique does not encounter these issues.

Table 2.1: Overview of pros and cons of different wetting-and-drying algorithms. Good performance is indicated in green, orange indicates room for improvement or conditionally good performance. Synthesized from Candy (2017), Le et al. (2020), and Medeiros and Hagen (2013)

Algorithm	Mass conservation	Accuracy	Robustness	Computational efficiency
Thin film	Correction required	Changes physics through fictitious water layer; accurate results	-	Larger domain
Element removal	Model-dependent	-	Good if: • High temporal resolution • High spatial resolution • Slow movement of wet-dry interface	Possibly slower to ensure numerical stability
Depth extrapolation	Often good; model-dependent. Correction required	Some artificial wetting	-	Minimal extra computational time due to corrections
Negative depth	Good if slow movement of wet-dry interface	Good if slow movement of wet-dry interface	-	Larger domain

2.3.1. Introduction to subgrid modeling technique

Subgrid modeling technique uses a high-resolution subgrid for bathymetric information while keeping a coarse computational grid. The water level is typically assumed to be uniform in a computational cell in depth-averaged hydrodynamic models. This assumption is also applied in subgrid-based models. As small-scale bathymetric features are important for detailed flow patterns (Figure 2.3), subgrid modeling technique is a way to incorporate these into coarse computational grids instead of averaging them out. In this way, the effect that small-scale spatial variations in bathymetry have on flow patterns on the scale of a computational cell can be taken into account. Results for coarse meshes and large time steps are still accurate (Casulli, 2009). This shifts the basis on which computational cell size should be chosen from small enough to accurately represent the bed to small enough to accurately reproduce flow phenomena on the scale in which the researcher is interested.

By allowing a non-uniform bed level per computational cell, the relationship between water level and volume in a computational cell (Figure 2.6) becomes non-linear. The resulting system of equations for water surface elevation becomes (mildly) non-linear. By solving this non-linear system of equations using a Newton iteration, wetting and drying is automatically resolved (Casulli, 2009). Therefore, no wetting and drying algorithm, which could introduce inaccuracies or decrease computational efficiency, is needed. A further assumption is that the cross-section through which water exchanges between adjacent computational cells is based on subgrid elevations where cells border each other. Lastly, it is

assumed there is a surface with friction, such as the seabed or riverbed. Subgrid modeling technique differs from non-subgrid models only when subgrid bottom elevations vary within a computational cell (or when automatic wetting and drying plays a role). In the limit, for a computational cell with large water depth in which bed level variations are thus relatively small, or for a single subgrid cell in a computational cell, model outcomes in a subgrid model are the same as outcomes of non-subgrid models.

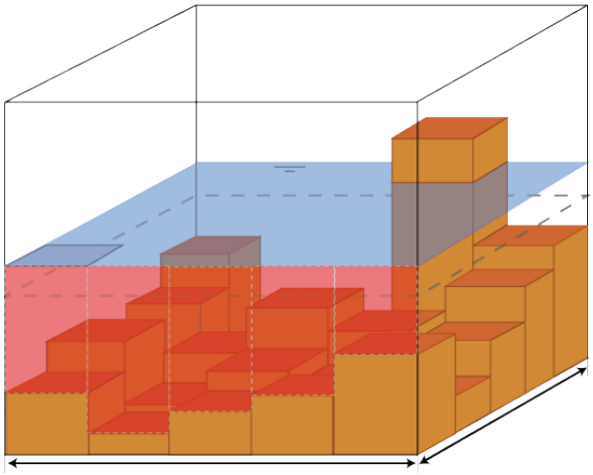

Figure 2.6: Subgrid modeling concept. Adapted from Nelen & Schuurmans (n.d.-a).

2.3.2. Subgrid modeling technique as described in Volp et al. (2013)

The subgrid method as described in Volp et al. (2013) takes into account small-scale variations in bed roughness and velocities by estimating subgrid-scale velocities. This estimation results in a 'friction depth'. Through the friction depth, variations in roughness and velocity at subgrid resolution are taken into account in calculations on the computational grid resolution. The discretization of the momentum balance in Volp et al. (2013) is detailed in Appendix A. Key assumptions are summarized in the following paragraphs.

Volp et al. (2013) establish a relationship between velocities on the subgrid scale and the velocity on the scale of the quarter momentum domain. To do so, a uniform flow direction is assumed within the quarter momentum domain. The consequence is that internal circulations, convergence, and divergence are excluded within the quarter momentum domain. Furthermore, a uniform friction slope is assumed:

$$S = \frac{c_f u_p^2}{gH} = uniform \tag{2.1}$$

with:

S	friction slope	[-]
c_f	bottom friction	[-]
u_p	subgrid-scale flow velocity	[m/s]
H	water depth	[m]

As the friction slope equals the water level gradient and bed slope in case of steady flow, the assumption has a physical basis. It is an assumption about the structure of the flow based on the relative importance of friction. When friction is dominant, this assumption plays a large role in converting subgrid scale velocities to the velocity on the quarter momentum domain scale. When the relative importance of friction decreases, the influence of this assumption decreases as well. In the limit, for marginal importance of friction, the system of equations that describes the water movement reduces to the same system of equations used in non-subgrid hydrodynamic models. The assumption of a uniform friction slope is then as good as the assumption of a uniform velocity within a computational cell.

Discharges between neighboring momentum domains are based on water depth and friction. Again, a uniform friction slope is assumed to calculate discharges between momentum domains. As before, the assumption plays a large role in calculating discharges between momentum domains when friction is dominant but plays a smaller role when the relative importance of friction decreases.

To prevent wind from accelerating thin water layers to unphysical velocities, creating numerical instabilities, extra momentum losses are introduced through the correction factor χ. This factor has not been validated. The formulation for χ is mathematically grounded in physics as it relates to the critical velocity $\sqrt{gH}$, which is the maximum velocity at which waves propagate linearly.

2.3.3. Validity of subgrid modeling technique for estuarine application

Subgrid modeling technique was created for application in estuarine settings. Therefore, subgrid modelling technique has been applied in a large variety of estuarine settings: the Venice Lagoon (Casulli & Stelling, 2011), Elbe estuary (Sehili et al., 2014), San Francisco Bay (MacWilliams et al., 2016), Delaware Bay (Wu et al., 2016), Western Scheldt (Volp, 2017), and Buttermilk Bay (Kennedy et al., 2019). In all studies, model results obtained using a subgrid were compared with results obtained using averaged bed elevations and a higher-resolution computational grid. All noted similar accuracy and lower computational cost. Sehili et al. (2014) is the only study to compare the automatic wetting and drying with the wetting and drying of a non-subgrid model, observing more accurate wetting and drying. The widespread use, favorable computational efficiency compared to non-subgrid models, and accurate wetting and drying imply that subgrid modeling technique is an adequate tool for estuarine application.

Kennedy et al. (2019) note a limitation to subgrid modelling technique as implemented in Volp et al. (2013). They applied formal averaging to the subgrid equations used in previous studies and proposed several closures for the additional terms this gave rise to. They noted that closures which use assumptions about the flow structure (e.g. Volp et al. (2013)) work well for flow parallel to depth contours, but lower accuracy is expected for flow perpendicular to depth contours. This should be taken into account when interpreting results.

An important assumption in the spatial discretization of the bottom friction term as in Volp et al. (2013) is the uniform flow direction per quarter momentum domain. This highlights that coarse simulations with subgrid modeling technique are an improvement to coarse grid simulations, not a replacement for fine grid simulations. Therefore, when using subgrid as described in Volp et al. (2013) to study flow patterns in the intertidal zone, the computational cell size should be small enough to accurately capture the length scales of the physics the researcher is interested in. In spatially discretizing the bottom friction and advection terms, Volp et al. (2013) assume a uniform friction slope. The assumption has a physical basis, but caution should be exercised when interpreting simulated flow patterns, as they result to some degree from this assumption.

2.4. Concluding remarks

There are gaps in the knowledge on horizontal flow patterns on intertidal flats, especially under the influence of wind forcing. To circumvent some of the difficulties of modeling flow with process-based models, subgrid modeling technique can be used. It has the benefits of automatic wetting and drying and the capability to take into account higher-resolution bed information while calculating on a coarser grid. While subgrid modeling technique can provide benefits, it is based on assumptions. These are important to consider when analyzing model results. It is not yet known how simulated flow patterns *on intertidal flats* using subgrid modeling technique compare to those without using subgrid modeling technique. This aspect requires further investigation.

3

Model setup

A subgrid-based hydrodynamic model was set up in the 3Di hydrodynamic subgrid modeling software. Before formulating the scenarios as specified in section 1.4, the model set-up is presented and the model performance is tested.

3.1. Data overview

Relevant data for setting up the hydrodynamic model of the Dutch Wadden Sea are bathymetric data, boundary conditions, freshwater discharge, and meteorological data. To assess the model performance, water level and/or velocity measurements data is required during the simulated period. Table 3.1 shows an overview of the used data. The bed level of the Dutch Wadden Sea and Ems-Dollard is measured in cycles of six years, with a single tidal basin being measured per year. This dataset is called the Vaklodingen dataset (Rijkswaterstaat, 2023). Rijkswaterstaat provided the Vaklodingen data for the most recent available years of 2017 to 2022. Offshore bathymetric data was supplemented with data used in the KRW Slib model (Vroom et al., 2020), such that the hydrodynamic boundary conditions of the KRW Slib model could be used. The exact resolution of this bathymetric dataset varies, as it is expressed in longitude and latitude.

Table 3.1: Overview of data (with sources) used in model setup, calibration, and validation.

Data	Resolution		Source
	Spatial	**Temporal**	
Wadden Sea and Ems-Dollard bathymetry	20mx20m	-	Rijkswaterstaat, Vaklodingen
North Sea bathymetry	Shallow: ca. 450mx450m[1] Deep: ca. 900mx900m[1]	-	Deltares (Vroom et al., 2020)
Water level boundary conditions	North: ca. 1650m[1] East: ca. 950m[1] South: ca. 850m[1] West: ca. 1850m[1]	10 min	Deltares (Vroom et al., 2020) Originates from Dutch Continental Shelf Model (Zijl et al., 2018)
Freshwater discharge	-	10-15 min	Deltares (Vroom et al., 2020)
Meteorological data	-	1 hour	Theo Gerkema[2]
Water level measurements	-	10 min	Rijkswaterstaat

[1]Depends on longitude, latitude.
[2]Methodology described in Gerkema and Duran-Matute (2017). Updated dataset includes 2019.

Rijkswaterstaat keeps track of water levels at several measuring stations in and around the Wadden Sea. Ten measuring stations in and around the western Dutch Wadden Sea were used for calibration and validation purposes (Figure 3.1). The K14 platform near the edge of the model domain was used to assess the quality of the boundary condition. The water level dataset contained multiple entries at several points in time. It was not possible to determine which water level occurred in reality at these points in time. The first value in the dataset was retained and additional values were discarded. Interpolation was applied to fill missing values.

Figure 3.1: Locations and names of measuring stations in the western Dutch Wadden Sea, and the K14 platform. Adapted from Google (n.d.).

3.2. Model setup

The chosen domain includes Dutch the Wadden Sea, Ems-Dollard, and part of the North Sea. The model reference coordinate frame is expressed in Rijksdriehoeks (RD) coordinates. The bathymetric data in the Dutch Wadden Sea and Ems-Dollard has a resolution of 20mx20m (Table 3.1). To be able to use the boundary conditions from the KRW Slib model (Vroom et al., 2020), the model domain was expanded to include part of the North Sea and the western German Wadden Sea. As the KRW Slib model reference coordinate frame is expressed in longitude and latitude, transferring bathymetric data of the KRW Slib model to the present model introduces curvature. To better align the bed with the square computational grid, extrapolation is applied such that the edges of the model are straight in an RD coordinate system. The full data processing procedure applied to the Digital Elevation Model (DEM) is described in Appendix B. An overview of the bed after data processing is given in Figure 3.2.

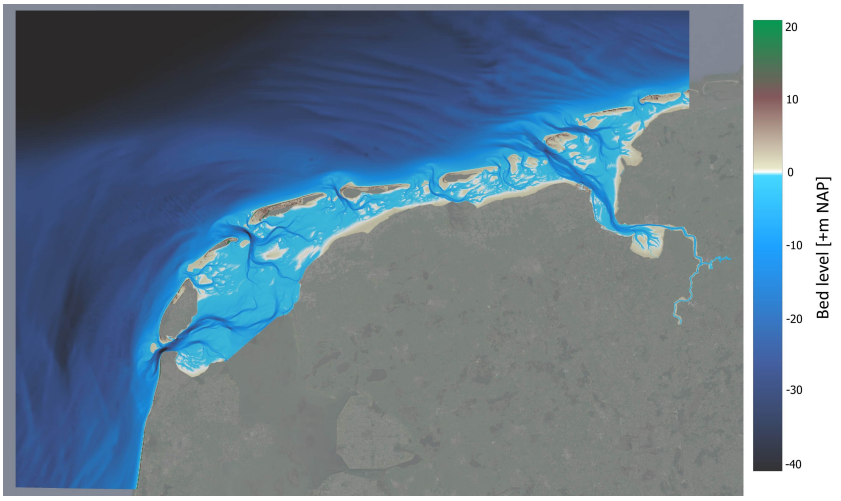

Figure 3.2: Overview of bed levels throughout the model domain. Background from Google (n.d.).

Computational grid

In Appendix C, the convergence of model outcomes using different grid resolutions is analyzed. Based on these findings, the grid resolution before applying scenario-dependent grid refinement was chosen. As shown in Figure 3.3, the resolution ranges from 640mx640m in the western Dutch Wadden Sea to 2560mx2560m in areas farther from selected intertidal flats. There is some exchange of water between the western Dutch Wadden Sea and the area east of the Terschelling tidal divide (Duran-Matute et al., 2016). As this area is relevant but of secondary importance for flow in the western Dutch Wadden Sea, a resolution of 1280mx1280m was determined appropriate for the region between the Terschelling and Schiermonnikoog tidal divides. Because of the quadtree algorithm (Stelling, 2012) in 3Di, computational cells can only border cells half or double their size. Therefore, instead of directly bordering the cells of 2560x2560m, areas of 640x640m cells are padded by cells of 1280mx1280m, which can then border the 2560mx2560m cells. The bed level subgrid has a 20mx20m resolution in all computational cells.

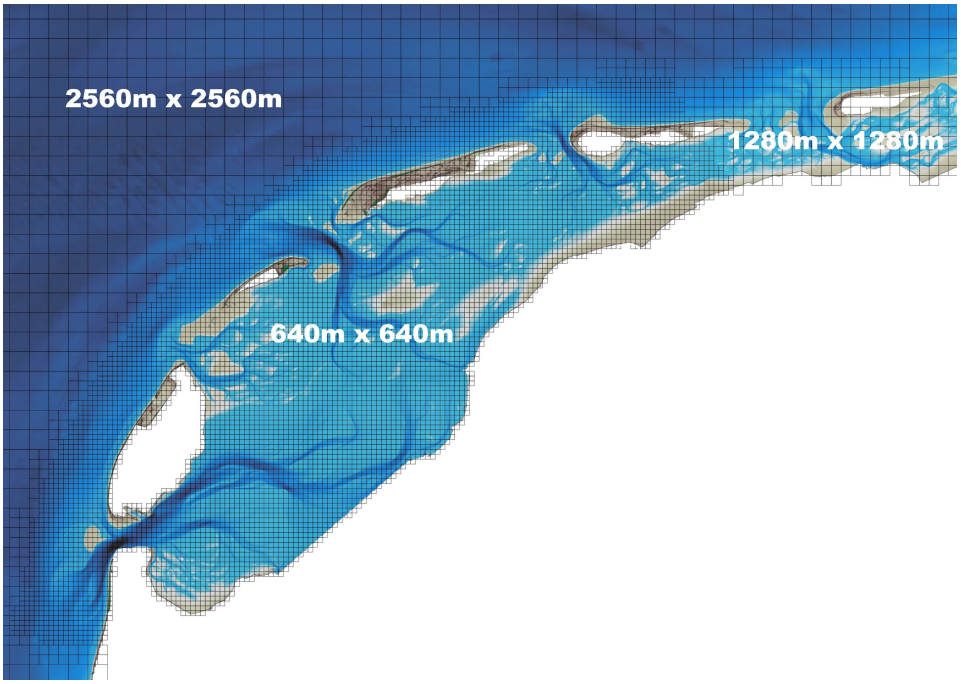

Figure 3.3: Computational grid throughout the part of the model domain including and surrounding the western Dutch Wadden Sea; before scenario-dependent grid refinement.

Boundary conditions

Boundary conditions of the KRW Slib model were used, as these boundary conditions are located sufficiently far from the western Dutch Wadden Sea and in deep water. Therefore, artificial effects of the boundary condition on water flow are dampened to a certain degree before the tidal wave reaches the area of interest. The provided water level boundary conditions span the year 2019. The spacing of the points at which boundary conditions were provided differs per boundary section, with the southern and eastern boundary sections having a significantly smaller spacing than the northern and western boundary sections (Table 3.1). In the eastern part of the model domain, a small boundary section is located in shallow water (Figure 3.2). Duran-Matute et al. (2014) got accurate model results in the western Dutch Wadden Sea while using a boundary section in shallow water. In Duran-Matute et al. (2014), the boundary section was located closer to the western Dutch Wadden Sea than in the present study. Thus, it is probable that the boundary section is sufficiently far away to leave flow in the western Dutch Wadden Sea unaffected. The exact implementation of the boundary condition is described in Appendix D.

Freshwater discharge

Freshwater discharges at the Den Oever, Kornwerderzand, and Lauwersoog sluices were included. An overview of typical discharges for these sluices is given in Appendix E. Some smaller sluices (and the Ems River) exist in the area of interest. These were omitted due to lack of data. As described in Appendix E, the impact of omitting these is expected to be minimal. As density-related effects are not accounted for, included freshwater discharges are effectively modeled as fluxes of additional saltwater into the system.

Wind forcing

A corrected wind record from the Vlieland weather station was provided by Theo Gerkema[3]. Compared to the other weather stations near the western Dutch Wadden Sea at De Kooy (Den Helder) and Hoorn (Terschelling), less sheltering occurs due to the location of this weather station. It follows that the representation of the actual wind climate in the western Dutch Wadden Sea is better than at the other two weather stations. Missing data in the Vlieland record was supplemented with data from Hoorn multiplied by a unique correction factor for each wind sector (explained in Gerkema and Duran-Matute (2017)). They applied linear interpolation for periods in which both stations did not work. In the provided dataset, the wind direction was absent at some points in time. Linear interpolation was used to supplement missing direction entries.

3.3. Model calibration

The large-scale flow in the model was calibrated using water level measurements (Table 3.1). The full calibration procedure is detailed in Appendix F. The calibration was carried out in two stages. First, the bottom roughness was iteratively calibrated during a period with barely any wind. The water level setup in the boundary condition during this period was minimal. In the second stage, the wind drag coefficient was iteratively calibrated during a windy period.

The Chézy roughness coefficient was used. It has an inverse relationship with the bottom roughness. A high Chézy roughness value indicates a relatively smooth bed. The calibrated bottom roughness profile is shown in Figure 3.4. A large part of the model domain was assigned a relatively high Chézy roughness value of 100 $m^{1/2}/s$. This was required to increase the tidal range in the North Sea. Yet, tidal ranges in the North Sea are still underestimated using this bottom roughness profile. This points to excessive numerical damping. Some causes for numerical damping were investigated, but no direct cause was found. The remaining probable sources of numerical damping are the 1st order accuracy of the advection scheme and the implementation of the boundary condition. The bottom roughness profile was indicatively compared to the modeling efforts of van Weerdenburg et al. (2021) and Duran-Matute et al. (2014), as well as to the bottom roughness based on the length scales of bedforms encountered in the Wadden Sea (Appendix F). These comparisons suggest that the chosen bottom roughness profile underestimates the actual bottom roughness.

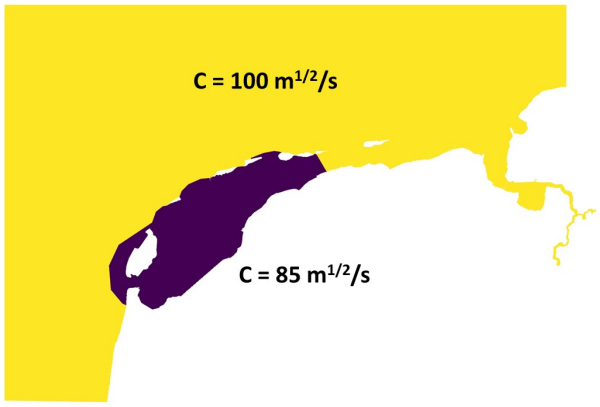

Figure 3.4: Overview of bottom roughness throughout the model domain.

[3]Methodology described in Gerkema and Duran-Matute (2017). Updated dataset includes 2019.

The Kling-Gupta efficiency (KGE) (Gupta et al., 2009), was used to assess the performance of several values for wind drag coefficient. The KGE tests the performance of the simulated signal compared to the measured signal on correlation, mean, and variability, and aggregates the result into a single metric. Overall, the KGE score was highest for a wind drag coefficient of C_D = 0.0015 (Appendix F). This value was chosen for subsequent model runs.

3.4. Validation of large-scale flow patterns

The large-scale water movement was validated based on measurements in the first half of 2019. Harmonic analysis assumes that the tide consists of the summation of tidal harmonic constants. As stated in Duran-Matute et al. (2014), this assumption is not entirely appropriate in a shallow area like the Wadden Sea, where propagation of tidal constants is affected by wind-induced sea level changes. Therefore, in addition to a harmonic analysis, the entire tidal signal is analyzed.

The simulated and measured water level timeseries at Vlieland haven were qualitatively compared. This station was chosen as the error in the most dominant tidal constituent M2 is average compared to all measuring stations, and its location is relevant for flow into the western Dutch Wadden Sea. The comparison is shown for the month of March in Figure 3.5. The wind-induced variability around March 4th - March 5th, March 13th - March 14th, and March 17th - March 19th is captured well. However, tidal ranges are underestimated. The underestimation of tidal ranges increases during neap tides. The cause for this could not be identified. Besides the underestimation of tidal ranges, no periods with structurally deviating water levels were identified (e.g. during certain wind events). The difference signal at Vlieland haven (Figure 3.5) shows little agreement with the difference signal at the model boundary (Figure D.4a). This means that differences between the simulated and measured water level timeseries originate not from the boundary condition but from the hydrodynamics that were simulated in the model domain.

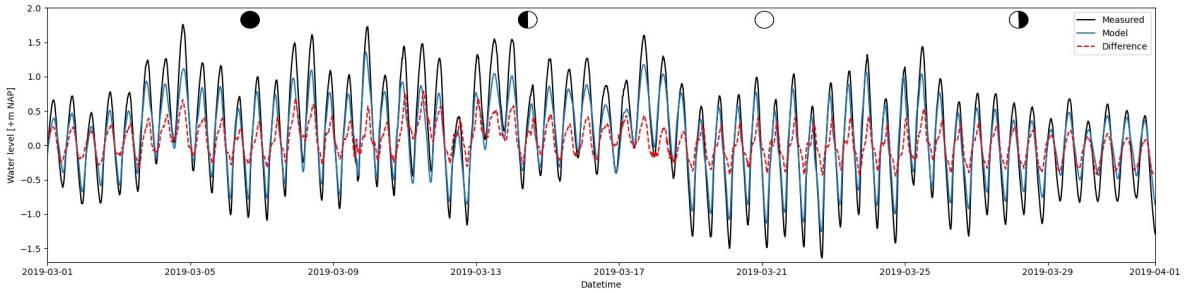

Figure 3.5: Measured and simulated water level timeseries at the Vlieland haven measuring station, and the difference between them. Shown during the period of March 1st - April 1st. Moon phases are shown to indicate the phase of the spring-neap tidal cycle.

A harmonic analysis was performed on the simulated and measured water level timeseries at the measuring stations in and around the western Dutch Wadden Sea (Table G.1). The M2, M4, and M6 constituents were assessed in detail in Appendix G. The phase and amplitude of the M2 constituent are treated here, as this is the most important constituent in the mainly semi-diurnal tide along the Dutch coast. The phase and amplitude of the M2 constituent are shown in Figure 3.6. While the amplitude of the M2 constituent in the Wadden Sea deviates in the order of a single decimeter (max. 16cm; Den Helder), the deviation in the North Sea is of the order of multiple decimeters (max. 30cm; Terschelling Noordzee). The tidal range at the North Sea and Den Helder measuring stations is underestimated. On the other hand, the representativeness of the M2 constituent improves for the measuring stations farther into the western Dutch Wadden Sea (i.e. Den Oever buiten, Kornwerderzand buiten, and Harlingen). This has two implications for the accuracy of model results. Firstly, the tidal range in the western Dutch Wadden Sea near tidal inlets is slightly underestimated (e.g. at the Oudeschild, Vlieland haven, and West-Terschelling measuring stations). Secondly, to be able to reproduce measurements in the Wadden Sea accurately while starting off with an underestimated tidal range in the North Sea, the bottom roughness in the Wadden Sea must be lower than what it should be when starting off with

the correct tidal range in the North Sea. This is supported by the overestimation of the amplitude of the friction-induced M6 constituent at measurement stations far into the western Dutch Wadden Sea (Appendix G).

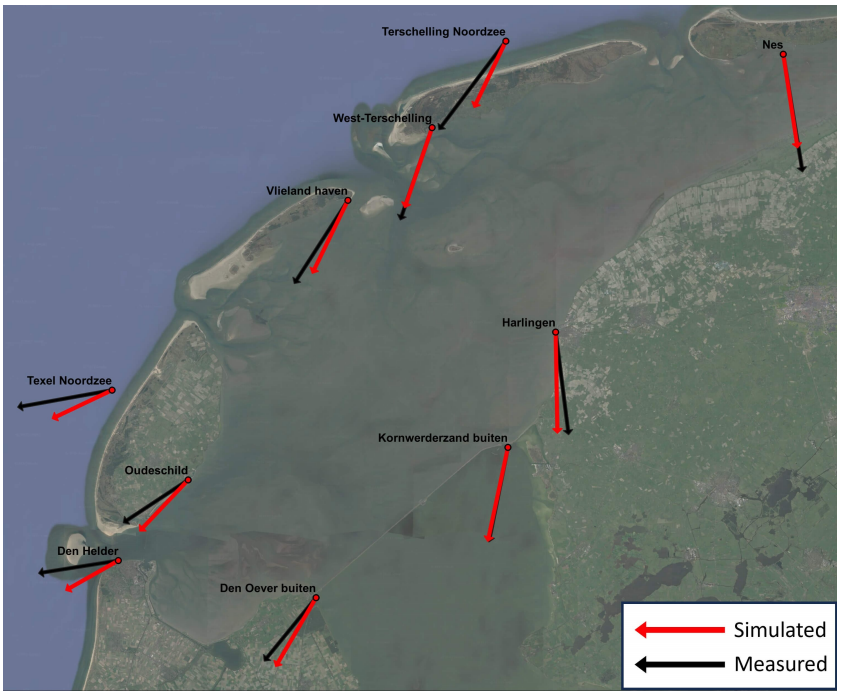

Figure 3.6: Simulated and measured phase and amplitude of the M2 constituent of the tide. Adapted from Google (n.d.).

To summarize, the model reproduces the large-scale water movement in the western Dutch Wadden Sea to within a single decimeter of measured water levels. The tidal range during neap tide is slightly underestimated. The simulated tidal range in the North Sea is underestimated, which leads to an underestimation of the tidal range in the western Dutch Wadden Sea near the tidal inlets.

3.5. Validity of flow over intertidal flats

Unfortunately, no velocity or water level measurements are available on intertidal flats during the period for which boundary condition data was available. Therefore, an adequate validation of flow over intertidal flats is not possible. The validity of flow near and over intertidal flats is inferred from the large-scale water movement.

The Wadden Sea has extensive intertidal areas. Thus, the total water volume stored on intertidal flats over the tidal cycle is substantial. These volumes play an important role in dictating the large-scale water movement in the Wadden Sea. For the model to reproduce the large-scale water movement as accurately as it does, the water movement near and over intertidal flats must be largely correct. On the other hand, as flow over intertidal flats is driven by water level gradients, deviations in water levels near intertidal flats have a significant impact on the flow over intertidal flats. It was noted that the tidal range is slightly underestimated near the tidal inlets, as well as during neap tides. These deviations in water levels do have a significant effect on flow patterns over intertidal flats and should be considered when analyzing model results.

4

Scenario definition

According to the approach outlined in section 1.4, model scenarios are run in which the following factors are varied: computational grid resolution, whether subgrid modeling technique is applied, phase of the spring-neap tidal cycle, and whether wind forcing is applied. The model scenarios to address the research question are formulated in Table 4.1. The rationale behind the scenarios, the analyses they are used for, and the implementation in the model are motivated in subsequent sections.

Table 4.1: Simulation scenarios. *Local* refers to the scale of the intertidal flat; the area where model schematizations differ.

Scenario	Tide	Local grid resolution		Wind	
		Computational	Subgrid	Direction	Velocity
Average Tide (AT)	Average	80mx80m	20mx20m	-	-
Higher-Resolution (HR)	Average	20mx20m	-	-	-
Interpolated Bathymetry (IB)	Average	80mx80m	-	-	-
Spring Tide (ST)	Spring	80mx80m	20mx20m	-	-
Neap Tide (NT)	Neap	80mx80m	20mx20m	-	-
Westerly Wind (WW)	Average	80mx80m	20mx20m	W	15 m/s
Easterly Wind (EW)	Average	80mx80m	20mx20m	E	15 m/s

Within the western Dutch Wadden Sea, two non-fringing intertidal flats complexes are selected for analyses: Kornwerderzand and the Grienderwaard-Ballastplaat-vlakte van Oosterbierum (GBO) complex (Figure 4.1a). These complexes and the channels surrounding them have unique geometries and are located in different tidal basins. The Kornwerderzand intertidal flat is intersected by several channels. It is located at the back of the Marsdiep tidal basin. It is relatively small compared to the basin size, as it takes up roughly 1/10th of its surface area. A schematic overview is given in Figure 4.1b. The flood tide enters from the south. The flood wave branches into several channels. The tidal divide between the Marsdiep and Vlie basins is in the north. Over this line, the exchange between the tidal basins is approximately zero. Flow directions during ebb are opposite to what is shown in the figure.

The GBO complex is roughly twice as large as the Kornwerderzand intertidal flat and spans from the coast to near the tidal inlet, taking up a significant part of the Vlie tidal basin. It takes up about 1/4th of the Vlie surface area. Between the vlakte van Oosterbierum and Grienderwaard is a depression with gullies, but the complex is not intersected by channels to the extent of the Kornwerderzand intertidal flat. The highest bed elevations on the GBO complex are higher than at Kornwerderzand, with the Griend island not fully inundating during High Water (HW). A schematic overview is given in Figure 4.1c. The flood tide enters from the northwest and branches into the two tidal channels to the north and to the south of the GBO complex. The southern tidal channel extends to the coast, where it bends in the northeastern direction parallel to the coast. Analyzing the differences and similarities in the flow patterns on such different complexes helps form a generic understanding of flow patterns on intertidal flats and how these flow patterns interact with different geometries.

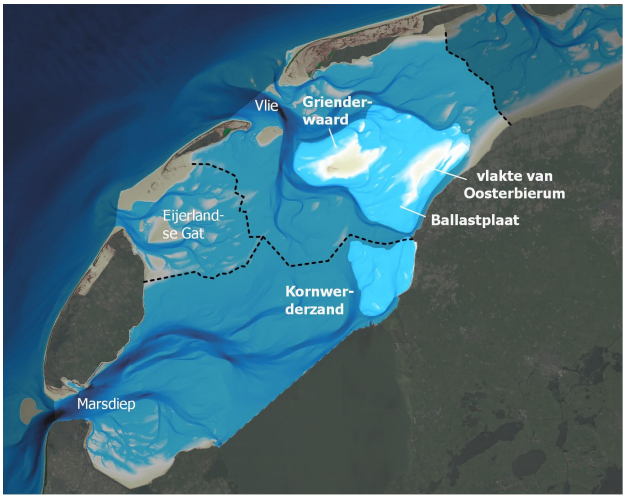

(a) Selected intertidal flats in the western Dutch Wadden Sea. Tidal divides indicated by dashed lines. Background from Google (n.d.).

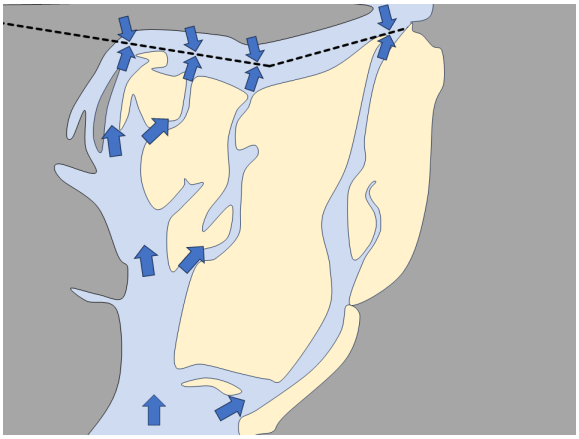

(b) Schematic overview of flow during flood at the Kornwerderzand intertidal flat. Currents indicated in blue; grey indicates areas with higher bed elevations not considered part of the Kornwerderzand intertidal flat.

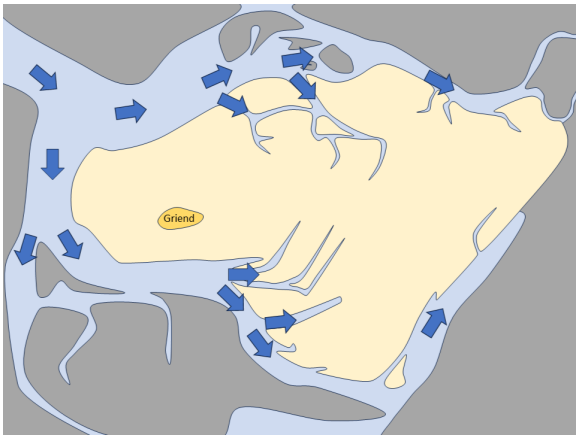

(c) Schematic overview of flow during flood at the GBO complex. Currents indicated in blue; grey indicates areas with higher bed elevations not considered part of the GBO complex.

Figure 4.1: Overview of selected intertidal flats in the western Dutch Wadden Sea, along with schematic overviews of flow patterns at the selected intertidal flats.

4.1. Subgrid modeling technique on intertidal flats

Former studies (e.g. Casulli and Stelling (2011)) investigated how the use of subgrid modeling technique throughout the entire model domain affects simulated flow patterns. Here, the impact on flow patterns of using subgrid modeling technique at the scale of an intertidal flat (hereafter: *local* subgrid) is evaluated. This offers insight into the adequacy of using subgrid modeling technique to study flow patterns on intertidal flats. To do so, the Average Tide (AT) and Interpolated Bathymetry (IB) scenarios are compared to each other and to scenario Higher-Resolution (HR). Scenarios AT and IB have identical computational grids (80mx80m on the intertidal flat; Figure 4.2). In scenario AT, a local subgrid is used on the intertidal flat. In scenarios IB and HR, however, the traditional approach of interpolating bed elevation values to a single average value per computational cell is used (i.e. no local subgrid is used) on the intertidal flat. The computational grid in HR is refined to the size of a single subgrid pixel (20mx20m; Table 3.1). It is assumed that the finer computational grid results in more accurate hydrodynamics than in scenarios AT and IB. It is important to note that the automatic wetting and drying, which is part of subgrid modeling technique, is still present in scenarios HR and IB. The Kornwerderzand intertidal flat is considered as it is computationally feasible to model this intertidal flat in its entirety in a 20mx20m grid. Furthermore, its elevation is high enough such that frequent shallow flows occur, which are of interest when studying flow patterns on intertidal flats.

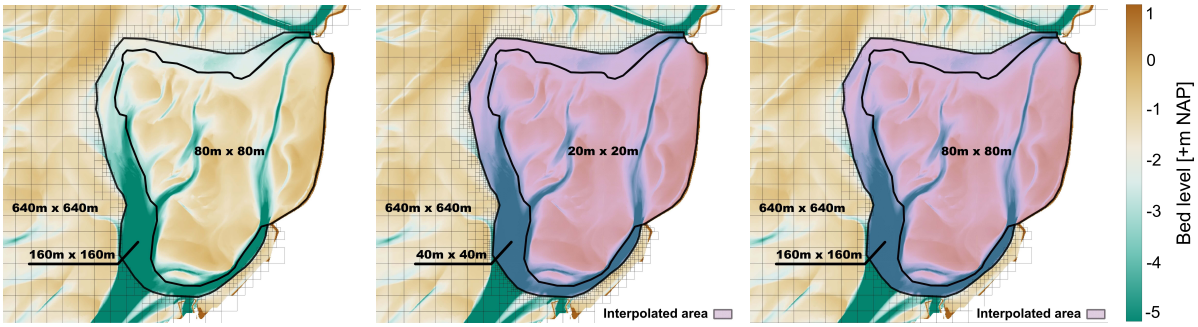

(a) Scenario AT: Computational cell sizes in simulation with coarser computational grid and subgrid.

(b) Scenario HR: Computational cell sizes and area where bed elevations are interpolated in simulation with fine computational grid.

(c) Scenario IB: Computational cell sizes and area where bed elevations are interpolated in simulation with coarser computational grid.

Figure 4.2: Computational cell sizes and areas within which bathymetric information is interpolated to an average value per computational cell at the Kornwerderzand intertidal flat in scenarios AT, HR, and IB.

The influence of applying subgrid modeling technique at the scale of an intertidal flat on the basin-scale hydrodynamics and on water storage is assessed through water depths and the bulk parameter volume. The influence on the flow patterns at the scale of the intertidal flat is analyzed using discharges through transects on sub-areas of the intertidal flat and with point measurements of flow velocities.

Water levels in the channels surrounding the intertidal flat serve as ‘boundary condition’ for flow in the area in which the model schematizations differ. For a fair comparison of how flow patterns on the scale of the intertidal flat differ due to the different model schematizations, this ‘boundary condition’ should be consistent across the three scenarios. This is not guaranteed. The hydrodynamics in the area of interest differ as a consequence of the different model schematizations. This can then affect the hydrodynamics outside of the area of interest (i.e. the ‘boundary condition’). How similar the ‘boundary condition’ is across the three scenarios is investigated in Appendix H. The ‘boundary condition’ is relatively consistent across the scenarios. The average deviation over the tidal cycle is less than 1 cm. The maximum deviation is ca. 2 cm.

4.2. Flow patterns on intertidal flats

The flow patterns on intertidal flats in the western Dutch Wadden Sea in absence of wind forcing are analyzed. An adapted scenario AT with additional grid refinement at the GBO complex is used (Figure 4.3). Focusing on water levels, discharges, exposure times, and velocities provides insight into the flow patterns. The flow patterns are caused by water level gradients (subsection 2.2.1). To find out what drives the detailed horizontal flow patterns on intertidal flats, the spatial differences in water levels are assessed on the intertidal flats and in surrounding channels. How the phase of the spring-neap tidal cycle impacts flow patterns is analyzed by assessing the same quantities while using simulations Spring Tide (ST) and Neap Tide (NT).

To expand on the analysis of flow patterns in absence of wind forcing, it is investigated how wind forcing alters flow patterns on intertidal flats. The effect of wind forcing is assessed at the GBO complex. The GBO complex has relatively high bed elevations. Consequently, water layers are shallow around HW, resulting in a large impact of wind on the flow pattern (subsection 2.2.2). In reality, the direction from which the wind blows constantly shifts. Two scenarios Westerly Wind (WW) and Easterly Wind (EW) with unidirectional wind direction are formulated, as it is more straightforward to study the impact of unidirectional wind on flow patterns. The same quantities are tracked as in the situation without wind. Findings are compared to those in scenario AT to discover how wind forcing alters the horizontal flow patterns on intertidal flats.

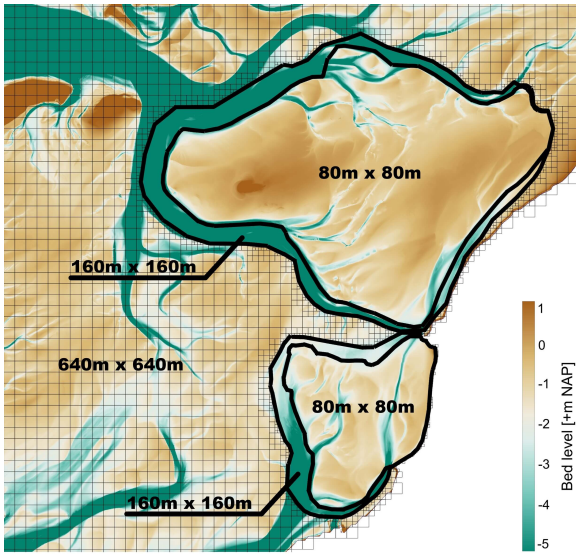

Figure 4.3: Overview of the computational grid in scenarios AT, ST, NT, WW, and EW.

4.3. Simulated conditions

Three tidal conditions are simulated: average, spring, and neap tide (Table 4.1). Actual tidal conditions are chosen over theoretical tidal conditions. This allows for a fair comparison of scenarios with and without wind forcing while using the same boundary conditions.

For the average tide, the following criteria apply: the wind forcing should be minimal such that the water level set-up in the boundary condition is minimal, and the tide should be hydrodynamically representative. The average measured tidal range at Harlingen over the validation period is 1.93m. The tide on Mar 19th is selected. With its measured tidal range of 1.90m at Harlingen it is considered hydrodynamically representative for average tidal conditions. Furthermore, wind forcing is minimal compared to the 2019 mean wind velocity of 7.7 m/s (Figure 4.4). These tidal conditions are applied without wind forcing in scenarios AT, HR, and IB. For the spring tide (ST) and neap tide (NT) scenarios, the same criteria apply as for the average tide. Additionally, for the tidal range to be representative, the spring and neap tides were selected from the 10th percentile highest and lowest tidal ranges in the validation. The periods selected for the spring and neap tide are May 18th-19th and June 24th-25th respectively.

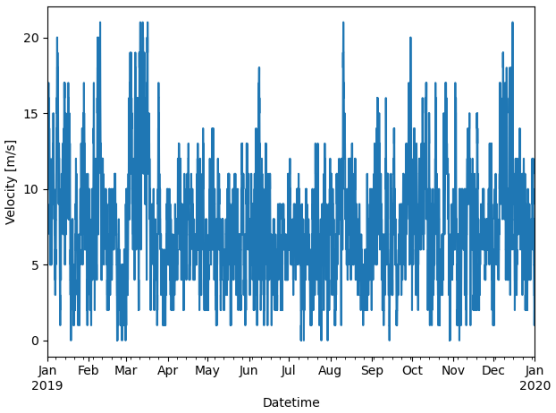

Figure 4.4: Wind velocity at the Vlieland weather station over 2019.

The tidal conditions of AT are applied with added wind forcing in scenarios WW and EW. In the 2019 wind record, velocities of up to 21 m/s occur (Figure 4.4). In the WW and EW scenarios, a relatively high wind velocity is applied such that the influence of wind on flow patterns is more pronounced. The 5th percentile wind velocity of 15 m/s is chosen.

5

Evaluation of subgrid modeling technique

The adequacy of using subgrid modeling technique for simulating flow patterns on the scale of an intertidal flat is assessed. The scenarios Higher-Resolution (HR), Interpolated Bathymetry (IB), and Average Tide (AT) are used (Table 4.1). In HR and IB, the bed elevation in computational cells covering the intertidal flat is interpolated to an average value. In AT, a subgrid is used instead. Due to its higher grid resolution HR is considered the most accurate simulation out of the three, and serves as a reference. The Kornwerderzand intertidal flat is studied. Hydraulic boundary conditions at the Kornwerderzand and Grienderwaard-Ballastplaat-vlakte van Oosterbierum (GBO) intertidal flats complexes are similar, and frequent shallow flows occur at both complexes. Therefore, findings are expected to extend to the GBO complex.

To gain insight into how well bulk behavior is reproduced on a coarser computational grid, the bulk parameter volume is compared over time between HR, IB, and AT Figure 5.1b. Gullies and tidal channels that intersect the intertidal are included in this volume estimate. Due to the different computational grids that were applied, there is a difference of 0.7% in the surface area used in the volume calculation. This mostly concerns parts of the tidal channels surrounding the intertidal flat.

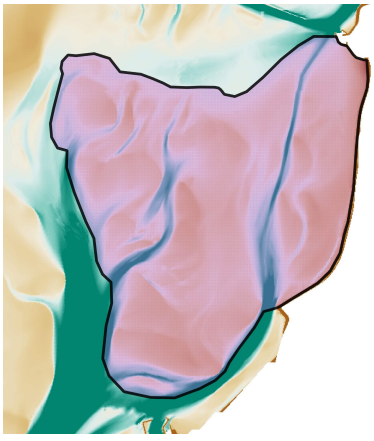

(a) Area used in the volume calculation indicated in purple.

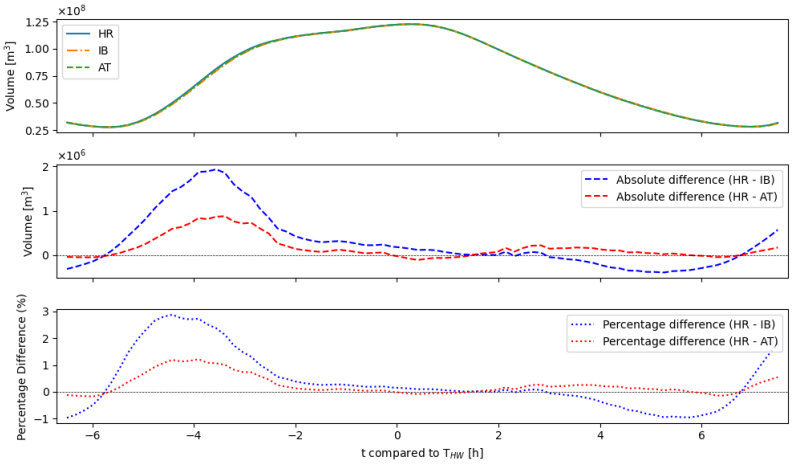

(b) Total volume over time, along with the absolute and percentual differences in volumes.

Figure 5.1: Volume over time and absolute and percentual differences in volumes in IB and AT compared to HR at the Kornwerderzand intertidal flat.

The volume deviations in IB and AT compared to HR are of the order of percentages and thus relatively small. The differences in the volume stored on the intertidal flat over the tidal cycle are too small to substantially affect basin-scale hydrodynamics, both in IB and AT. Nearly always, the difference between AT and HR is smaller than the difference between IB and HR. Hence, the bulk hydrodynamics in the coarse grid simulation with local subgrid are slightly more representative (of the bulk hydrodynamics in the fine grid simulation) than the coarse grid simulation without local subgrid.

The impact on water levels when including high-resolution bathymetric information through a subgrid is assessed. In AT and IB, a single water level value is calculated per timestep per 80mx80m computational cell. One 80mx80m cell in these scenarios corresponds to 16 computational cells of 20mx20m in HR, with each having a water level value. The bathymetry of IB is interpolated to 80mx80m. This causes a mismatch between the bathymetries of HR and IB. The impact on simulated water levels is largest where bed level variations within computational cells are large. This is shown in Figure 5.2.

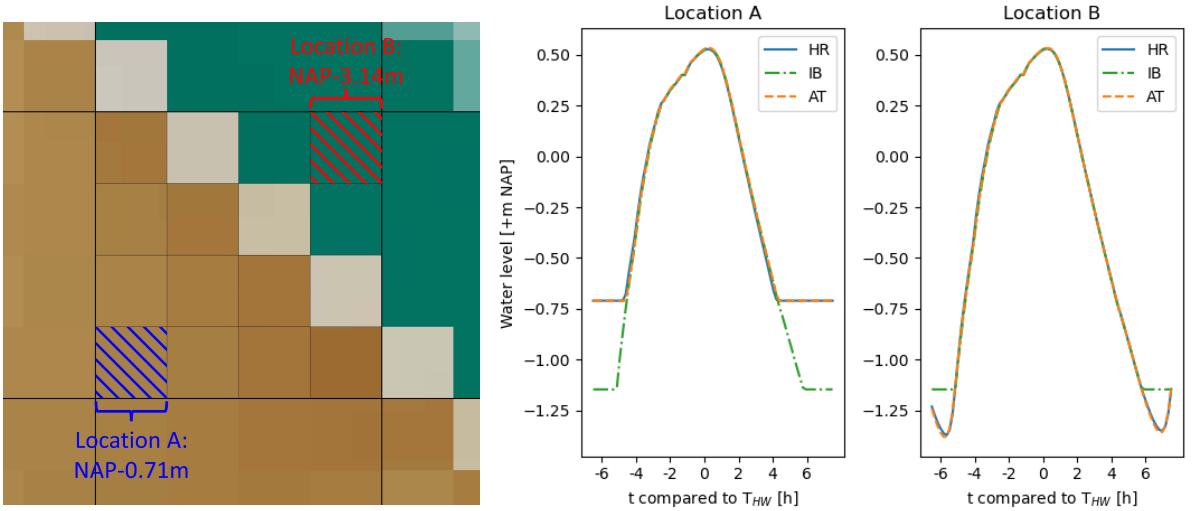

(a) 20mx20m subgrid pixels near the edge of the intertidal flat at which water levels are compared, along with their elevation and position in the 80mx80m calculation cell.

(b) Comparison of water levels in HR, IB, and AT at two locations near the edge of the intertidal flat.

Figure 5.2: Water level comparison at locations on both sides of the edge of the Kornwerderzand intertidal flat. The locations are in the same 80mx80m computational cell but in different 20mx20m computational cells. See KWP3 in Figure 5.4 for exact location.

Due to the mismatch in bathymetries, the water level at location A is underestimated by about 0.4m during the dry phase. This is the consequence of artificial lowering of the bed due to the interpolation of bathymetry. Conversely, location B is artificially elevated. This leads to Low Water (LW) levels that are 0.2m higher than what occurs in HR. There is no mismatch between the bathymetries of AT and HR due to the subgrid. As a consequence, water levels in these simulations barely differ. An improvement of subgrid modeling technique over simulations with interpolated bathymetry is that water levels at locations with large bed level variations are more accurate.

How accurately the water storing capacity of the intertidal flat is reproduced in the subgrid-based simulation is further investigated. As mentioned above, due to the subgrid in AT there is information about water depths on the 20mx20m resolution. This allows for a comparison with HR. To investigate how well the water storing capacity of the intertidal flat is reproduced in AT, the maximum water depth deviation between AT and HR over a single tidal cycle is shown in Figure 5.3. Overall, the maximum deviation in water depth is in the order of centimeters (on average 1.6cm). The water storing capacity of the intertidal flat is reproduced fairly accurately using subgrid modeling technique compared to a higher-resolution simulation without subgrid.

An exception to the fairly accurate representation of water depths is shown in Figure 5.3b. A water depth deviation of 0.11m occurs. During drying, water is stored in a depression near the edge of the intertidal flat. This is accurately captured in HR. In AT, 'leakage' occurs. The bottom elevation at the edge of a computational cell is used for calculating the discharge to a bordering cell. The area with higher elevation that separates the depression from the tidal channel next to the intertidal flat is not located on the edge of a computational cell. Therefore, water can 'leak' through it, and is essentially in direct connection with the neighboring tidal channel. The length scale of the leakage phenomenon is capped by the distances between computational cell borders (i.e. the computational cell size). The leakage phenomenon highlights that the accuracy of complex interactions of flow with bathymetry is limited by the length scale of geometric features.

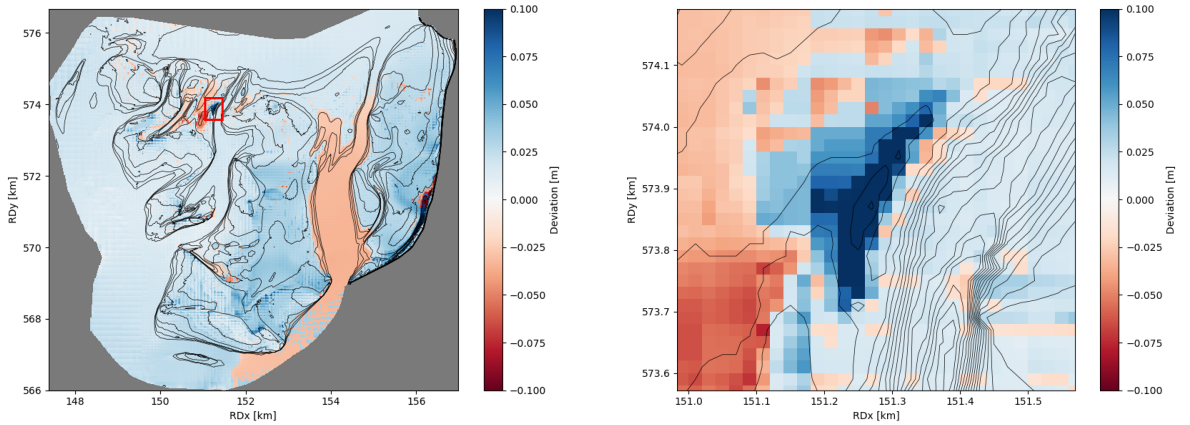

(a) Maximum water depth deviation.

(b) Zoom of maximum water depth deviation. Location indicated by red box in Figure 5.3a

Figure 5.3: Maximum water depth deviation between HR and AT over a representative tidal cycle at the Kornwerderzand intertidal flat. Positive values indicate a maximum deviation where the water depth in HR is larger than in AT. Vice-versa for negative values.

To assess the more detailed flow patterns, specific discharges through several transects are compared between scenarios AT, IB, and HR. Furthermore, velocities at points are tracked. Velocities are only compared between AT and IB, as the higher-resolution HR output would need to be aggregated to be able to compare. This could skew results based on the chosen aggregation method. Locations are indicated in Figure 5.4. The discharge through transects is divided by the total transect length to get specific discharge. To account for different bathymetric characteristics, transects and velocity points are defined at various locations: at the edge of the intertidal flat (KWT1, KWT3), from the edge to the upper intertidal flat and roughly perpendicular to the previous transects (KWT2, KWT4), on the lower intertidal flat (KWP3), on the upper intertidal flat (KWT5, KWP4), in a gully with a width of roughly 100m (KWT6, KWP2), and in a tidal channel with a width of roughly 120m (KWT7, KWP1). The edge of the intertidal flat is defined as the mean of LW levels at Harlingen over the validation period (-1.03m NAP), as bed elevations that exceed this level can generally inundate and drain.

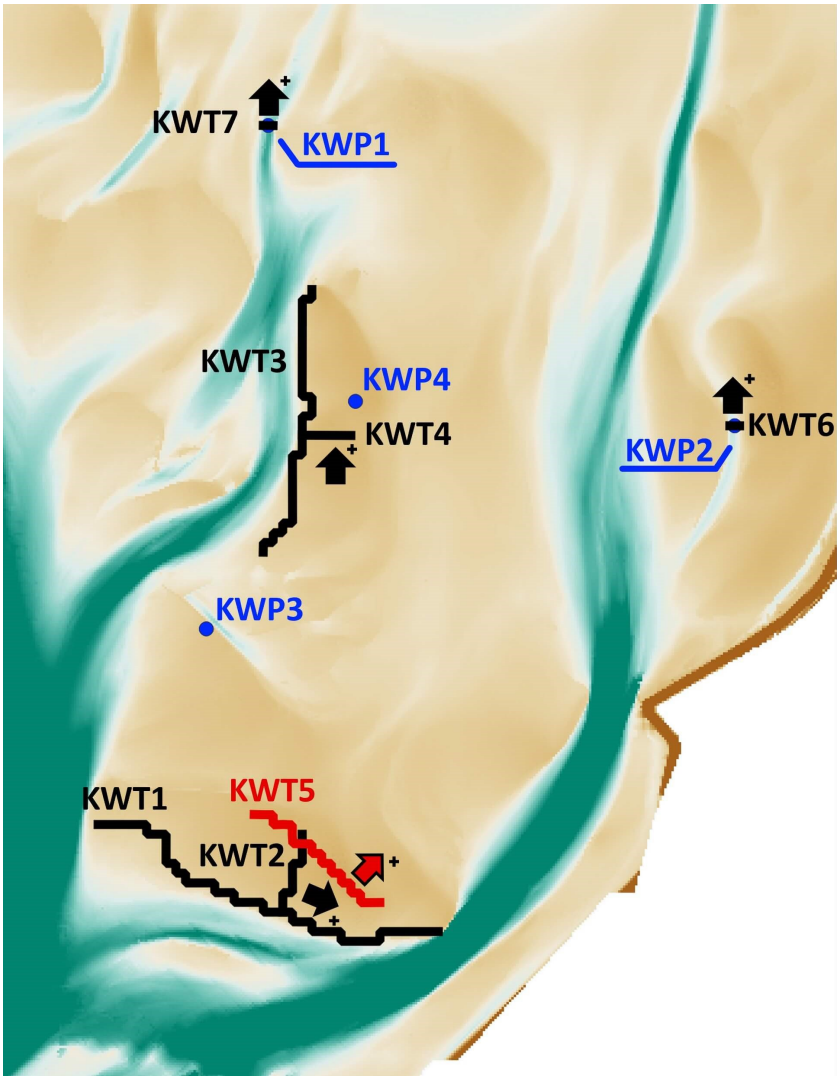

Figure 5.4: Location of selected transects and point measurements at the Kornwerderzand intertidal flat. Positive direction indicated for transects not on the edge of the intertidal flat.

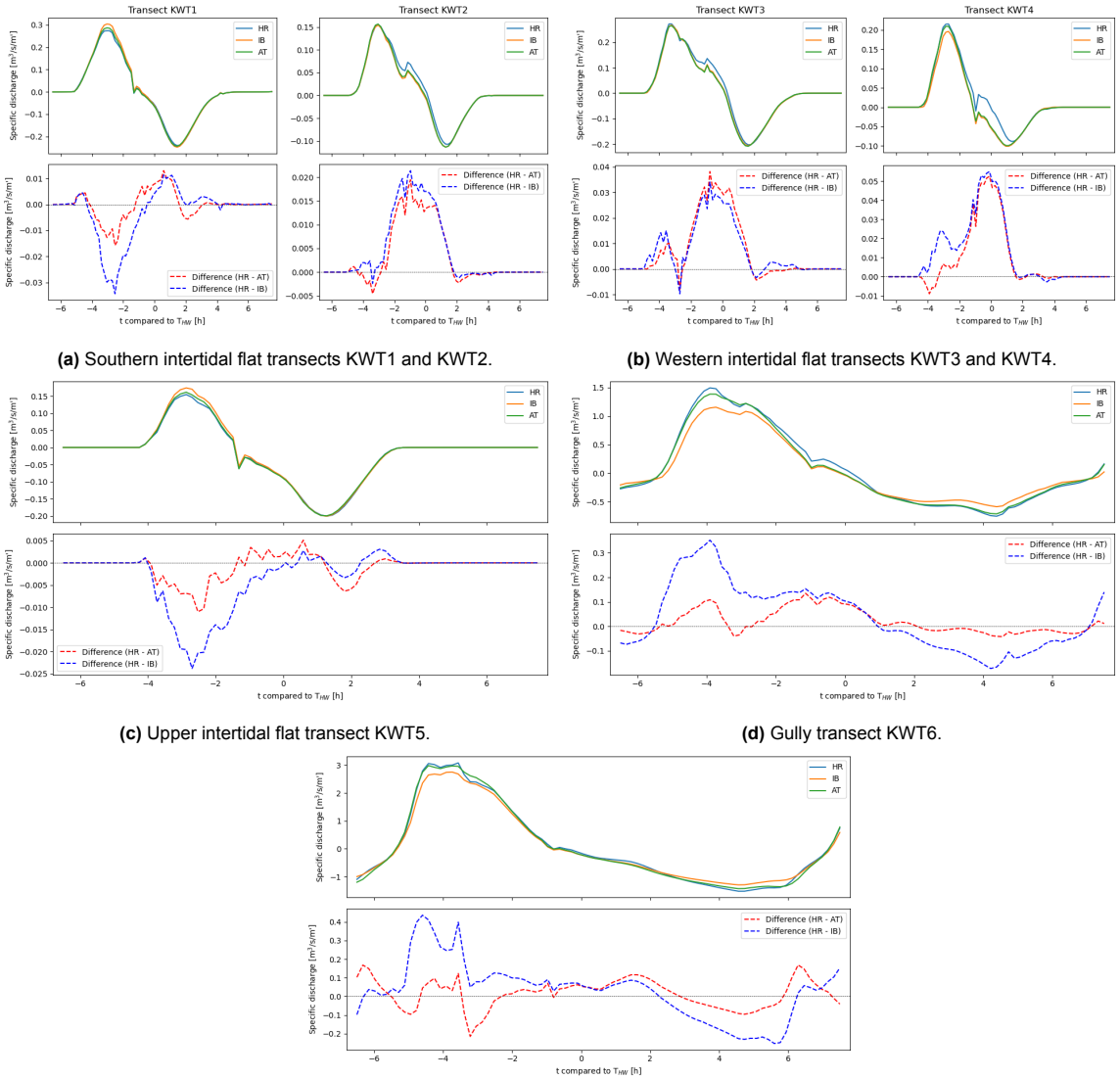

(a) Southern intertidal flat transects KWT1 and KWT2.

(b) Western intertidal flat transects KWT3 and KWT4.

(c) Upper intertidal flat transect KWT5.

(d) Gully transect KWT6.

(e) Tidal channel transect KWT7.

Figure 5.5: Specific discharge through several transects at the Kornwerderzand intertidal flat, and the difference of discharges in IB and AT compared to HR. Transect locations indicated in Figure 5.4.

Specific discharges in AT, IB, and HR are shown in Figure 5.5, along with the differences in the specific discharge of AT and IB compared to HR. Specific discharges in AT are more accurate than in IB (compared to HR) at transects KWT1, KWT5, KWT6, and KWT7. The difference between IB and HR is roughly twice as large as the difference between AT and HR during some periods. At KWT1, there is a geometric feature in front of the edge of the intertidal flat. The flow pattern is complex as flow interacts with this feature before entering the intertidal flat. Transect KWT5 is located close to KWT1 and has a similar orientation. It is probable that the improvement at this transect originates from the better representation of flow over the edge of the intertidal flat at KWT1. The characteristic that transects KWT6 and KWT7 share is that there are large bed level differences within the computational cells. Here, resolving friction and the cross-section through which water exchanges to the subgrid resolution improves the flow pattern.

The largest differences between AT and IB occur during rising tide. At most transects large differences occur during the falling tide as well. The probable explanation for this is the assumption of a uniform friction slope used in subgrid modeling technique. The friction term in the depth-averaged shallow-water equations is $\frac{\tau_b}{\rho_w H}$, in which $\tau_b \sim u^2$. When the maximal specific discharges occur during the rising and falling tide, velocities are largest. The friction term is relatively large compared to other terms in the

shallow-water equations. Flow is then friction-dominated, and the assumption of a uniform friction slope is important for resolving the flow pattern in AT. At other moments in the tidal cycle, when velocities are smaller and/or water depths are larger, the assumption of a uniform friction slope affects the flow pattern to a lesser degree. At those moments, the differences between AT and IB are smaller.

On the scale of an intertidal flat, the local effects of subgrid modeling technique may lead to a more accurate representation of discharges compared to a simulation on interpolated bathymetry. The largest improvements were observed where bed level gradients and complex flow around bathymetric features shape the flow pattern. While in some situations the local effects of subgrid modeling technique did not improve the accuracy of simulated discharges compared to a simulation on interpolated bathymetry, the accuracy was never substantially decreased.

Velocities at points are compared for AT and IB (Figure 5.6). At KWP1 and KWP2, the difference between simulated velocities using a local subgrid and using an interpolated bed only slightly deviate. The lowest bed elevations at location KWP3 are beneath the LW level. Therefore, no drying should occur. This is the case in AT. In IB, the lowest elevations at KWP3 are higher than the LW level due to the interpolation of the bed elevation. This leads to artificial drying. During the last stage before drying, water accelerates along the bed level gradient. This leads to an artificial velocity peak before the cell artificially dries. In reality, the actual velocity is closer to the results from AT.

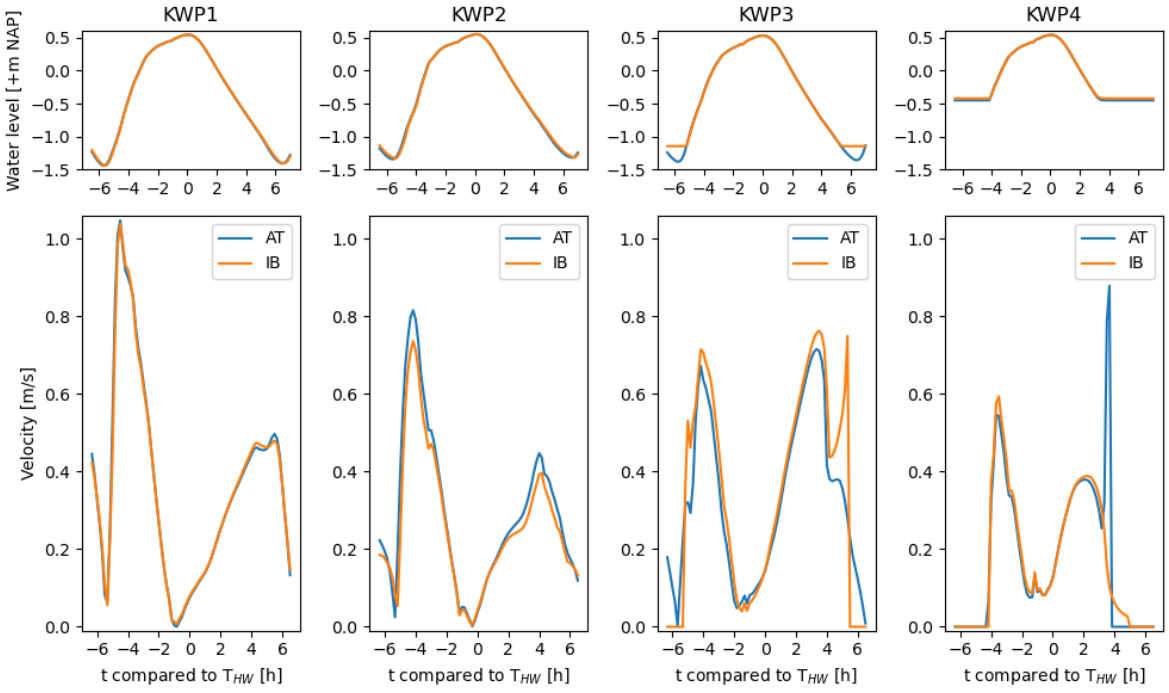

Figure 5.6: Velocities (along with water levels) in AT and IB at locations KWP1 (tidal channel), KWP2 (gully), KWP3 (lower intertidal flat), and KWP4 (upper intertidal flat). Locations indicated in Figure 5.4.

On the upper intertidal flat, there is a velocity peak in AT just before drying. The flow accelerates as it follows the bed level gradient. This velocity peak is not present in IB. Here, the interpolation of the bed results in a stair-like bed gradient with an 80m resolution. These 80m steps are too coarse to accurately capture the acceleration that occurs during the last stage of drying.

Overall, velocities in a simulation with a local subgrid and a simulation on interpolated bathymetry are very similar. However, artificial velocity peaks can occur due to interpolation of bed level gradients. Furthermore, simulations on interpolated bathymetry do not accurately capture the velocity peak during the final stage of drying on the upper intertidal flat. The bed level gradient along which flow accelerates in reality is not smooth enough using interpolated bathymetry.

5.1. Concluding remarks

In this chapter, it was tested how well the water storing capacity and detailed flow patterns on intertidal flats are reproduced when using subgrid modeling technique. Here, these findings are combined with findings from the model calibration and validation phases to comment on the adequacy of using subgrid modeling technique to study flow patterns on intertidal flats. Note that the automatic wetting and drying, which enables the study of shallow flows, was not explicitly considered.

It was not possible to validate the flow over intertidal flats due to a lack of water level measurements. However, it was inferred that because water storage on intertidal flats plays an important role in dictating large-scale flow patterns, flow over intertidal flats had to be largely correct. In this chapter, the water storage on the intertidal flat was similar when using a fine computational grid and when using a local subgrid. This indicates that a local subgrid simulation can represent the large-scale flow pattern (nearly) as accurately as a fine grid simulation.

The detailed flow pattern on the intertidal flat follows from the water levels in the channels surrounding the intertidal flat. In the western Dutch Wadden Sea, the M2 constituent is accurate to the order of a single decimeter. This means that the simulated flow pattern deviates to some extent from the actual flow pattern. The detailed flow pattern in the simulation with a local subgrid and the simulation using an identical computational grid but without local subgrid were compared. The detailed flow pattern in the simulation with the local subgrid corresponded more closely to the simulation on a finer grid in terms of volumes, water levels, and specific discharges. In terms of velocities, it corresponded more closely to how the actual flow pattern should behave according to theory. The occurrence of ‘leakage’, and the still considerable differences between specific discharges of the local subgrid and fine grid simulations indicate that subgrid modeling technique should be considered as an improvement to coarse grid simulations instead of a replacement for fine grid simulations.

Moving forward, simulations with a local subgrid and a computational cell size of 80mx80m on the intertidal flat are used. Based on the findings in this chapter, this is not expected to significantly decrease the accuracy of simulated large-scale flow patterns. The detailed flow pattern in an 80mx80m simulation with a local subgrid is less accurate than a 20mx20m simulation without a subgrid. However, it is expected that an 80mx80m simulation suffices for simulating the flow patterns on the Kornwerderzand and GBO intertidal flats complexes, as resolving flow phenomena on a sub-80mx80m scale is not necessarily required to answer the research question. Furthermore, it is not computationally feasible to model the GBO complex using a finer grid resolution. The automatic wetting and drying, which was not explicitly considered, plays an important role in resolving the detailed flow pattern.

6

Flow patterns on intertidal flats

The horizontal flow patterns on intertidal flats and the water level gradients that cause these are studied at the Kornwerderzand intertidal flat and the Grienderwaard-Ballastplaat-vlakte van Oosterbierum (GBO) intertidal flat complex. The aspects that are manipulated over simulations are the tidal forcing and whether wind forcing is applied.

6.1. Kornwerderzand

The flow patterns at the Kornwerderzand intertidal flat are simulated with a hydraulically representative tide without wind forcing in scenario Average Tide (AT). The flow patterns are visualized using velocity vectors (Figure 6.1). The water level differences that drive the flow are visualized in Figure 6.2. In this figure, at several instances of the tidal cycle, the water level deviation to the mean water level in the Kornwerderzand sub-domain is shown.

Water enters from the south, causing a water level gradient from south to north (Figure 6.2a). The wider and deeper western tidal channel conveys more water, causing the water levels in the west to rise faster than in the east. The water level gradient turns to the northeast direction (Figure 6.2b). Consequentially, most of the intertidal flat is inundated from the southwestern direction. Due to the interaction of the tidal flood wave with the tidal basin, the water level gradient changes to ebb-oriented before High Water (HW) occurs anywhere in the Kornwerderzand sub-domain (Figure 6.2c). The flow on the intertidal flat and in the tidal channels responds differently. On the intertidal flat, the flow turns to the ebb direction relatively quickly (Figure 6.1c). The response of the flow in tidal channels is slower. In tidal channels, the flow turns to the ebb direction around the occurrence of HW, about 1.5 hours later. A possible explanation is the effect of water depth on the flow pattern. The water depth is relatively large in tidal channels. The relative importance of friction is then small, and the relative importance of inertia is large. On the intertidal flat, water depths are relatively small. This results in a phase difference in how the flow in tidal channels and on the intertidal flat respond to the reversal of the water level gradient.

Gullies play an important role in conveying the discharge onto the intertidal flat during flood and from the intertidal flat during ebb (Figure 6.4). During flood, discharge starts flowing through gully transect KWT8 an hour before discharge starts flowing through edge transect KWT3. Once discharge through KWT3 increases from zero, the specific discharge through KWT8 is already 0.5 m^3/s/m'. The flow just before LW almost exclusively follows the bed level gradients which are oriented towards gullies, to subsequently drain into the tidal channels (Figure 6.1f). After the discharge through KWT8 decreases to zero, specific discharges of on average 0.2 m^3/s/m' flow through KWT3 for two more hours (Figure 6.4).

The water level timeseries (Figure 6.1g) is asymmetrical in time. The flood period is shorter than the ebb period. The rate at which the water level rises during flood is larger than the falling rate during the longer ebb period. This causes larger water level gradients (compare Figure 6.2b and Figure 6.2e), resulting in larger discharges (Figure 6.4) and velocities (e.g. Figure 6.1b and Figure 6.1e) during flood than during ebb.

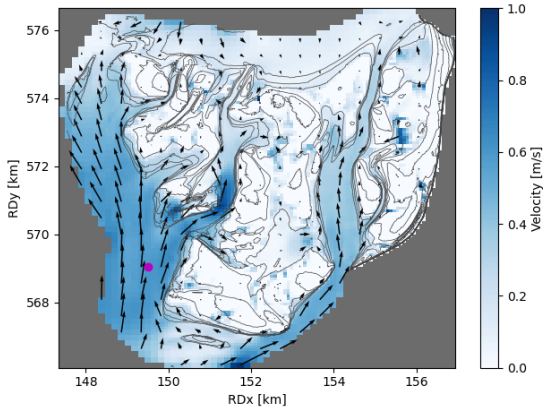

(a) t_1: Ca. 1 hour after LW.

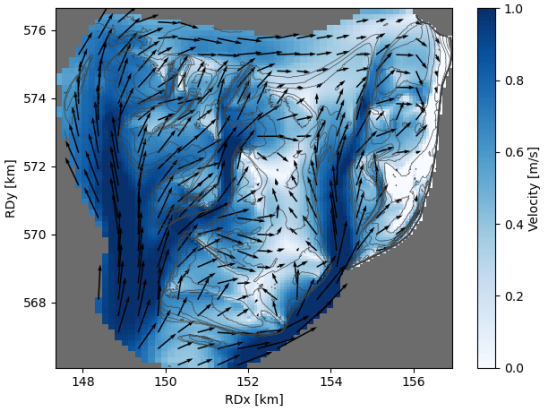

(b) t_2: Rising tide.

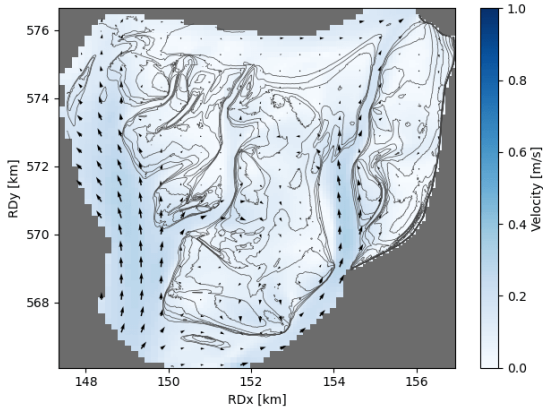

(c) t_3: Ca. 1.5 hours before HW.

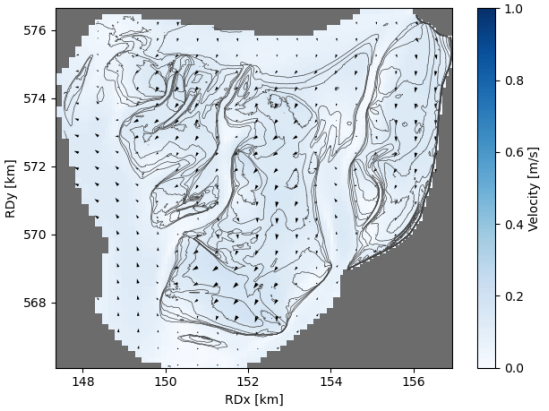

(d) t_4: High Water.

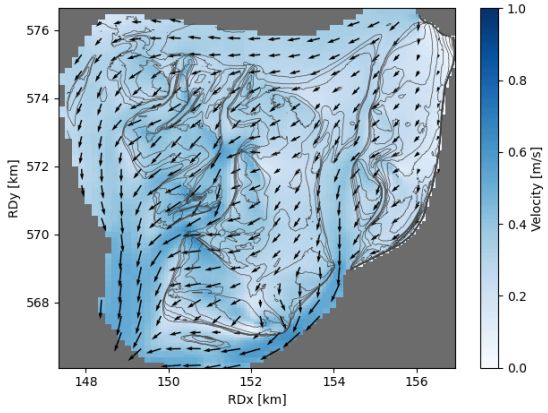

(e) t_5: Falling tide.

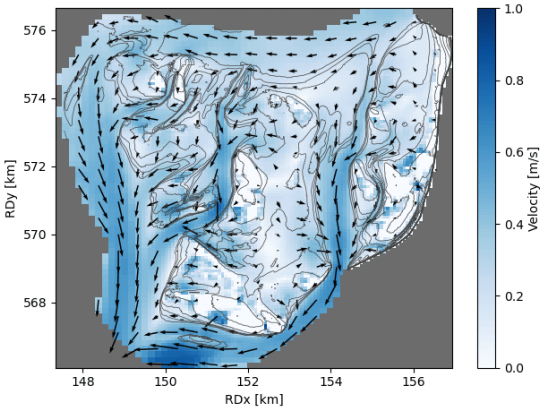

(f) t_6: Ca. 2 hours before LW.

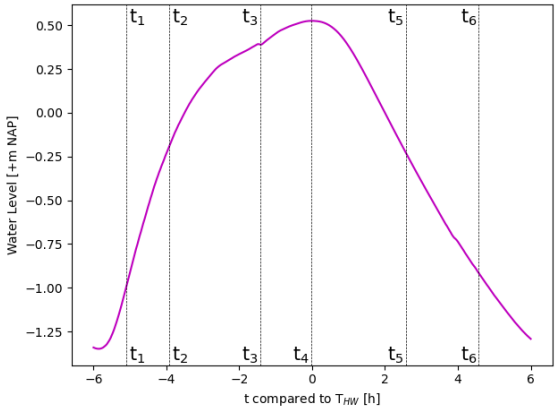

(g) Overview of instances in the tidal cycle at which snapshots are shown. Location of water level timeseries indicated in subfigure a.

Figure 6.1: Snapshots of vector velocities at the Kornwerderzand intertidal flat at different moments in AT, along with an overview of the instances in the tidal cycle at which snapshots are shown.

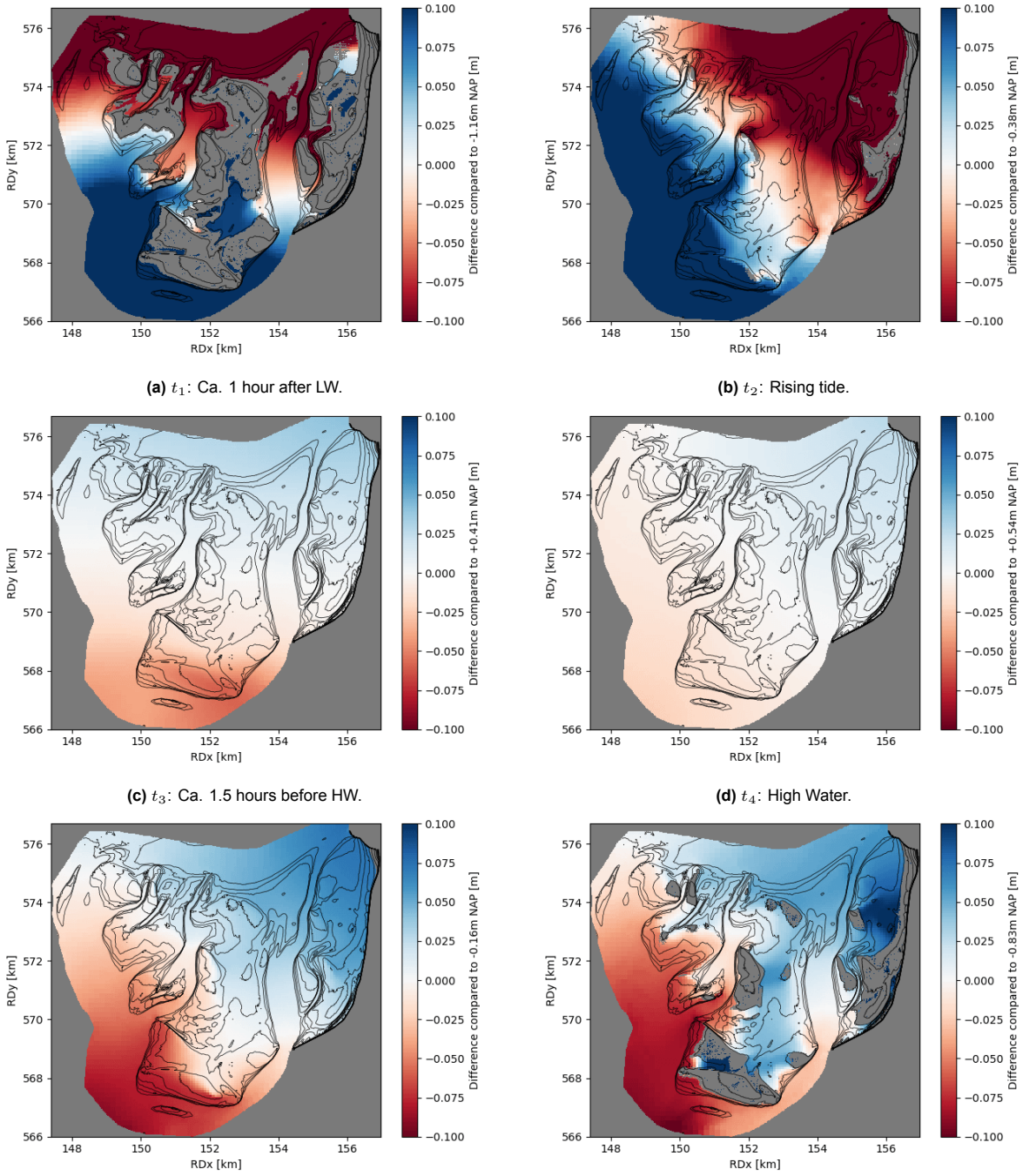

(a) t_1: Ca. 1 hour after LW.

(b) t_2: Rising tide.

(c) t_3: Ca. 1.5 hours before HW.

(d) t_4: High Water.

(e) t_5: Falling tide.

(f) t_6: Ca. 2 hours before LW.

Figure 6.2: Snapshots of water level differences compared to the mean water level at the Kornwerderzand intertidal flat at different moments in AT. Figure 6.1g gives an overview of the instances in the tidal cycle at which snapshots are shown.

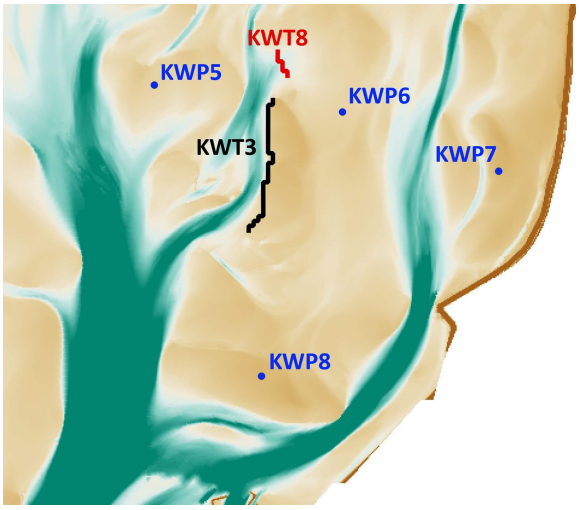

Figure 6.3: Location of Figure 6.4 transects and Figure 6.5 measurement points. KWT3 placed at the MLW[1] contour. KWT8 placed in a gully. Flow onto the intertidal flat defined as positive.

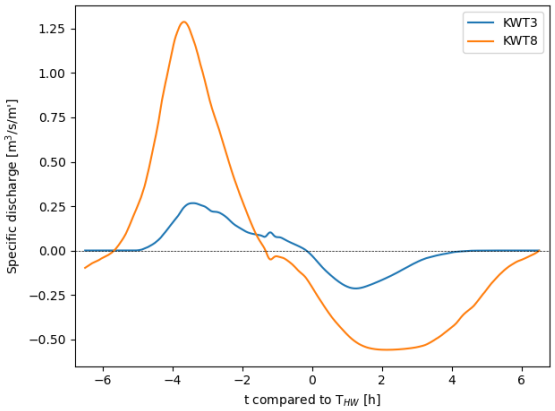

Figure 6.4: Specific discharge through transects KWT3 and KWT8 in AT.

To establish the more detailed flow patterns on the intertidal flat, the evolution of water levels and velocities are tracked at four points on the intertidal flat (Figure 6.5). To study the differences in flow magnitude at different elevations, two points KWP5 and KWP6 are placed on the lower intertidal flat, and two points KWP7 and KWP8 are placed on the upper intertidal flat. As demonstrated by the evolution of the absolute velocity at location KWP7, four velocity peaks can occur over the tidal cycle. There is a large water level gradient when a location is just inundated. This causes an initial velocity peak. The water level gradients are maximal when the rate at which the water level rises and the rate at which the water level falls are maximal. The result is that there are velocity peaks when the rising rate and falling rate of the tide are maximal. Just before drying, water flow accelerates along bed level gradients, which leads to the final velocity peak. At locations KWP8 and KWP5, the moment at which the maximal positive water level gradient occurs coincides with the moment of inundation. Therefore, these are not separate velocity peaks. Generally, velocities on the lower intertidal flat are larger than at the upper intertidal flat. Location KWP6 differs. As this location inundates from and dries towards two tidal channels, velocities are lower than at the other locations.

[1]Average LW at the Kornwerderzand measuring station over the validation period (-0.93m NAP).

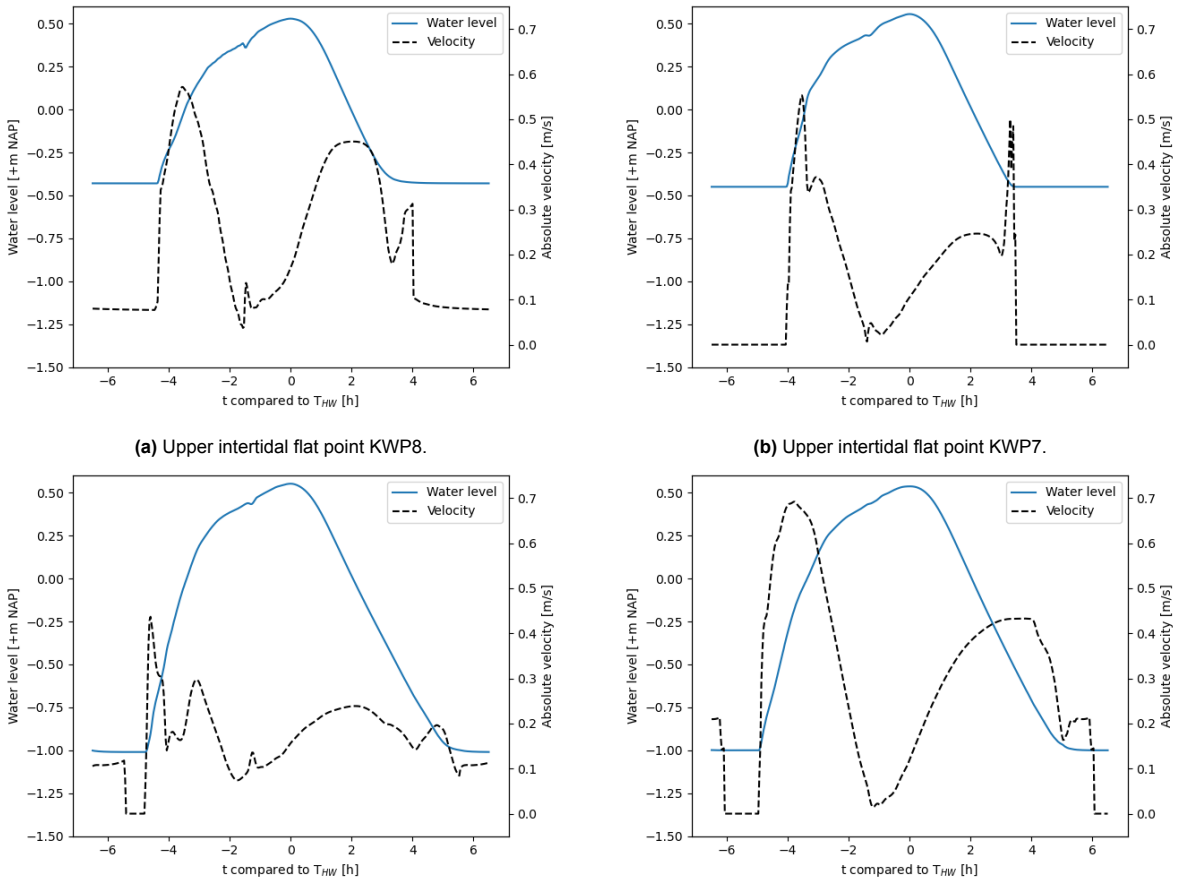

(a) Upper intertidal flat point KWP8.

(b) Upper intertidal flat point KWP7.

(c) Lower intertidal flat point KWP6.

(d) Lower intertidal flat point KWP5.

Figure 6.5: Water levels and velocities over a tidal cycle in AT at several locations on the lower and upper Kornwerderzand intertidal flat. Locations indicated in Figure 6.3

The exposure times at the Kornwerderzand intertidal flat in AT are visualized in Figure 6.6a. A very shallow water layer remains on the bed for some time during draining. In reality, this water layer might infiltrate into the bed, and for practical purposes this could be considered as ‘dry’. A pixel was considered as ‘dry’ when the water depth was lower than 1 cm. The highest bed elevations are dry for roughly 6 hours or approximately half the tidal cycle. Exposure time decreases with elevation. The model artifact of ‘trapped water’ is visible. At some bed pixels with higher elevation, the exposure time equals zero due to the absence of infiltration processes in the model. The relationship between exposure time and bed elevation is investigated to assess to what extent exposure time depends on the detailed flow pattern. This has implications for the adequacy of using a rigid lid approach (i.e. a flat water layer) to approximate exposure time. Figure 6.6b shows a scatter plot of the elevation of all 20xm20m bed pixels and their respective exposure times. The ‘trapped water’ artifact is visible for pixels with higher bed elevation and exposure times of zero. There is a clear relationship between bed elevation and exposure time. However, at the lower bed elevations there is a spread of up to a few hours. This suggests that on the lower intertidal flat, the detailed flow pattern is important for accurately estimating exposure times. It follows that estimating exposure times with a flat water layer does not suffice. The exact cause for the spread in exposure times is not investigated here.

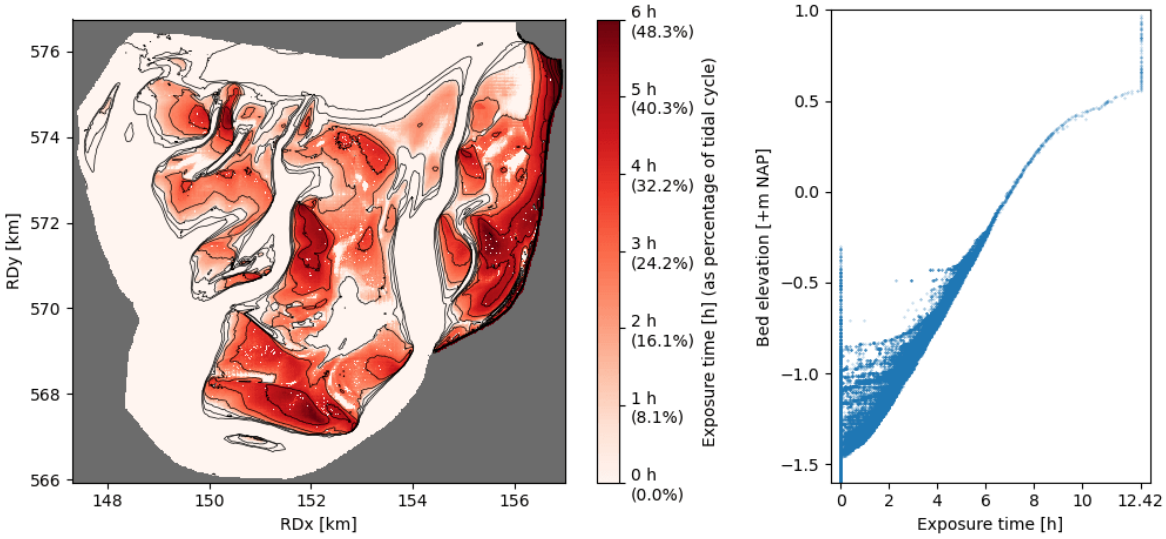

(a) Exposure time.

(b) Scatter plot.

Figure 6.6: Exposure time and scatter plot of exposure time against bed elevation at the Kornwerderzand intertidal flat in AT.

6.1.1. Spring-neap tidal cycle

The effect of the spring-neap tidal cycle on flow patterns at the Kornwerderzand intertidal flat is studied by comparing scenarios Spring Tide (ST), Neap Tide (NT), and AT. Water level timeseries (Figure 6.7) and specific discharges (Figure 6.8) are shown. What stands out is that the different timeseries do not oscillate around the same mean water level. It is probable that this is caused by the minimal wind set-up and/or set-down that is present in the boundary conditions during these simulations. Note that the NT timeseries is less asymmetric in time than the AT and NT timeseries. A preliminary assessment of the measured tidal records suggests that tidal asymmetry increases from relatively symmetrical during neap tide to relatively asymmetrical during spring tide. A possible explanation is that the interaction with the tidal basin of tides with a smaller tidal range gives rise to less tidal asymmetry than tides with a larger tidal range.

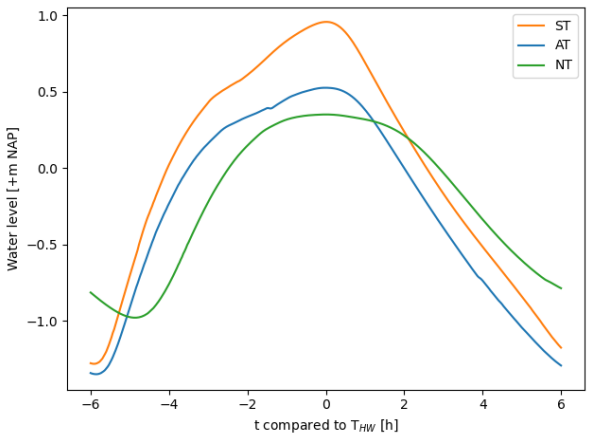

Figure 6.7: Water levels at the Kornwerderzand intertidal flat in ST, AT, and NT (see Figure 6.1a for location).

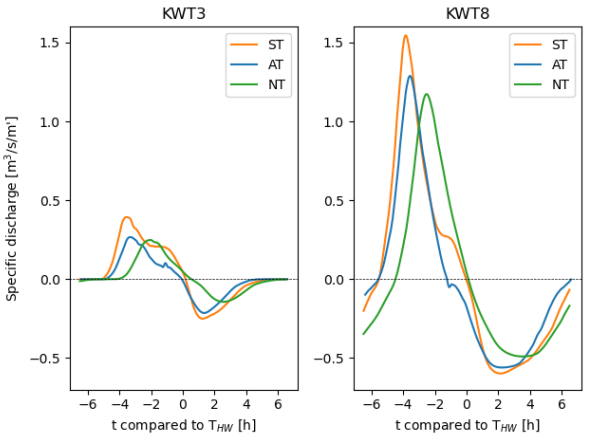

Figure 6.8: Specific discharges through intertidal flat edge transect KWT3 and gully transect KWT8 in ST, AT, and NT (see Figure 6.3 for location).

The specific discharges through transects KWT3 and KWT8 in simulations ST, AT, and NT are shown in Figure 6.8. The magnitude of the peaks during flood and ebb seems proportional to the HW level of the tide in Figure 6.7, suggesting that discharge over the intertidal flat is indeed proportional to the HW level (subsection 2.2.1).

The spatial distribution of velocities and water level gradients in ST and NT were compared to AT. The full comparison is detailed in Appendix I. The comparison for spring tide is shown during rising tide (t_2; Figure 6.1g) in Figure 6.9. The spatial distribution of the water level gradients in ST (Figure 6.9b) is almost identical to that of AT (Figure 6.2b). Results suggest that the spatial distribution of water level gradients, and consequently the spatial distribution of flow directions, does not depend on the phase of the spring-neap tidal cycle. The magnitude of the water level gradients, and consequently the magnitude of flow velocities, does depend on the phase of the spring-neap tidal cycle. However, it is hard to confirm if this is the case over the entire spring-neap tidal cycle. Due to the differences in tidal asymmetry across the spring-neap tidal cycle (e.g. Figure 6.7), it is hard to compare the exact same phase of different tidal waves.

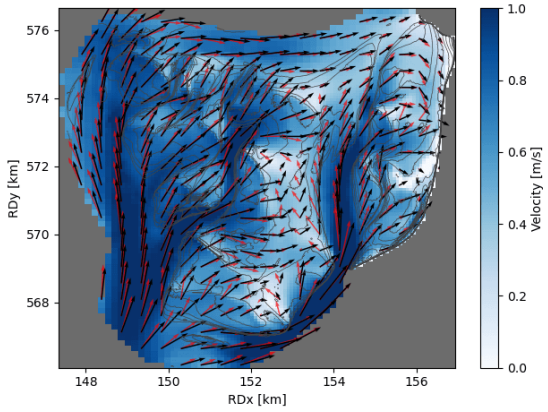

(a) Velocities in ST in black. Velocities in reference simulation AT indicated in red.

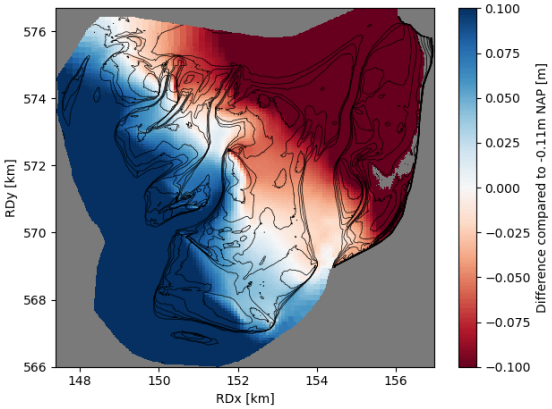

(b) Water level differences.

Figure 6.9: Velocities and water level differences compared to the mean water level at t_2 at the Kornwerderzand intertidal flat in ST.

The difference in exposure times of NT and ST compared to AT is shown in Figure 6.10. Figure 6.10c shows water level and velocity timeseries at several locations, along with water level and velocity timeseries. The higher LW level of NT at KWP5 and KWP6 results in longer submergence. In the water level timeseries at KWP7 and KWP8, the HW level in NT is similar to AT and exceeds the upper intertidal flat for roughly an equal period of time. This is reflected in the exposure time plot, where the NT exposure time is shorter on the lower intertidal flat and roughly equal on the upper intertidal flat. At all four locations, water levels in ST exceed the bed elevation for longer than in AT. The consequence is a uniform decrease in exposure times in ST compared to AT, regardless of intertidal flat bed elevation.

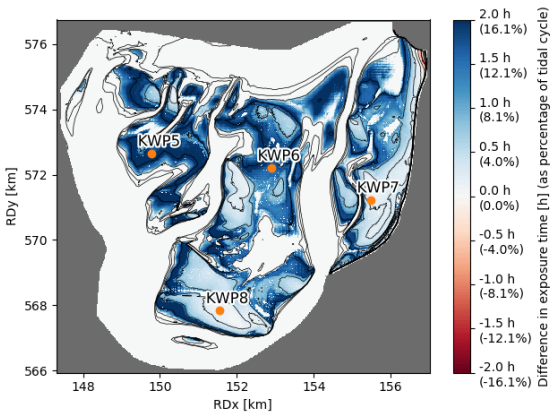

(a) Difference in exposure time between AT and NT. Positive values indicate AT has a longer exposure time. Subfigure c locations indicated for reference.

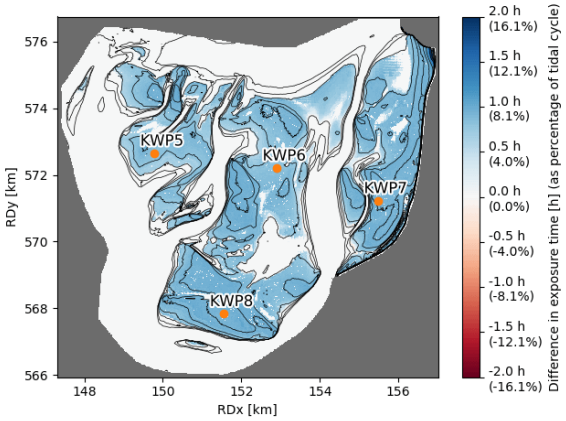

(b) Difference in exposure time between AT and ST. Positive values indicate AT has a longer exposure time. Subfigure c locations indicated for reference.

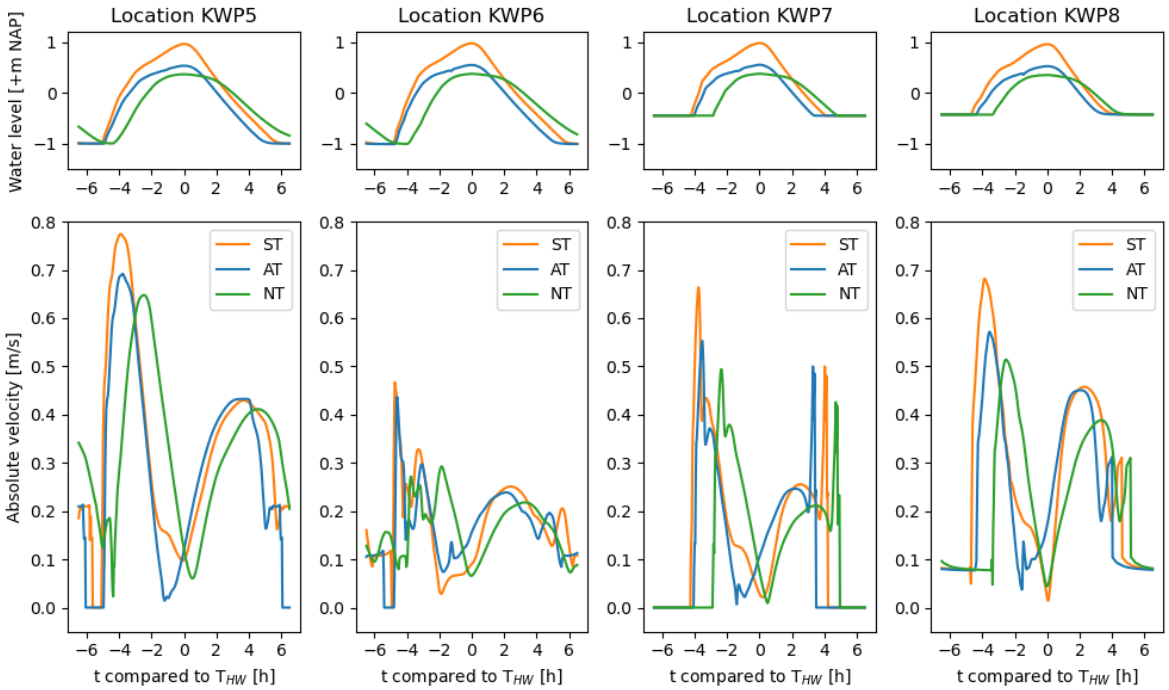

(c) Water levels and velocities at KWP5 (lower intertidal flat), KWP6 (lower intertidal flat), KWP7 (upper intertidal flat), and KWP8 (upper intertidal flat). Locations indicated in subfigures a and b.

Figure 6.10: Spatial differences in exposure time at the Kornwerderzand intertidal flat between (a) NT and AT, (b) as well as NT and AT, (c) along with point measurements of velocity and water level in ST, AT, and NT.

At points KWP5, KWP7, and KWP8, peak velocities during the ST rising tide are larger than in AT. The cause is the rate at which the water level rises. In the water level timeseries, it can be seen that the rate at which the water level increases is larger in ST than in AT. This causes steeper water level gradients and leads to larger velocities. The rate at which the water level decreases during the falling tide in ST is similar to AT, leading to similar velocities. In NT, the rising rate is similar to AT, and the falling rate is smaller. This leads to similar velocities during the rising tide and smaller velocities during the falling tide. The rate at which the tide rises and falls is related to how asymmetrical the tide is. An increase in temporal asymmetry from relatively symmetrical neap tides towards more asymmetrical spring tides was identified. Velocities (and consequently discharges) in the western Dutch Wadden Sea are therefore not only related to the HW level (as mentioned in subsection 2.2.1). The tidal asymmetry, which seems to vary over the spring-neap tidal cycle, also affects tidal velocities.

6.2. Grienderwaard-Ballastplaat-vlakte van Oosterbierum complex

The focus of this section is on the differences and similarities in flow patterns between the Kornwerderzand and Grienderwaard-Ballastplaat-vlakte van Oosterbierum (GBO) intertidal flats complexes. This helps gain insight into how flow interacts with different intertidal flat geometries. The geometry (i.e. size, bed elevation, and degree to which it is intersected by gullies) of the GBO complex differs from the Kornwerderzand intertidal flat. The length scale of the GBO complex is larger. As the GBO complex spans from near the tidal inlet to the coast, water levels at opposing ends of this complex differ more than at the Kornwerderzand intertidal flat. A single water level timeseries sufficed to show water levels at the Kornwerderzand intertidal flat. At the GBO complex, two timeseries are shown in tidal channels near the extreme ends of the complex (Figure 6.11h). These give approximate bounds within which the water levels at the GBO complex fall.

Unlike the Kornwerderzand intertidal flat, the direction of the water level gradient is not uniform at the GBO complex. Due to the geometry of the complex, there are water level gradients to the north and to the south of the Griend island as the tidal flood wave enters (Figure 6.12a). This causes the tidal flood wave to branch into the major tidal channels to the north and to the south. While water levels are low, the relatively high elevation and shoal-like geometry of the GBO complex largely prevent the exchange of water between both major tidal channels. The tidal flood wave is pushed up towards the back of the basin. The tidal flood wave in the southern tidal channel is pushed up more than the tidal flood wave in the northern tidal channel. Once water levels exceed the bed level of the GBO complex, this causes a uniform northwest-directed water level gradient. Whereas water level gradients at the Kornwerderzand intertidal flat are uniformly flood- and ebb-directed, the shoal-like geometry and relatively high bed elevation of the GBO complex cause an additional water level gradient once water levels exceed the intertidal flat bed.

The water level differences that develop at the GBO complex are larger than at the Kornwerderzand intertidal flat. The size of the GBO complex, however, is also larger than that of the Kornwerderzand intertidal flat. To investigate the impact of water level differences on the flow pattern, the water level differences have to be coupled to the water level gradient. The exact directions of water level gradients at both intertidal flat complexes are hard to study as these depend on the exact flow pattern on the intertidal flat. The water level gradients are crucial in dictating the flow velocity on the intertidal flat. The impact of water level gradients on flow velocities is more straightforward to study. Figure 6.14 is a scatter plot of all Kornwerderzand and GBO complex 20mx20m bed pixel elevations located above MLW[2], against the mean flow velocity at this location over the tidal cycle. The general trend is that flow velocities at similar bed elevations are larger at the GBO complex. This suggests that the combination of larger water level differences and larger intertidal flat size leads to larger water level gradients at the GBO complex than at the Kornwerderzand intertidal flat.

At t_5, HW just occurred near the tidal inlet but is yet to occur for most of the tidal basin. About 1.5 hours later, HW occurs near the coast. Around t_5, the uniform water level gradient reverses (Figure 6.12e). This results in ebb-oriented flow velocities on the intertidal flat while flow velocities in the tidal channels are still flood-oriented (Figure 6.11e, Figure 6.11f). This is similar to what took place at the Kornwerderzand intertidal flat.

The important role of gullies in conveying discharge onto the intertidal flat during flood and from the intertidal flat during ebb is comparable to that observed at the Kornwerderzand intertidal flat. This is demonstrated in Figure 6.15. A specific discharges of 0.3 m^3/s/m' flows through gully transect GBT2 roughly 1.5 hours before substantial discharges flow over the edge of the intertidal flat. A specific discharge of on average 0.1 m^3/s/m' keeps flowing through the gully for about an hour after the specific discharge over the edge of the intertidal flat decreases to zero.

[2]Average LW at the Kornwerderzand measuring station over the validation period (-0.93m NAP).

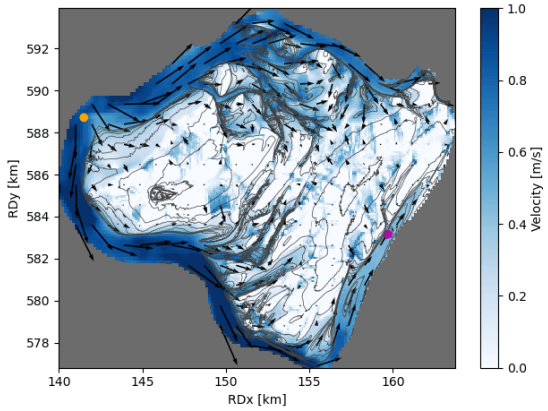

(a) t_1: Ca. 2 hours after LW.

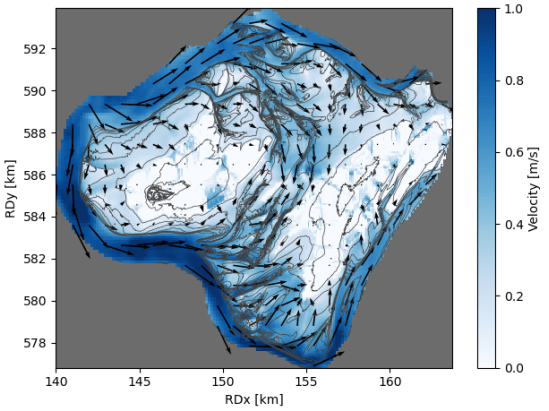

(b) t_2: Rising tide.

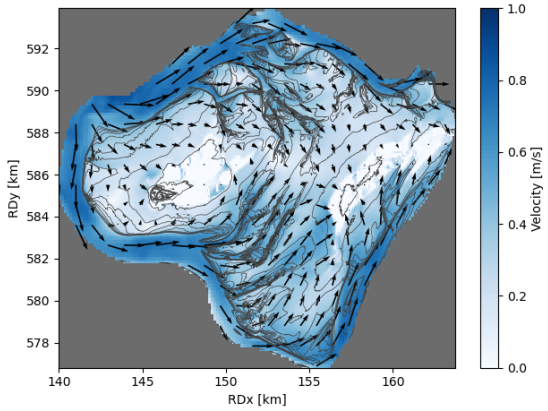

(c) t_3: Ca. 2 hours before HW.

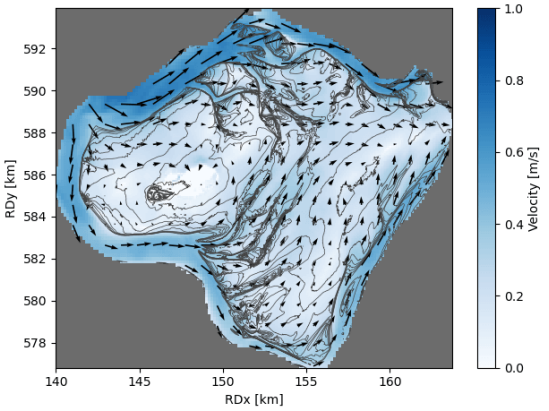

(d) t_4: Just before HW near the tidal inlet.

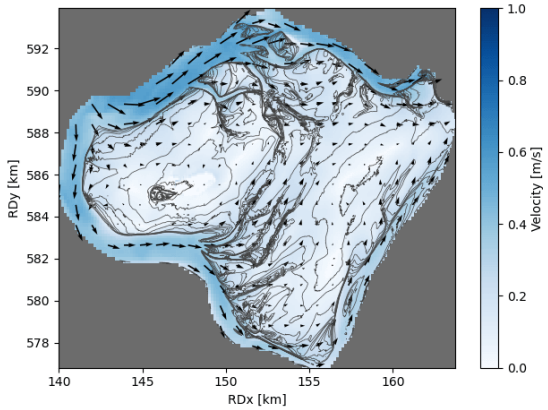

(e) t_5: Just after HW near the tidal inlet.

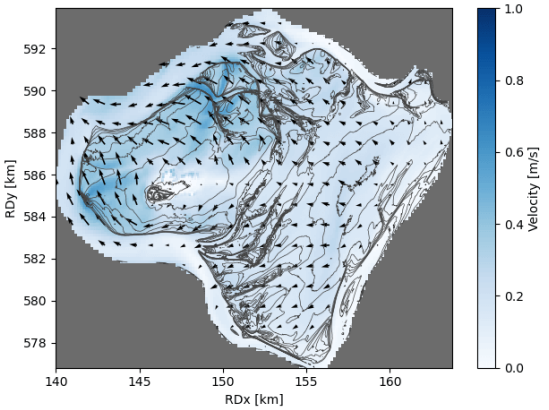

(f) t_6: Just after HW near the coast.

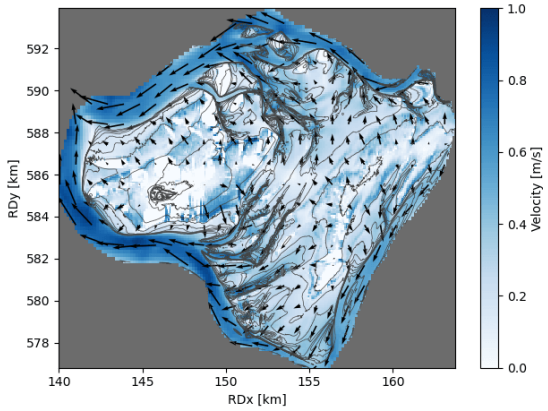

(g) t_7: Falling tide.

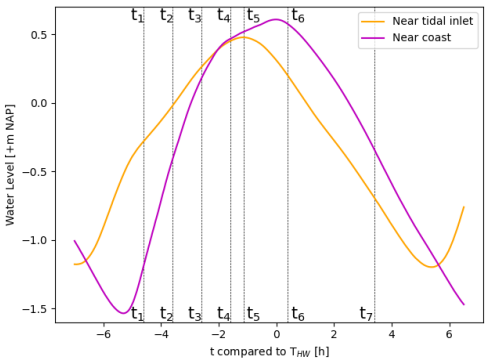

(h) Overview of instances in the tidal cycle at which snapshots are shown. Locations shown in subfigure a. HW-mark defined as HW near coast.

Figure 6.11: Snapshots of vector velocities at the GBO complex at different moments in AT, along with an overview of the instances in the tidal cycle at which snapshots are shown.

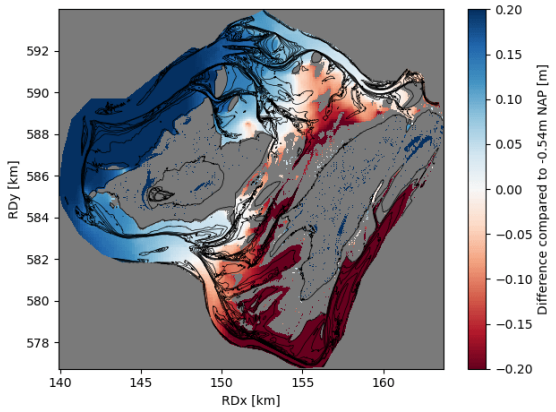

(a) t_1: Ca. 2 hours after LW.

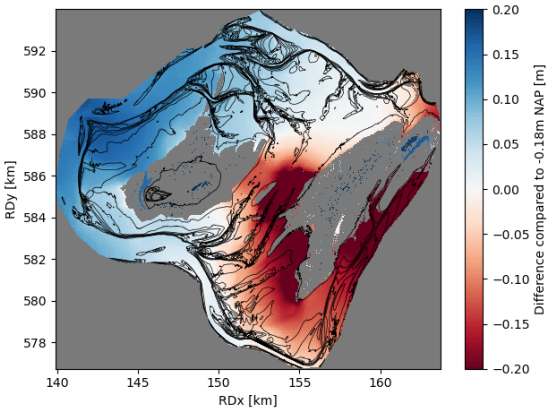

(b) t_2: Rising tide.

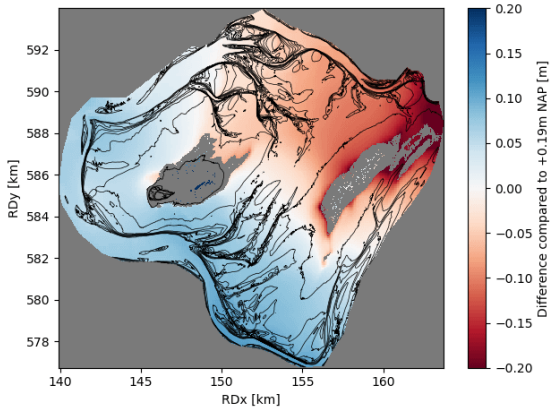

(c) t_3: Ca. 2 hours before HW.

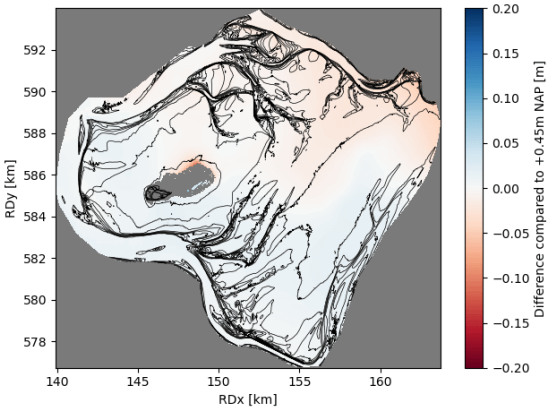

(d) t_4: Just before HW near the tidal inlet.

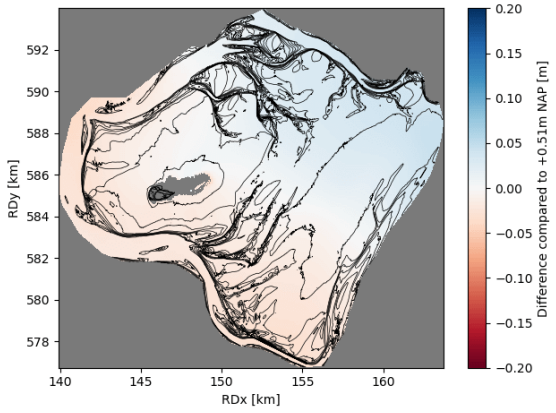

(e) t_5: Just after HW near the tidal inlet.

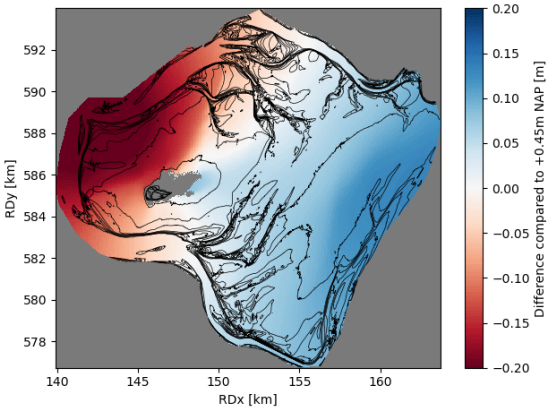

(f) t_6: Just after HW near the coast.

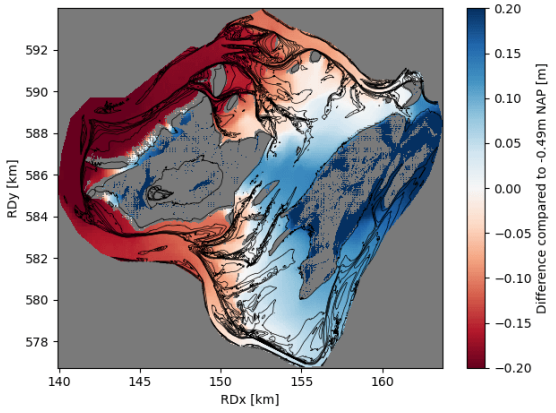

(g) t_7: Falling tide.

Figure 6.12: Snapshots of water level differences compared to the mean water level at the GBO complex at different moments in AT. Figure 6.11h gives an overview of the instances in the tidal cycle at which snapshots are shown.

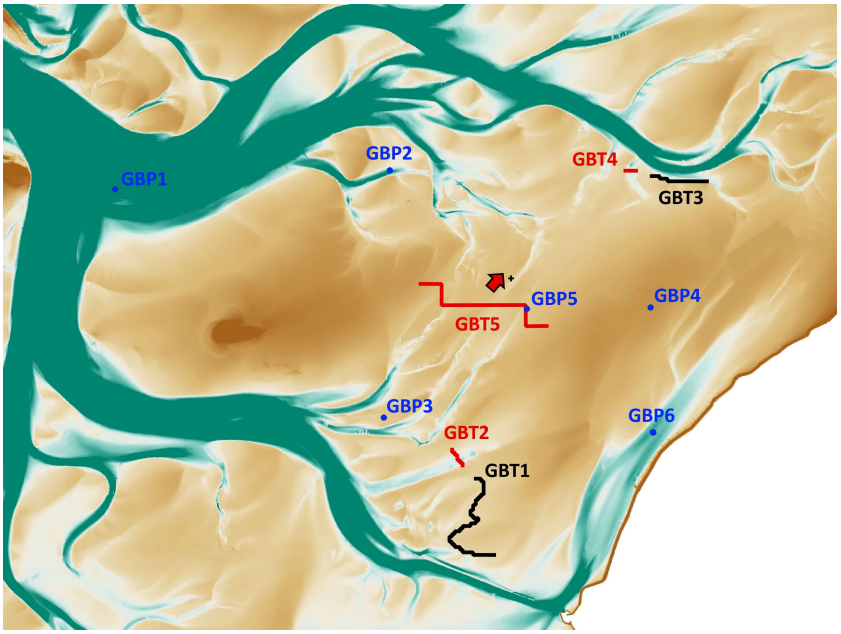

Figure 6.13: Location at which transects and measurement points are placed. GBT1 and GBT3 placed at the MLW[3] contour. GBT2 and GBT4 placed in a gully. GBT5 placed at the approximate location where flow from the north and south meet. Flow onto the intertidal flat defined as positive.

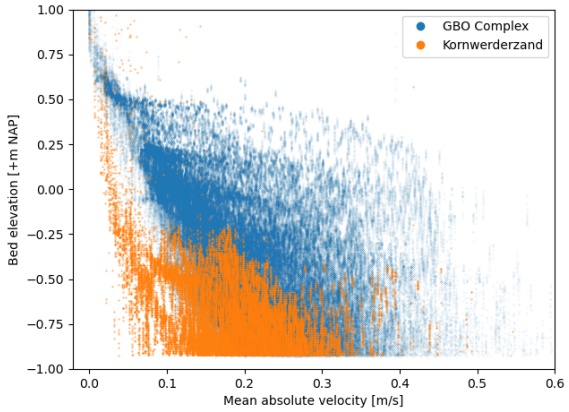

Figure 6.14: Scatter plot of bed elevation against mean absolute velocity over the tidal cycle at the Kornwerderzand and GBO intertidal flats complexes in AT.

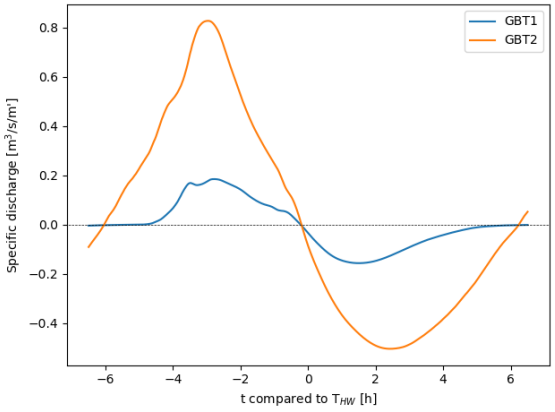

Figure 6.15: Specific discharge through southern edge transect GBT1 and southern gully transect GBT2 in AT.

Specific discharges across the other transects, exposure times, and the influence of the spring-neap tidal cycle on discharges, velocities, water levels, and exposure times at the GBO complex are shown in Appendix J. The behavior is very similar to what has been shown at the Kornwerderzand intertidal flat.

6.3. Effect of wind forcing on horizontal flow patterns

Scenarios Westerly Wind (WW) and Easterly Wind (EW) are compared with AT at the GBO complex to investigate how wind forcing alters flow patterns on intertidal flats. AT serves as a reference without wind forcing. To demonstrate how wind forcing alters the tidally driven horizontal flow patterns, snapshots of water level differences compared to the mean water level in the GBO sub-domain at t_5 (Figure 6.11h) are shown in Figure 6.16. In the situation without wind, the water level gradient at this

[3]Average LW at the Harlingen measuring station over the validation period (-1.03m NAP).

moment in time was oriented to the northeast (Figure 6.12e). The water level difference between the northeast and the southwest of the domain was <0.1m. The direction of the water level gradient in WW is northwest. The direction of the water level gradient in EW is to the southeast. In both EW and WW, the water level difference between northwest and southeast is roughly 0.25m. The distance between the northwest and southeast of the domain is similar to the distance between the southwest and northeast of the domain. This means that the water level gradient is steeper in WW and EW than in AT. Furthermore, the mean water level of WW and EW at t_5 differs by 0.34m (y-label of Figure 6.16). Westerly wind causes basin-scale water level set-up, and easterly wind causes basin-scale water level set-down. Wind forcing of 15 m/s completely alters the hydrodynamics at the GBO complex.

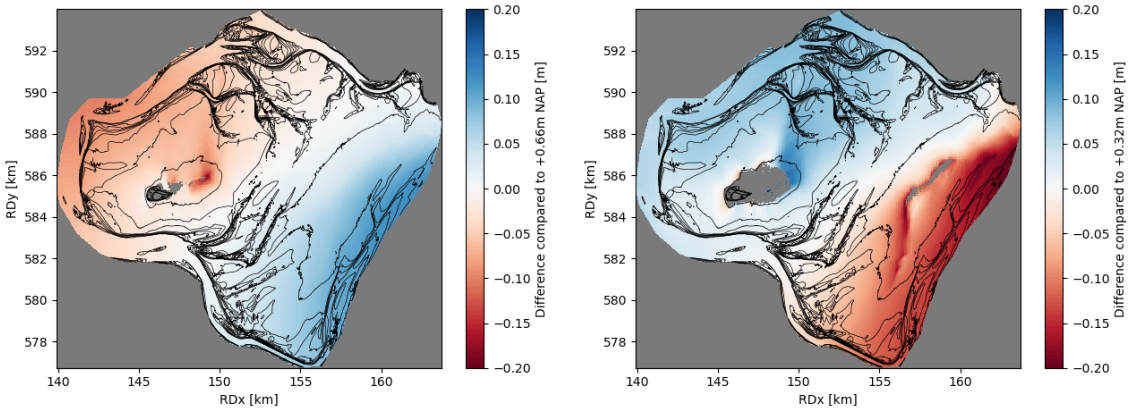

(a) Scenario WW. **(b)** Scenario EW.

Figure 6.16: Water level differences compared to the mean water level at t_5 at the GBO complex in EW and WW.

Without wind forcing, a water level gradient towards the northeast is created once water levels exceed the bed level (Figure 6.12c). This leads to northeastern flow. Westerly wind enhances the northeastern flow over the complex (Figure 6.18). This leads to higher flood discharges onto the complex at the southwestern edge and gullies (Figure 6.17a). At the northeastern edge and gullies, ebb discharges off of the complex are enhanced. (Figure 6.17b). There is also a substantial increase in northeastern flow through transect GBT5. Overall, westerly wind amplifies the discharges to the northeast. Easterly wind opposes the northeastern-directed water level gradient. The direction of velocities on the intertidal flat turns to the west/southwest during most of the tidal cycle (Figure 6.19). The discharge over the northeastern edge increases during flood, and the discharge over the southwestern edge increases during ebb. The discharge through transect GBT5 is to the southwest for the entire tidal cycle. Easterly wind reduces discharge to the northeast, possibly even reversing the net discharge direction to the southwest. Wind significantly impacts the moment that the flow direction through the edge transects switches sign. The discharge through edge transect GBT1 in WW is directed onto the intertidal flat for 4 hours longer than in EW (Figure 6.17a). Similarly, the direction of the discharge through edge transect GBT3 in EW does not even reverse (Figure 6.17b). This means that wind has a pronounced effect on how water discharge (along with the sediment it carries) enters and leaves the intertidal flat.

The detailed flow pattern is studied at several points. Timeseries of water levels, flow velocities, and flow directions are shown in Figure 6.20c. The impact of wind on the water levels at a location mainly follows from basin-scale water level set-up or set-down. At GBP1, which is close to the tidal inlet, the impact of wind on water levels is small. At locations GBP3 and GBP4, a substantial impact of wind is discerned in the water level timeseries. At all locations, wind impacts the evolution of velocities over the tidal cycle. At GBP1 and GBP2, the flow direction remains unchanged, but velocities are altered. GBP2 is in a gully which is oriented to the west. The flow direction still aligns with the channel axis, but the timing of flow reversal in WW and EW differs by 1.5 hours. At GBP3 and GBP4, wind has a substantial impact on velocity and direction. On the lower intertidal flat (GBP3), the velocity and direction in WW and EW are altered compared to AT but still show some resemblance. There is a moment of flow reversal, and clear velocity peaks occur during flood and ebb. However, the timing of flow reversal in

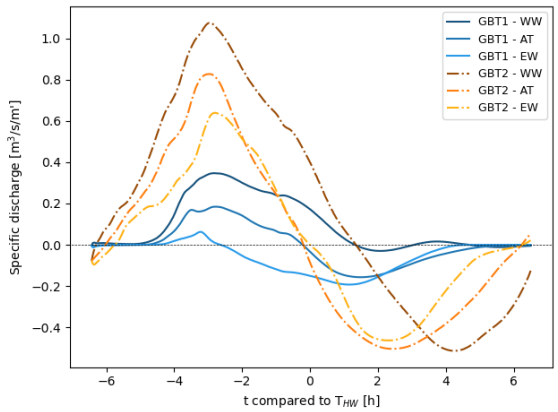

(a) Southern edge transect GBT1 and southern gully transect GBT2.

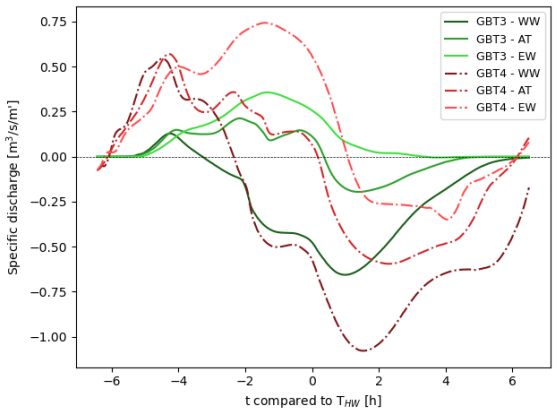

(b) Northern edge transect GBT3 and northern gully transect GBT4.

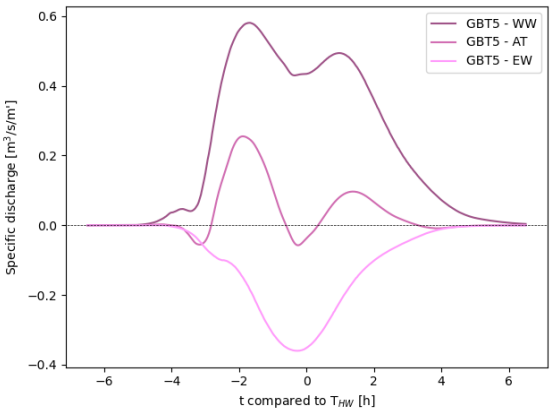

(c) Middle gullies transect GBT5.

Figure 6.17: Discharge through several transects at the GBO complex in AT, WW, and EW. Exact locations indicated in Figure 6.13.

WW and EW differ by 3.5 hours. On the upper intertidal flat (GBP4), wind forcing completely changes the direction of flow for the entire period that the location is wet. Velocities in the simulations with wind (of 15 m/s) are around 0.5 m/s, which is significantly larger than the ca. 0.1 m/s in the reference.

The effect that wind forcing has on exposure times is studied. Figure 6.20b exemplifies that the basin-scale water level set-down during easterly wind does not necessarily increase exposure times on the entire GBO complex. Exposure times to the east of the Griend island decrease, as this area is inundated for longer by water that is pushed up against the island through easterly wind shear. There are several other patches where exposure times increase. This shows that not only the presence of islands or coasts but also the intertidal flat geometry has an effect on the detailed wind-driven flow pattern. During westerly wind, sheltering of the Griend island prevents substantial water level set-up to the east of the Griend island (Figure 6.20a). The general pattern of exposure times with wind forcing follows from basin-scale water level set-up/set-down. However, the combination of wind-driven basin-scale water level set-up/set-down and flow caused by wind shear increases the variability in exposure times compared to the situation without wind.

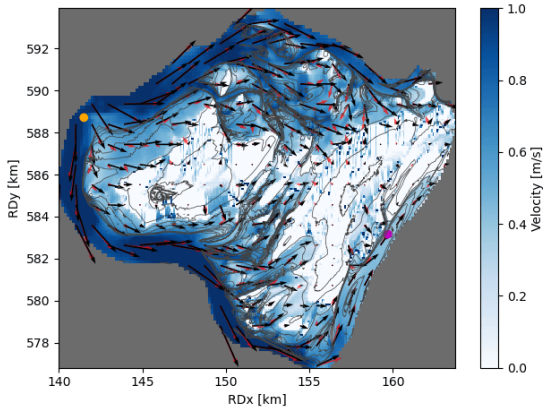

(a) t_1: Ca. 2 hours after LW.

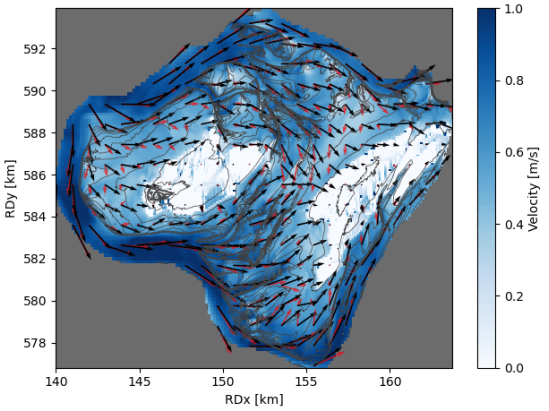

(b) t_2: Rising tide.

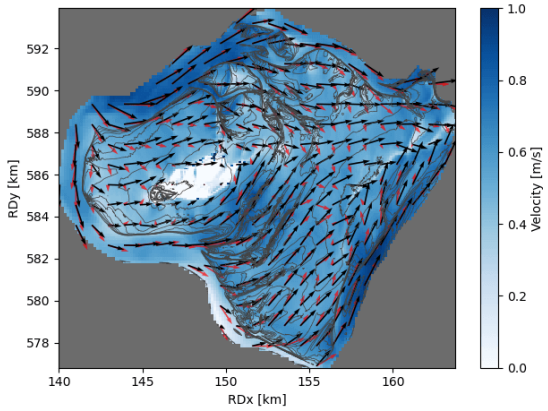

(c) t_3: Ca. 2 hours before HW.

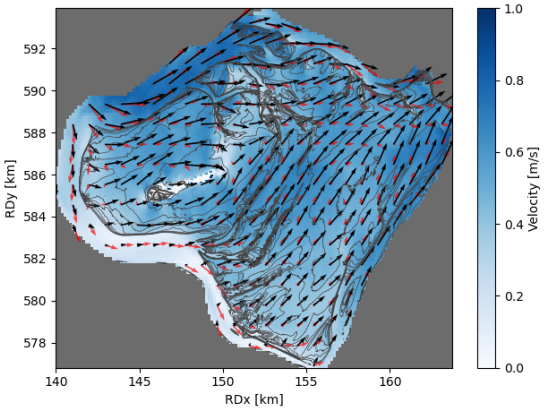

(d) t_4: Just before HW near the tidal inlet.

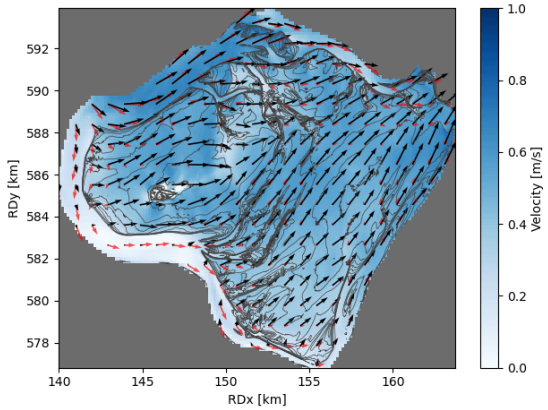

(e) t_5: Just after HW near the tidal inlet.

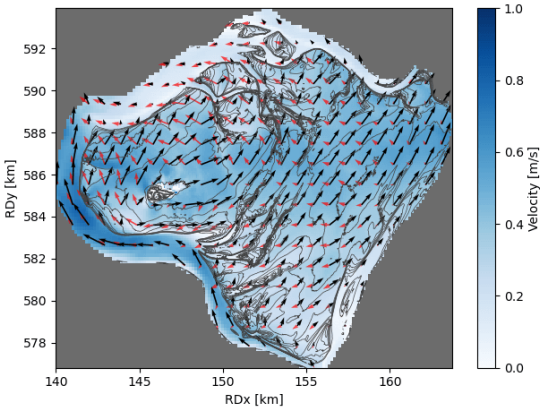

(f) t_6: Just after HW near the coast.

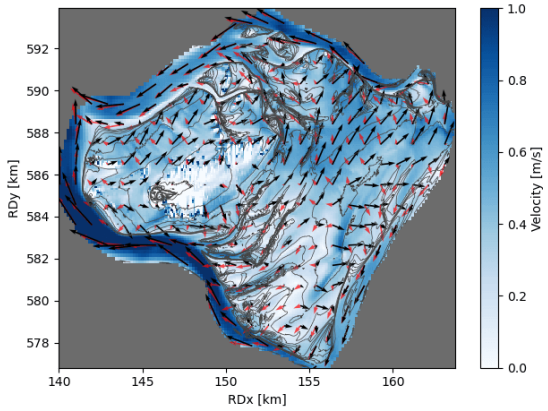

(g) t_7: Falling tide.

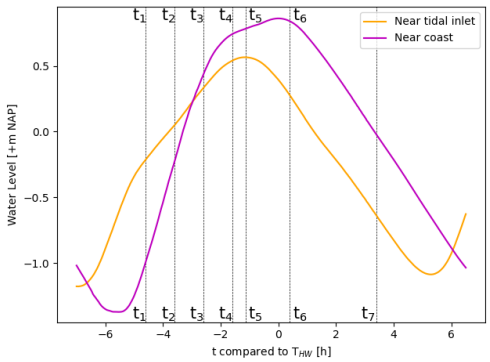

(h) Overview of instances in the tidal cycle at which snapshots are shown. Locations shown in subfigure a. HW-mark defined as HW near coast.

Figure 6.18: Snapshots of vector velocities on the GBO complex at different moments, along with an overview of the instances in the tidal cycle at which snapshots are shown. Velocity vectors in reference scenario AT indicated in red; velocity vectors in WW indicated in black.

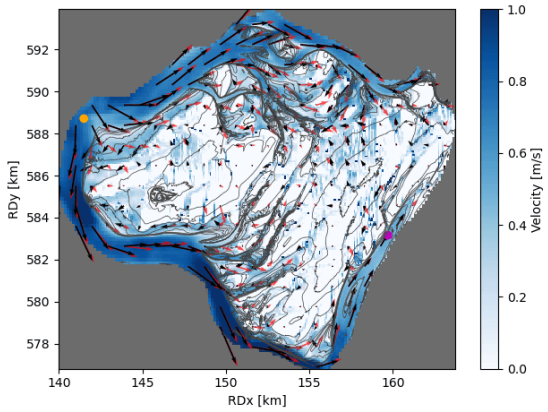

(a) t_1: Ca. 2 hours after LW.

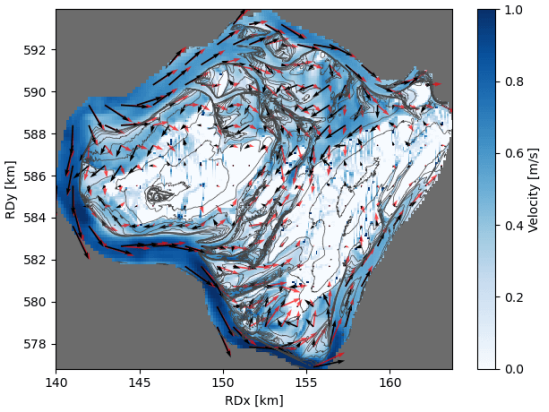

(b) t_2: Rising tide.

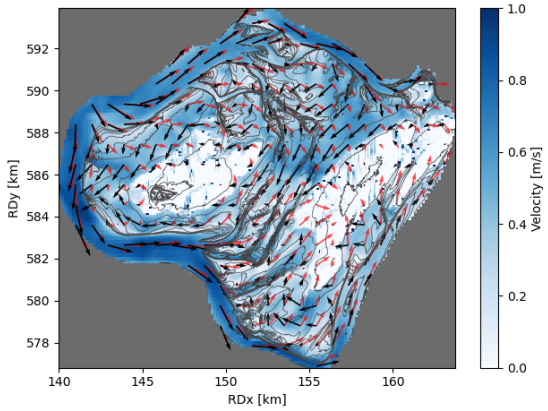

(c) t_3: Ca. 2 hours before HW.

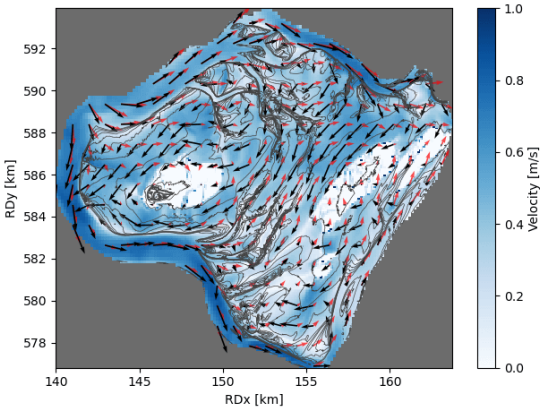

(d) t_4: Just before HW near the tidal inlet.

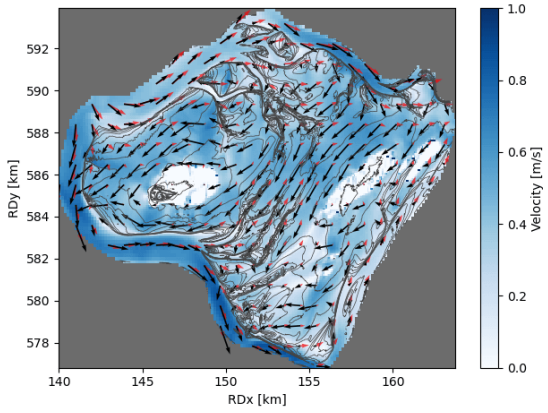

(e) t_5: Just after HW near the tidal inlet.

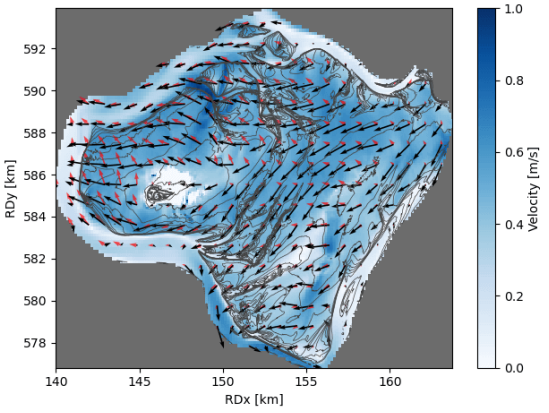

(f) t_6: Just after HW near the coast.

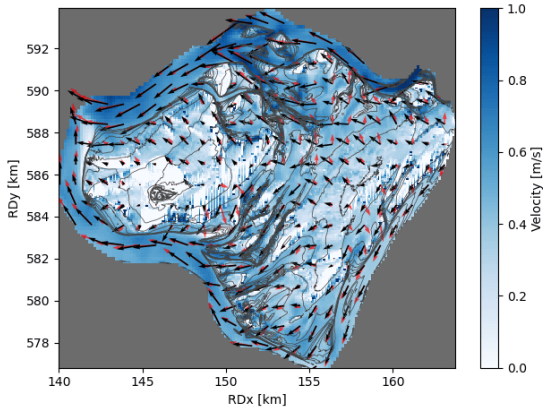

(g) t_7: Falling tide.

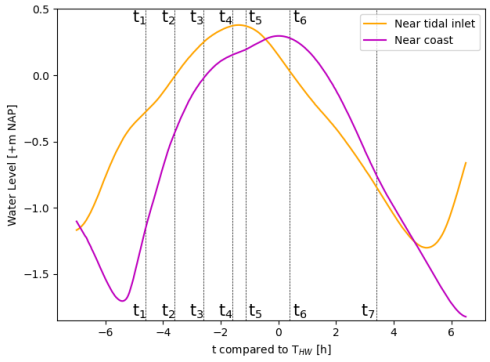

(h) Overview of instances in the tidal cycle at which snapshots are shown. Locations shown in subfigure a. HW-mark defined as HW near coast.

Figure 6.19: Snapshots of vector velocities on the GBO complex at different moments, along with an overview of the instances in the tidal cycle at which snapshots are shown. Velocity vectors in reference scenario AT indicated in red; velocity vectors in EW indicated in black.

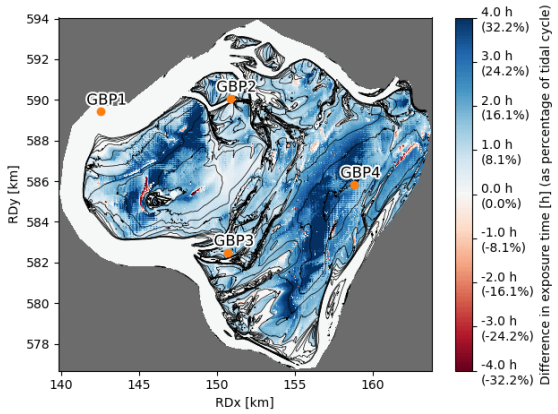

(a) Difference in exposure time between AT and WW. Positive values indicate AT has a longer exposure time. Subfigure c locations indicated for reference.

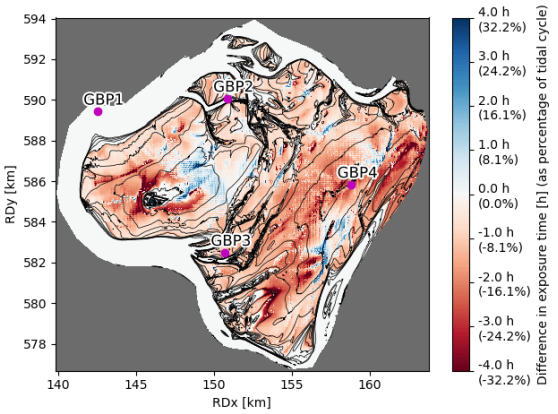

(b) Difference in exposure time between AT and EW. Positive values indicate AT has a longer exposure time. Subfigure c locations indicated for reference.

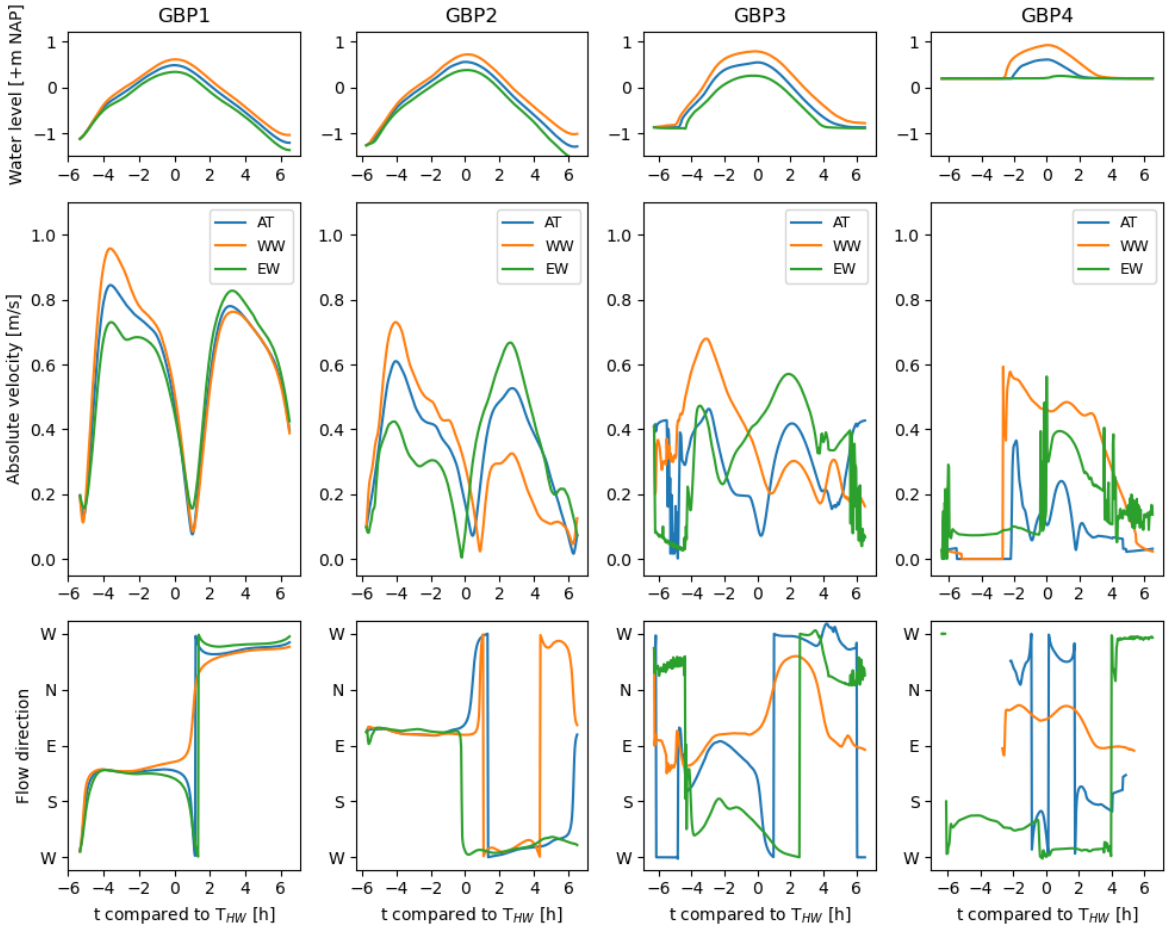

(c) Water levels and velocities at GBP1 (tidal channel), GBP2 (gully), GBP3 (lower intertidal flat), and GBP4(upper intertidal flat). Locations indicated in subfigures a and b.

Figure 6.20: Spatial differences in exposure time at the GBO complex between (a) WW and AT, (b) as well as EW and AT, (c) along with point measurements of velocity, water levels, and flow direction in AT, WW, and EW.

7

Interpretation & Discussion

Findings about the tidally- and wind-driven flow patterns on intertidal flats are synthesized based on the results in chapter 6. The validity of the applied method and the use of subgrid modeling technique are discussed.

7.1. Synthesis of flow patterns on intertidal flats

Horizontal flow patterns on intertidal flats were studied by assessing water levels, discharges, exposure times, and velocities. This study showed that the horizontal flow patterns on non-fringing intertidal flats depend on various aspects: intertidal flat geometry (i.e. size, bed elevation, and degree to which the intertidal flat is intersected by tidal channels), hydraulic boundary condition (i.e. phase of the spring-neap tidal cycle, asymmetry of the tidal wave), and wind forcing.

Intertidal flat geometries in the western Dutch Wadden Sea vary. The Kornwerderzand and GBO intertidal flat complexes were studied. The Kornwerderzand intertidal flat is small compared to the Marsdiep basin (about 1/10th of surface area), has bed elevations such that it fully submerges even during neap tide, and is heavily intersected by tidal channels. The GBO complex is large compared to the Vlie basin (about 1/4th of surface area), has bed elevations such that it barely submerges even during average tides, and shoal-like geometry. Flow patterns at the Kornwerderzand and GBO intertidal flat complexes differ due to their different geometries.

When water levels are low, the tidal flood wave branches into the tidal channels surrounding the intertidal flat. Shoal-like geometry and higher bed elevations prevent the exchange of water between surrounding tidal channels. Lower bed elevations and tidal channels that intersect the intertidal flat enable the exchange of water between the tidal channels. If exchange occurs between the tidal channels such that no significant difference in water levels develops, the flow direction follows the basin-scale water level gradient. (Figure 7.1a). If little exchange occurs between the tidal channels, a significant difference in water levels develops. Once water levels exceed intertidal flat elevation, a water level gradient arises that causes flow (Figure 7.1b). The magnitude of water level gradients is determined by the interplay of the water level differences between tidal channels surrounding the intertidal flat, and the size of the intertidal flat. For similar water level differences, larger intertidal flat size results in smaller water level gradients, leading to smaller flow velocities (Figure 7.1c).

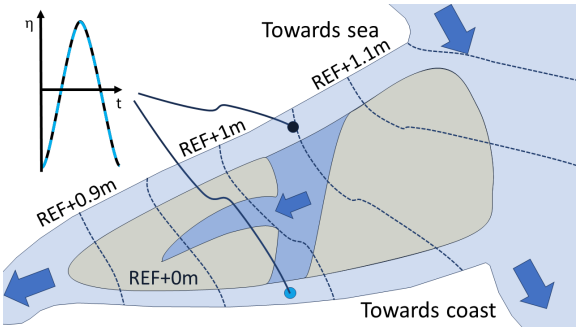

(a) Lower bed elevations and channel-intersected geometry. Water levels in the tidal channels surrounding the intertidal flat do not differ as the intertidal flat geometry enables water exchange between the tidal channels. Water flow follows the basin-scale water level gradient.

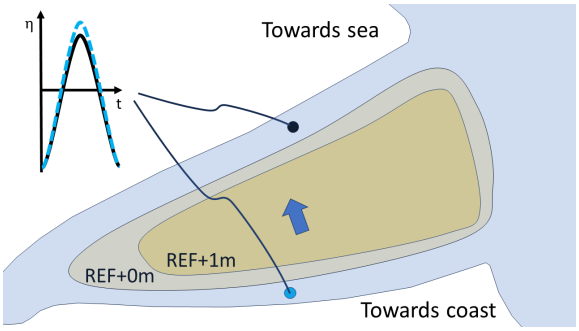

(b) Higher bed elevations and shoal-like intertidal flat geometry. Water levels in the tidal channels surrounding the intertidal flat differ as the intertidal flat geometry prevents water exchange between the tidal channels. Once the water level exceeds the intertidal flat, water flow follows the water level gradient.

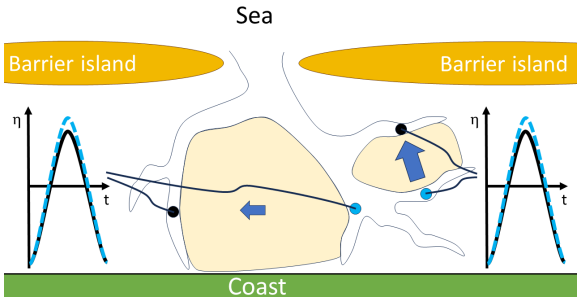

(c) Flow over intertidal flats with different sizes. The water level differences at both locations are similar. Flow velocities over the larger intertidal flat are smaller as water level gradients are smaller due to its size. Flow velocities over the smaller intertidal flat are larger as water level gradients are larger due to its size.

Figure 7.1: The impact on flow patterns of the geometrical characteristics of bed elevation, degree to which the intertidal flat is intersected by tidal channels, and size. Graphs show water levels over the tidal cycle. Colors of graph lines correspond to the colors of points indicating their location.

An additional effect of how flow interacts with the bed at different elevations was observed (Figure 7.2). The water level gradient changed to ebb-oriented before High Water (HW) occurred (both in the channels and on the intertidal flat). On the intertidal flat, flow turned to the ebb direction relatively quickly in response. The response in the tidal channel was slower. The flow turned to the ebb orientation 1.5 hours later, around HW. There is a phase difference in when the HW slack tide occurs on the intertidal flat and in surrounding channels. A possible explanation for the phase difference between HW slack at the intertidal flat and in the tidal channel is the relative importance of friction and inertia at the different locations. Water depths are relatively small on the intertidal flat, leading to a large relative importance of friction and a small relative importance of inertia. Water depths are relatively large in the tidal channel, leading to a small relative importance of friction and a large relative importance of inertia. An effect on sediment dynamics is exemplified. When HW slack occurs at the intertidal flat, suspended sediments settle on the intertidal flat. As the concentration of suspended sediments in the water column is now lower, less sediment settles in the tidal channel once HW slack occurs there. While this is definitely not the only mechanism to impact sediment dynamics, the phase difference in HW slack tide has implications for the distribution of sediments throughout the tidal basin.

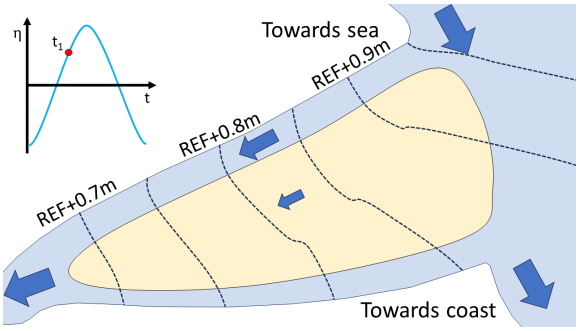

(a) t_1: Flood-directed flow in tidal channels and on the intertidal flat.

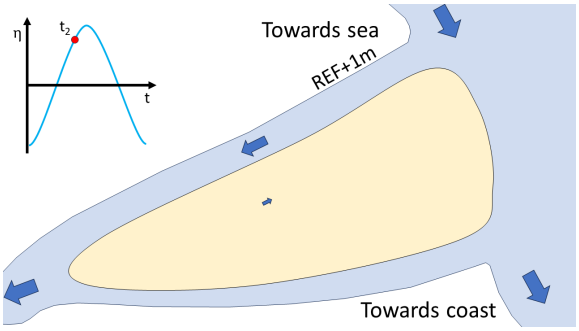

(b) t_2: Some time before HW, the water level gradient reverses to ebb-directed. Flow in tidal channels remains flood-directed while flow on the intertidal flat reverses.

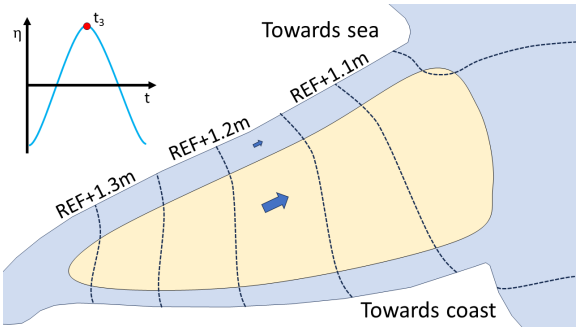

(c) t_3: As the ebb-directed water level gradient continues to steepen, flow in the tidal channel also reverses.

Figure 7.2: Phase difference in HW slack on the intertidal flat and in the tidal channel.

Four velocity peaks were observed over the tidal cycle at measurement points on the lower intertidal flat (Figure 7.3). These peaks occur due to: the large water level gradient when a location is just inundated, the large water level gradient when the rate at which the water level rises is maximal, the large water level gradient when the rate at which the water level falls is maximal, and the acceleration of water along bed level gradients just before drying. Thus, the first and last peaks follow from physics on the scale of an intertidal flat, while the second and third peaks follow from the basin-scale tide. The upper intertidal flat inundates after the maximum water level gradient has already occurred. Therefore, the first two velocity peaks coincide, and only three velocity peaks occur (Figure 7.3).

Measurements on a lower intertidal flat in the western Dutch Wadden Sea (Colosimo et al., 2020), but also measurements on other intertidal flats do not clearly show the first and last velocity peaks (e.g. Le Hir et al. (2000), de Vet et al. (2020), Zhu et al. (2022)). It is likely that the measurement equipment in the aforementioned studies was not able to register velocities in very shallow water layers. Nowacki and Ogston (2013) and Zhang et al. (2016) discuss these so-called 'velocity pulses'. Velocity pulses on intertidal flats occur at water depths of around <10 cm (Zhang et al., 2016). Nowacki and Ogston (2013) argue that their magnitude is determined by tidal range. The water and sediment fluxes caused by velocity pulses are small in comparison to total water and sediment fluxes over the tidal cycle (Zhang et al., 2016), implying minor importance for basin-scale morphodynamics. The exact interactions of velocity pulses with the bed are not well understood, mainly because of the difficulties of measuring in shallow water. Zhang et al. (2016) do infer that velocity pulses have a key role in the formation of the micro-topography (i.e. bedforms of ca. 1-2 cm high; 5-10cm long) of intertidal flats and possibly in tidal creek formation. As tidal creeks are important for hydrodynamics on the scale of the intertidal flats, velocity pulses may play an important role in the long-term morphological evolution of intertidal flats. As demonstrated in this study, subgrid modeling technique can estimate velocity pulses due to its automatic wetting and drying. For this estimate to be somewhat accurate, it is imperative that the water movement is validated adequately during the periods of the tide that *can* be measured. In that case, subgrid modeling technique could contribute to a better understanding of the forming processes behind tidal creeks and micro-topography of intertidal flats.

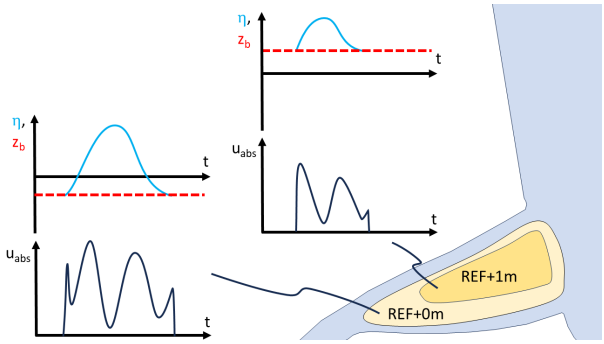

Figure 7.3: The difference in how absolute velocity develops over the tidal cycle at the lower and upper intertidal flat. Intertidal flat elevation indicated by red dashed line. Four velocity peaks occur on the lower intertidal flat, while only three velocity peaks occur on the upper intertidal flat.

Simulated flow patterns on intertidal flats in the western Dutch Wadden Sea differed over the spring-neap tidal cycle. Water level timeseries over the spring-neap tidal cycle do not oscillate around the same mean water level, even with barely any wind forcing. It is probable that the minimal wind forcing still has a notable effect on water levels in the western Dutch Wadden Sea (Figure 7.4a). The tidal range increases from neap tide to spring tide. The increased tidal range of a spring tide necessitates (in absence of other effects) larger rising and falling rates of the tide. Water level gradients, and consequently flow velocities on intertidal flats, increase (Figure 7.4b). The studied neap tide showed notably more symmetry in time than the average tide and spring tide (Figure 7.4b). A preliminary assessment of the measured tidal records suggests that tidal asymmetry increases from relatively symmetrical in time during neap tide to relatively asymmetrical during spring tide. Sediment transport scales with flow velocity to a certain power (Bosboom & Stive, 2021). Thus, morphological activity increases from neap tide to spring tide as flow velocities increase with the tidal range. There are implications for the morphological evolution of intertidal flats if there is in fact an increase of tidal asymmetry from neap to spring tide. Low morphological activity and a relatively symmetrical tidal signal during neap tides would lead the intertidal flat bed to remain largely the same. On the other hand, the combination of high morphological activity and a relatively asymmetrical tidal signal during spring tides would induce large changes to the intertidal flat bed. Guo et al. (2019) showed that there can be a structural difference in the tidal asymmetry at different phases of the spring-neap tidal cycle. As tidal asymmetry strongly depends on bathymetric characteristics, a study specific to the Wadden Sea is required. Verifying whether this mechanism exists helps extend the knowledge on the morphological evolution of intertidal flats.

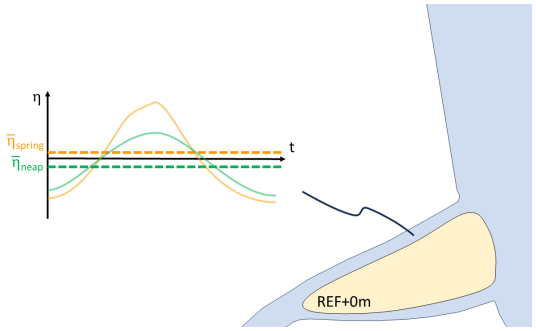

(a) The mean water level of tides ($\bar{\eta}$) differs over the spring-neap tidal cycle, even with barely any wind forcing. $\bar{\eta}_{spring}$ is higher than $\bar{\eta}_{neap}$ in this example. This is not necessarily the rule.

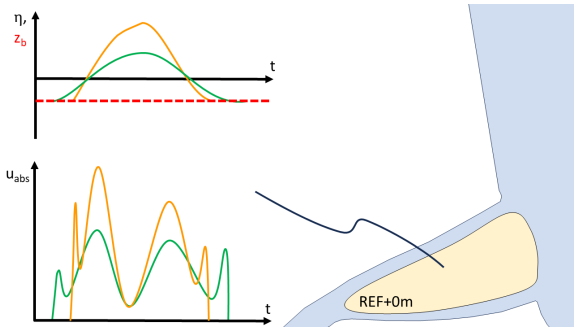

(b) Water levels and velocities on the intertidal flat during spring and neap tide. Intertidal flat elevation indicated by red dashed line. During the rising and falling tide, the water level gradient over the intertidal flat during spring tide is larger than during neap tide, leading to larger flow velocities on the intertidal flat.

Figure 7.4: Water levels and absolute velocities over a tidal cycle during a spring tide (orange) and neap tide (green). The water level timeseries of the spring tide is more asymmetrical than the neap tide.

In this study, unidirectional wind events of 15 m/s impacted the flow patterns on several different scales. On the basin scale, westerly wind caused water level set-up. The magnitude of set-up increased from the tidal inlet towards the coast. Similarly, easterly wind caused water level set-down. Colosimo et al. (2023) found that the basin-scale effect of wind-driven water level set-down plays an important role in the accretion of intertidal flats. Water level set-down enables longer aerial exposure of intertidal flats. The bed can consolidate longer, possibly leading to over-consolidation. This increases shear strength against erosion. As demonstrated in this study, basin-scale water level set-down does not necessarily increase exposure time at the entire intertidal flat, due to the role that wind shear on the scale of the intertidal flat plays. This implies that wind shear plays a significant role in enabling and preventing the over-consolidation process. It would be beneficial to further the knowledge on its impact on the long-term predictive capacity of morphological models.

On the scale of an intertidal flat, wind shear caused a substantial shift in how water enters and leaves the intertidal flat (Figure 7.5a). Over the edge in the direction from which the wind blew, more water entered the intertidal flat during flood, and less water left during ebb. Over the edge in the direction towards which the wind blew, less water entered the intertidal flat during flood, and more water left during ebb. Wind had an additional impact on the scale of the intertidal flat, which differed with bed elevation (Figure 7.5b). The effect on flow increased for smaller water depths. On the upper intertidal flat, wind forcing completely altered the direction and magnitude of velocities. On the lower intertidal flat, the direction and magnitude of velocities were altered, but not as much as on the upper intertidal flat. On the scale of a gully, wind events that aligned with the orientation of a gully substantially altered the flow velocities over the tidal cycle. In de Vet et al. (2018), a wind event perpendicular to the gully was ineffective at altering the flow pattern, especially peak flow velocities. The orientation of gullies determines how effective wind is at altering the flow in a gully (Figure 7.5c).

Research has been carried out on the effect of varying wind forcing on basin-scale hydrpdynamics (Duran-Matute et al., 2016; van Weerdenburg et al., 2021). On the scale of intertidal flats, the impact of varying wind magnitude on the flow pattern on intertidal flats was mainly studied (Colosimo et al., 2020; de Vet et al., 2018). In the present study two unidirectional wind events were analyzed. Findings do not not generalize to the impact of directionally varying wind forcing on flow patterns on intertidal flats. More research is required into how directionally varying wind forcing alters hydrodynamics and consequently the morphodynamics on the scale of an intertidal flat.

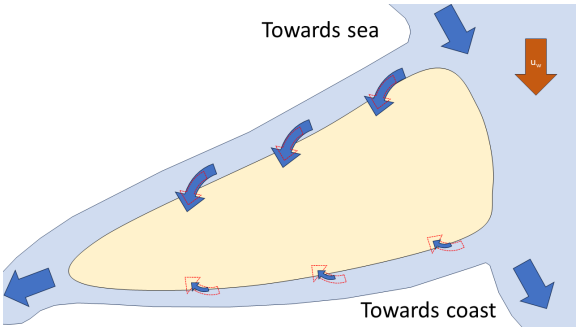

(a) Shift in how water discharge enters the intertidal flat during the rising tide because of wind forcing. More discharge flows over the edge in the direction from which the wind blows; less discharge flows over the edge towards which the wind blows. The reverse holds for the falling tide.

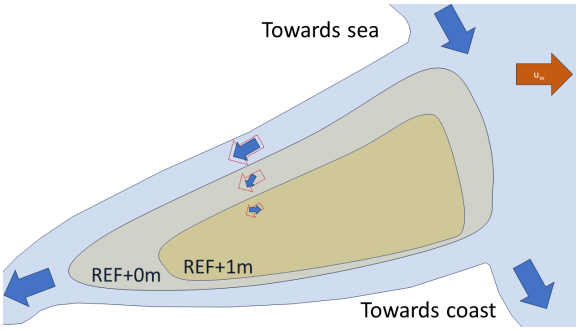

(b) The impact of wind forcing depends on bed elevation. In tidal channels, wind has a lesser impact. On the lower intertidal flat, wind starts substantially impacting the flow pattern. On the upper intertidal flat, wind can completely alter the flow pattern.

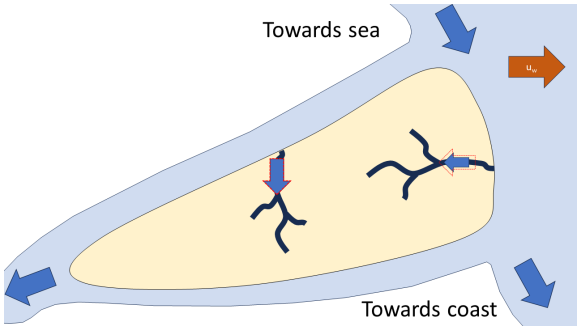

(c) The impact of wind forcing on flow through gullies depends on gully orientation. If wind forcing aligns with the gully axis, the impact is large. If wind forcing is perpendicular to the gully axis, the impact is small.

Figure 7.5: The effect of wind on several aspects of flow on intertidal flats. Wind forcing indicated in orange. Currents without wind forcing indicated by transparent arrows with dashed red outline.

It is speculated to what extent findings apply to the eastern Dutch, German, and Danish Wadden Sea. The ASMITA model accurately predicts the morphological system behavior of tidal basins both in the western and eastern Dutch Wadden Sea using the same empirical relationships with different parametrizations (e.g. Huismans et al. (2022)). It is hypothesized that as aggregated system behavior is similar, the underlying hydrodynamic processes in the western and eastern Dutch Wadden Sea are similar to some degree. Differing characteristics are that the eastern Dutch Wadden Sea is shallower, and the ratio of horizontal area of intertidal flats to horizontal area of tidal channels is larger than in the western Dutch Wadden Sea (Lodder et al., 2022). This leads the tidal flood wave to interact differently with the tidal basin than in the western Dutch Wadden Sea (i.e. the hydraulic boundary condition differs). Intertidal flats in the eastern Dutch Wadden Sea generally have shoal-like geometry and higher bed elevations (i.e. intertidal flat geometry differs). As some aspects that are relevant to the flow pattern differ, it is expected that the detailed flow pattern differs from that in the western Dutch Wadden Sea while still following the same general pattern. By extension, the same is expected in the German and Danish Wadden Sea as some bathymetric and hydraulic characteristics relevant to the flow pattern differ. Additional research is required to assess the detailed flow pattern in the rest of the Wadden Sea.

The applicability of findings to similar estuarine settings is explored through a comparison to the research of de Vet et al. (2018). The studied flow patterns on intertidal flats in the western Dutch Wadden Sea show similarities to the flow patterns on the Roggenplaat intertidal flat in the Eastern Scheldt. The characteristic that both study sites share is that large tidal channels surround the intertidal flat. During mild wind conditions, the flow direction at the Roggenplaat becomes ebb-oriented before HW, similar to what was observed in this study. At both locations, the flow over the intertidal flats was mainly caused by wind during harsher wind conditions. This shows that findings can be extended to some degree to estuarine areas with similar characteristics, even when hydrodynamic boundary conditions differ.

In this discussion, findings pertaining to the flow pattern are related to morphodynamics. However, flow is not the sole driver of morphological change. Waves, freshwater influx, biological processes, North Sea sediment concentration, and dredging activities also affect the Wadden Sea morphological development (Herman et al., 2018). Knowledge on the impact of the flow pattern on morphodynamics should thus not be considered in isolation, but in the context of the combined mechanisms responsible for morphological development.

7.2. Model considerations

The large-scale water movement in the western Dutch Wadden Sea was accurate to the order of a single decimeter. For this to be possible, the bulk hydrodynamics on intertidal flats had to be relatively accurate. Therefore, it is expected that improvements to model accuracy could only alter the local flow patterns. An unresolved modeling issue is that the tidal range in the North Sea is slightly underestimated, likely due to excessive numerical damping. Probable sources of the excessive numerical damping are the boundary condition implementation and the 1st order accuracy of the advection scheme. Further research is required to point out the cause of this inaccuracy.

Besides fixing the underestimation of the North Sea tidal range, additional improvements to model accuracy are possible. Due to the time scope of this project, the extent of the calibration was limited. It is very probable that model parametrizations exist in which simulated large-scale water movement is more accurate. Besides this, there are gains to be made in the model implementation. In setting up the hydrodynamic model, some processes were omitted or simplified due to: the equations and assumptions used in the model discretization (e.g. Coriolis, 3-dimensional effects, waves, spatially varying wind forcing), data availability (e.g. freshwater inflows), and lesser importance for overall results (e.g. precipitation, water level set-up due to atmospheric depression). This leads to errors in how well water flow is represented. More accurate model results can be attained by improving the implementation of some or all of these processes. Most notably, density-driven flows were shown to affect the flow patterns in tidal channels near the studied intertidal flats (Schulz and Gerkema (2018), Smits et al. (2022)). The magnitude of density-driven flow scales with water depth. Because the water depths on intertidal flats are smaller than in tidal channels, a smaller impact is expected on the flow pattern on intertidal flats than in tidal channels. Nevertheless, it is probable that this omission leads to some inaccuracies in the simulated flow pattern. Besides this, the largest improvements to model accuracy can still be gained from a more extensive calibration.

A more extensive validation of flow on intertidal flats is required to improve the reliability of the claims that were made. For example, a subgrid-based model could be validated using the measurements from the 2017 Kustgenese 2.0 campaign in the Dutch Wadden Sea (van Prooijen et al., 2020). Still, measurement locations in this campaign were submerged for at least ca. 90% of the time (van der Werf et al., 2019). Another candidate is measurements from Colosimo et al. (2020). This campaign was limited to two locations on a fringing intertidal flat. To adequately validate a model with which to provide insight in flow patterns (and subsequently morphodynamics) on intertidal flats, additional velocity and water level measurements are required at locations with lower submergence times.

Former studies (e.g. Sehili et al. (2014)) compared subgrid modeling technique to simulations without subgrid on the domain scale. The present study performs a comparison on the scale of an intertidal flat. Where bed level gradients and complex flow around bathymetric features shape the flow pattern, subgrid simulations outperformed simulations with interpolated bathymetry with the same computational grid resolution. Nevertheless, the differences between the simulations on interpolated bathymetry and with subgrid (on the same computational grid resolution) were relatively small. In part, the comparatively accurate flow patterns in both the subgrid and interpolated simulations are due to the relatively high resolution (80mx80m) compared to the reference simulation (20mx20m). Volp (2017) demonstrated in the estuarine setting of the Western Scheldt that when increasing the computational cell size, subgrid simulations were still relatively accurate compared to the higher-resolution reference simulation. The accuracy of simulations on interpolated bathymetry decreased faster. It follows that the differences between the subgrid and interpolated simulations in the present study would increase for larger cell sizes.

It is not strictly correct to indicate the comparisons between scenarios Average Tide and Interpolated Bathymetry (or Higher-Resolution) as a comparison between subgrid and non-subgrid simulations. In the simulations 'without subgrid', the bed profile is interpolated to the computational cell size. However, automatic wetting and drying, which is part of subgrid modeling technique, is still present in these simulations. If a non-subgrid model with a wetting-and-drying algorithm was used, the velocity evolution would differ. For example, at some measurement points, the simulations on interpolated bathymetry showed velocity pulses just after inundating and just before drying. A model with the element removal algorithm might not show these velocity pulses at all, because computational cells with shallow water layers would be categorized as 'dry'. Other wetting-and-drying algorithms could face other difficulties regarding mass conservation, accuracy, and computational efficiency (Table 2.1). Another example is how it was possible to study the effect of wind on a shallow water layer on the upper intertidal flat. This demonstrates that the automatic wetting and drying, which was not explicitly studied in this report, is crucial for capturing the flow patterns on intertidal flats. Future studies in which flow patterns in shallow water layers are important should consider using subgrid modeling technique. Potential applications could be studies on how sediment transport is affected by wind in shallow water layers, ecological studies into exposure times of intertidal flats (e.g. Ecotopenkaart (Baptist et al., 2016)), studies into the dispersal of plastic particles including how these deposit in the intertidal zone.

As mentioned above, in the simulations 'without subgrid', the bed profile is interpolated to the computational cell size, but wetting and drying is automatic as in subgrid modeling technique. The differences in the simulated flow patterns can then be linked to the difference in how friction is resolved, and the cross-section over which water is exchanged between computational cells. In this study, it was shown that resolving friction and the exchange cross-section to the subgrid scale improved (or at worst equaled) simulated flow patterns compared to simulations in which the friction and exchange cross-section were resolved to the computational cell size. This has implications for future modeling studies. Bathymetric features with length scales smaller than the current bed resolution (<20mx20m) exist both in the Wadden Sea (Dolch & Reise, 2010; Jr & Flemming, 1991), and on intertidal flats in general (Whitehouse et al., 2000). Their impact on flow is currently implicitly captured in the bottom roughness coefficient. As flow velocity is not a simple function of local depth and roughness, this is not entirely adequate (as illustrated in Volp (2017)). When bathymetric data of a higher resolution is available, subgrid modeling technique can offer a way to explicitly resolve the impact of higher-resolution bathymetric features on flow, without having to refine the computational grid to computationally unfeasible resolutions. It follows that subgrid modeling technique offers opportunities for computationally efficient morphological simulations with flow on the coarse grid and a bed level subgrid (as further discussed in Volp (2017)).

8

Conclusions & Recommendations

The main goal of this study is to systematically assess the detailed horizontal flow patterns on the scale of an intertidal flat and how they are influenced by wind forcing. It is important to assess these flow patterns as they are important to ecology and the morphological evolution of intertidal flats, which can affect ecosystem services such as coastal protection. The research question is:

'What determines the horizontal flow patterns on intertidal flats in the Western Dutch Wadden Sea, and how does wind influence these flow patterns?

In short, the horizontal flow patterns on intertidal flats follow from the water level gradient between surrounding channels and are influenced by the intertidal flat geometry (i.e. size, bed elevation, and degree to which the intertidal flat is intersected by tidal channels), hydraulic boundary condition (i.e. phase of the spring-neap tidal cycle, asymmetry of the tidal wave), and wind forcing (which can completely alter hydrodynamics at several scales).

Addressing the adequacy of subgrid modeling technique to capture flow patterns on intertidal flats is an important part of this study. Its adequacy depends on the intended purpose of the model and feasible grid resolutions. In the estuarine setting of the western Dutch Wadden Sea and estuaries with similar hydraulic boundary conditions, subgrid modeling technique offers an increase in how well the flow pattern is represented compared to simulations using interpolated bathymetry and the same computational grid resolution. It does not serve as a replacement for higher-resolution models. The automatic wetting-and-drying allows for the study of shallow flows where measurements and hydrodynamic models that require a wetting-and-drying algorithm face difficulties.

In absence of wind forcing, the flow patterns on intertidal flats follow from the water level gradients between the channels surrounding the intertidal flat. The magnitude of water level gradients, and therefore of flow velocities, depends on intertidal flat geometry (i.e. size, bed elevation, and degree to which the intertidal flat is intersected by tidal channels) and the phase of the spring-neap tidal cycle. Intertidal flats cyclically inundate during flood and dry during ebb. This leads to a maximum of four peaks in absolute velocity per tidal cycle, of which two follow from physics on the scale of an intertidal flat and two from the basin-scale tide. Flow velocities on the upper intertidal flat are smaller than on the lower intertidal flat due to the larger importance of friction as a consequence of smaller water depth. There is a phase difference between the High Water slack tide on the intertidal flat and in the surrounding tidal channels. High intertidal flat elevation and the absence of intersecting tidal channels inhibit the exchange of water between tidal channels surrounding the intertidal flat. A significant water level difference can build up. Once water levels exceed the intertidal flat, a water level gradient is created and flow follows the gradient. The magnitude of the water level gradient follows from the interplay between intertidal flat size and the magnitude of water level differences. Low intertidal flat elevation and the presence of intersecting tidal channels enable the exchange of water between the tidal channels surrounding the intertidal flat. No significant water level gradient builds up, and water flow follows the basin-scale water level gradient. Tidal asymmetry seems to increase from relatively symmetrical in time during neap tide to asymmetrical

during spring tide. The phase of the spring-neap tidal cycle also affects the rising and falling rate of the tide. This affects the magnitude of water level gradients, thereby impacting flow velocities. The phase of the spring-neap tidal cycle does not seem to affect the flow direction at a given phase of the regular tidal cycle.

Unidirectional wind forcing of 15 m/s both from the east and from the west significantly alters the flow pattern on several scales. On the basin scale, set-up and set-down occur (dependent on wind direction), changing the inundation and drying patterns on intertidal flats. On the scale of an intertidal flat, wind shear accelerates flow in the wind direction and decelerates flow opposite the wind direction, resulting in a substantial shift in how water enters and leaves the intertidal flat. Furthermore, wind has a depth-dependent impact on flow patterns at the intertidal flat. The magnitude and direction of flow on the upper intertidal flat, where water depths are smaller, are completely altered. The magnitude and direction of flow on the lower intertidal flat, where depths are slightly larger, are altered but not to the same degree as on the upper intertidal flat. On the scale of a gully, wind forcing substantially alters the flow pattern if the direction of the wind event aligns with the gully axis, but not if the wind event is perpendicular to the gully axis. The combination of basin-scale water level set-up or set-down with wind shear on the scale of an intertidal flat causes spatial variability in exposure times. As only two unidirectional wind events were studied, further study into the effect of varying wind forcing on the flow patterns on intertidal flats is required.

This study has contributed to the knowledge on horizontal flow patterns on intertidal flats, with the aim to further the understanding of mechanisms steering their morphological evolution. This understanding benefits studies into ecology, navigational maintenance, flood protection, and the ability of intertidal flats to keep up with sea level rise. While the flow pattern plays a significant role, it is not solely responsible for morphological change. Waves, freshwater influx, biological processes, North Sea sediment concentration, and dredging activities also affect the Wadden Sea morphology. Moving forward, continued research into the drivers of the morphological change of intertidal flats will be crucial for the informed management of ecologically valuable estuarine areas like the Wadden Sea.

8.1. Recommendations

While this study has contributed to the knowledge on flow patterns on intertidal flats, knowledge gaps remain both in the knowledge on the Wadden Sea system and in hydrodynamic models. With a view to the practice of Wadden Sea management and maintenance, hydrodynamic models serve as a means to gain system knowledge instead of an end in itself. Recommendations are made to fill gaps in Wadden Sea system knowledge, potentially through advancing the knowledge on (subgrid-based) hydrodynamic models.

Tidal asymmetry over the spring-neap tidal cycle
Indications were found that the tidal wave becomes increasingly asymmetric in time from neap tide to spring tide. Because of the implications for sediment dynamics and therefore the morphological evolution of the system, it is important to assess whether this is actually the case.

Directionally varying wind
In addition to the flow patterns due to unidirectional wind events, the effect of directionally varying wind (i.e. a regular wind climate) on the flow patterns on intertidal flats should be studied. This is relevant for ecology and morphology.

Effect of the over-consolidation process on predictive capacity of morphological models
The over-consolidation process increases shear strength against erosion. No instances were found where this non-linearity is accounted for in morphological models. Its effect on the predictive capacity of morphological models should be studied.

Additional velocity and water level measurements on intertidal flats
Only a limited amount of velocity and water level measurements are available on intertidal flats. To advance the knowledge on the intertidal zone, more measurements are needed. These should be analyzed by themselves and serve for validation purposes of hydrodynamic models. Preferably, at least two campaigns should be carried out, one during minimal wind conditions and one during notable wind forcing. The Kornwerderzand intertidal flat is a good candidate. The highest bed elevations are inundated for roughly half the tidal cycle. Shorter submergence would not provide valuable data considering a minimum water depth is required for adequate measurements. Two measurement frames on the lower intertidal flat and two measurement frames on the upper intertidal flat and a 10-20 minute measuring frequency should suffice for model calibration purposes. Exposure time maps in this report could help inform placement.

Application of automatic wetting & drying
The automatic wetting & drying shows promise. At current, automatic wetting & drying is the only means to study the following relevant Wadden Sea topics without the drawback of a wetting & drying algorithm: dispersal of plastic particles and how these deposit in the intertidal zone, velocity pulses, and exposure times for ecological maps. As results indicate that rigid lid approaches do not suffice to estimate exposure times, model simulations are required for ecological maps instead. It is recommended to consider using subgrid modeling technique for its automatic wetting & drying when studying these topics.

Subgrid-based morphological modeling
Morphological simulations are computationally demanding. Gains in computational efficiency therefore add up in the long term. Subgrid modeling technique offers opportunities for computationally efficient morphological simulations. It is recommended to perform a case study to compare the accuracy and computational efficiency of an existing standard-practice (Delft3D) Wadden Sea morphological model to subgrid-based morphological model schematizations with varying grid sizes regarding accuracy and computational efficiency.

Improvements to subgrid-based model accuracy
While automatic wetting & drying and the subgrid are benefits, the main drawback of applying the present subgrid-based hydrodynamic model in its current state is accuracy. The model accuracy after a time-limited calibration is an order of magnitude (decimeters) lower than standard-practice Wadden Sea hydrodynamic models Delft3D and GETM (centimeters). For many research and maintenance applications, the current model accuracy does not suffice. The cause of numerical diffusion should be investigated. If numerical diffusion can be reduced, it should be possible to increase model accuracy to the order of centimeters with a more extensive calibration.

References

Baptist, M. J., van der Wal, J. T., de Groot, A. V., & Ysebaert, T. J. W. (2016). *Ecotopenkaart waddenzee volgens de zes.1 typologie*.

Bosboom, J., & Stive, M. J. F. (2021). Coastal dynamics.

Candy, A. S. (2017). An implicit wetting and drying approach for non-hydrostatic baroclinic flows in high aspect ratio domains. *Advances in Water Resources*, *102*, 188–205.

Casulli, V. (2009). A high-resolution wetting and drying algorithm for free-surface hydrodynamics. *International Journal for Numerical Mehtods in Fluids*, *60*(4), 391–408.

Casulli, V., & Stelling, G. S. (2011). Semi-implicit subgrid modelling of three-dimensional free-surface flows. *International Journal for Numerical Methods in Fluids*, *67*(4), 441–449.

Coen, L. D., Brumbaugh, R. D., Bushek, D., Grizzle, R., Luckenbach, M. W., Posey, M. H., Powers, S. P., & Tolley, S. G. (2007). Ecosystem services related to oyster restoration. *Marine Ecology Progress Series*, *341*, 303–307.

Colosimo, I., de Vet, P. L. M., van Maren, D. S., Reniers, A. J. H. M., Winterwerp, J. C., & van Prooijen, B. C. (2020). The impact of wind on flow and sediment transport over intertidal flats. *Journal of Marine Science and Engineering*, *8*(11), 910.

Colosimo, I., van Maren, D. S., de Vet, P. L. M., Winterwerp, J. C., & van Prooijen, B. C. (2023). Winds of opportunity: The effects of wind on intertidal flat accretion. *Geomorphology*, *439*, 108840.

Common Wadden Sea Secretariat. (2016). *Report on the state of conservation of the world heritage property "the wadden sea (n1314)"*.

de Vet, P. L. M., van Prooijen, B. C., Colosimo, I., Steiner, N., Ysebaert, T., Herman, P. M. J., & Wang, Z. B. (2020). Variations in storm-induced bed level dynamics across intertidal flats. *Scientific Reports*, *10*, 12877.

de Vet, P. L. M., van Prooijen, B. C., Schrijvershof, R. A., van der Werf, J. J., Ysebaert, T., Schrijver, M. C., & Wang, Z. B. (2018). The importance of combined tidal and meteorological forces for the flow and sediment transport on intertidal shoals. *Journal of Geophysical Research: Earth Surface*, *123*, 2464–2480.

Dolch, T., & Reise, K. (2010). Long-term displacement of intertidal seagrass and mussel beds by expanding large sandy bedforms in the northern wadden sea. *Journal of Sea Research*, *63*(2), 93–101.

Duran-Matute, M., Gerkema, T., de Boer, G. J., Nauw, J. J., & Gräwe, U. (2014). Residual circulation and freshwater transport in the dutch wadden sea: A numerical modelling study. *Ocean Science*, *10*, 611–632.

Duran-Matute, M., Gerkema, T., & Sassi, M. G. (2016). Quantifying the residual volume transport through a multiple-inlet system in response to wind forcing: The case of the western dutch wadden sea. *Journal of Geophysical Research: Oceans*, *121*, 8888–8903.

European Union. (2024). *Copernicus sentinel-2 imagery*. https://www.copernicus.eu/en/media/image-day-gallery/northern-netherlands

Friedrichs, C. T. (2011). Tidal flat morphodyanmics: A synthesis. *Treatise on Estuarine and Coastal Science*, *3*.

Funke, S. W., Pain, C. C., Kramer, S. C., & Piggott, M. D. (2011). A wetting and drying algorithm with a combined pressure/free-surface formulation for non-hydrostatic models. *Advances in Water Resources*, *34*(11), 1483–1495.

Gerkema, T., & Duran-Matute, M. (2017). Interannual variability of mean sea level and its sensitivity to wind climate in an inter-tidal basin. *Earth System Dynamics*, *8*(4), 1223–1235.

Google. (n.d.). https://www.google.cn/maps/vt?lyrs=s@189&gl=cn

Gouwenaar. (n.d.). *Zonsondergang waddenzee*. https://commons.wikimedia.org/wiki/File:20210908_zonsondergang4_Waddenzee.jpg)

Grasmeijer, B., Jaksic, L., & Vroom, J. (2022). *Verkenning morfologische ontwikkeling westelijke waddenzee*. Deltares.

Gräwe, U., Flöser, G., Gerkema, T., Duran-Matute, M., Badewien, T. H., Schulz, E., & Burchard, H. (2016). A numerical model for the entire wadden sea: Skill assessment and analysis of hydrodynamics. *Journal of Geophysical Research: Oceans*, *121*(7).

Guo, L., Wang, Z. B., Townend, I., & He, Q. (2019). Quantification of tidal asymmetry and its nonstationary variations. *Journal of Geophysical Research: Oceans*, *124*(1), 773–787.

Gupta, H. V., Kling, H., Yilmaz, K. K., & Martinez, G. F. (2009). Decomposition of the mean squared error and nse performance criteria: Implications for improving hydrological modelling. *Journal of Hydrology*, *377*(1-2), 80–91.

Heip, C. H. R., Goosen, N. K., Herman, P. M. J., adn J. J. Middelburg, J. K., & Soetaert, K. (1995). Production and consumption of biological particles in temperate tidal estuaries. *Oceanography and Marine Biology Annual Reviews*, *33*, 1–150.

Herman, P. M. J., van Kessel, T., Vroom, J., Dankers, P., Cleveringa, J., de Vries, B., & Villars, N. (2018). *Mud dynamics in the wadden sea; towards a conceptual model*. Deltares.

Hope, J. A., Paterson, D. M., & Thrush, S. F. (2020). The role of microphytobenthos in soft-sediment ecological networks and their contribution to the delivery of multiple ecosystem services. *Journal of Ecology*, *108*(3), 815–830.

Huismans, Y., van der Spek, A., Lodder, Q., Zijlstra, R., Elias, E., & Wang, Z. B. (2022). Development of intertidal flats in the dutch wadden sea in response to a rising sea level: Spatial differentiation and sensitivity to the rate of sea level rise. *Ocean & Coastal Management*, *216*.

Hunt, S., Bryan, K. R., & Mullarney, J. C. (2015). The influence of wind and waves on the existence of stable intertidal morphology in meso-tidal estuaries. *Geomorphology*, *228*, 158–174.

Jordan, C., Visscher, J., & Schlurmann, T. (2021). Projected responses of tidal dynamics in the north sea to sea-level rise and morphological changes in the wadden sea. *Frontiers in Marine Science*, *8*.

Jr, R. A. D., & Flemming, B. W. (1991). Time-series study of mesoscale tidal bedforms, martens plate, wadden sea, germany. *Sedimentary Geology*.

Kennedy, A. B., Wirasaet, D., Begmohammadi, A., Sherman, T., Bolster, D., & Dietrich, J. C. (2019). Subgrid theory for storm surge modeling. *Ocean Modelling*, *144*, 101491.

Le, H. A., Lambrechts, J., Ortleb, S., Gratiot, N., Deleersnijder, E., & Soares-Fražao, S. (2020). An implicit wetting–drying algorithm for the discontinuous galerkin method: Application to the tonle sap, mekong river basin. *Environmental Fluid Mechanics*, *20*(4), 923–951.

Le Hir, P., Roberts, W., Cazaillet, O., Christie, M., Bassoullet, P., & Bacher, C. (2000). Characterization of intertidal flat hydrodynamics. *Continental Shelf Research*, *20*(12-13), 1433–1459.

Lodder, Q., Huismans, Y., Elias, E., de Looff, H., & Wang, Z. B. (2022). Future sediment exchange between the dutch wadden sea and north sea coast - insights based on asmita modelling. *Ocean & Coastal Management*, *219*, 106067.

MacWilliams, M. L., Bever, A. J., & Foresman, E. (2016). 3-d simulations of the san francisco estuary with subgrid bathymetry to explore long-term trends in salinity distribution and fish abundance. *San Francisco Estuary and Watershed Science*, *14*(2).

Medeiros, S. C., & Hagen, S. C. (2013). Review of wetting and drying algorithms for numerical tidal flow models. *International Journal for Numerical Methods in Fluids*, *71*.

Nelen & Schuurmans. (n.d.-a). *Subgrid method*. https://docs.3di.live/h_subgrid.html

Nelen & Schuurmans. (n.d.-b). *Wind effects*. https://docs.3di.live/h_wind.html

Nowacki, D. J., & Ogston, A. S. (2013). Water and sediment transport of channel-flat systems in a mesotidal mudflat: Willapa bay, washington. *Continental Shelf Research*, *60, Supplement*, S111–S124.

Oost, A. P. (1995). *Dynamics and sedimentary development of the dutch wadden sea with emphasis on the frisian inlet, a study of barrier islands, ebb-tidal deltas, inlets and drainage basins*.

Oost, A. P., van Buren, R., & Kieftenburg, A. (2017). *Overview of the hydromorphology of ebb-tidal deltas of the trilateral wadden sea*. Deltares.

Paterson, D. M., Aspden, R. J., & Black, K. S. (2009). Intertidal flats: Ecosystem functioning of soft sediment systems. *Coastal wetlands: an integrated ecosystem approach*, 317–338.

Piersma, T., de Goeij, P., & Tulp, I. (1993). An evaluation of intertidal feeding habitats from a shorebird perspective: Towards relevant comparisons between temperate and tropical mudflats. *Netherlands Journal of Sea Research*, *31*(4), 503–512.

Pritchard, D., Hogg, A. J., & Roberts, W. (2002). Morphological modelling of intertidal mudflats: The role of cross-shore tidal currents. *Continental Shelf Research*, *22*(11-13), 1887–1895.

Reise, K., Baptist, M., Burbridge, P., Dankers, N., Fischer, L., Flemming, B., Oost, A. P., & Smit, C. (2010). The wadden sea – a universally outstanding tidal wetland [Common Wadden Sea Secretariat]. *Wadden Sea Ecosystem No. 29*, 7–24.

Rijkswaterstaat. (2023). *Vaklodingen bathymetry request page* [Dataset]. https://www.rijkswaterstaat.nl/formulieren/contactformulier-servicedesk-data

Schulz, K., & Gerkema, T. (2018). An inversion of the estuarine circulation by sluice water discharge and its impact on suspended sediment transport. *Estuarine, Coastal and Shelf Science*, *200*, 31–40.

Sehili, A., Lang, G., & Lippert, C. (2014). High-resolution subgrid models: Background, grid generation, and implementation. *Ocean Dynamics*, *64*, 519–535.

Smits, B., Vroom, J., van Weerdenburg, R., & Alonso, A. C. (2022). *Morfologie en onderhoud vaargeul boontjes: Systeembegrip en scenario's*. Deltares.

Stelling, G. S. (2012). Quadtree flood simulations with sub-grid digital elevation models. *Proceedings of the Institution of Civil Engineers - Water Management*, *165*(10), 567–580.

UNESCO World Heritage Centre. (n.d.). *Wadden sea*. Retrieved May 25, 2023, from https://whc.unesco.org/en/list/1314

van der Werf, J., Antolínez, J. A. A., Brakenhoff, L., Gawehn, M., den Heijer, K., de Looff, H., van Maarsseveen, M., Meijer-Holzhauer, H., Mol, J.-W., Pearson, S., van Prooijen, B. C., Santinelli, G., G., C. S., Tissier, M., Tonnon, P. K., de Vet, L., Vermaas, T., Wilmink, R., & de Wit, F. (2019). *Datareport kustgenese 2.0 measurements*. Rijkswaterstaat.

van Goor, M. A., Zitman, T. J., Wang, Z. B., & Stive, M. J. F. (2003). Impact of sea-level rise on the morphological equilibrium state of tidal inlets. *Marine Geology*, *202*(3-4), 211–227.

van Prooijen, B. C., Tissier, M. F. S., de Wit, F. P., Pearson, S. G., Brakenhoff, L. B., van Maarseveen, M. C. G., van der Vegt, M., Mol, J.-W., Kok, F., Holzhauer, H., van der Werf, J. J., Vermaas, T., Gawehn, M., Grasmeijer, B., Elias, E. P. L., Tonnon, P. K., Santinelli, G., Antolínez, J. A. A., de Vet, P. L. M., … de Looff, H. (2020). Measurements of hydrodynamics, sediment, morphology and benthos on ameland ebb-tidal delta and lower shoreface. *Earth System Science Data*, *12*(4), 2775–2786.

van Straaten, L. M. J. U. (1951). Longitudinal ripple marks in mud and sand. *Journal of Sedimentary Research*, *21*(1), 47–54.

van Weerdenburg, R., Pearson, S., van Prooijen, B., Laan, S., Elias, E., Tonnon, P. K., & Wang, Z. B. (2021). Field measurements and numerical modelling of wind-driven exchange flows in a tidal inlet system in the dutch wadden sea. *Ocean & Coastal Management*, *215*.

Volp, N. D. (2017). *Subgrid is dancing with sediment: A full subgrid approach for morphodynamic modelling* [Doctoral dissertation, Delft University of Technology].

Volp, N. D., van Prooijen, B. C., & Stelling, G. S. (2013). A finite volume approach for shallow water flow accounting for high-resolution bathymetry and roughness data. *Water Resources Research*, *49*, 4126–4135.

Vroom, J., van Weerdenburg, R., Smits, B. P., & Herman, P. (2020). *Modellering slibdynamiek voor de waddenzee*. Deltares.

Wang, Z. B., Hoekstra, P., Burchard, H., Ridderinkhof, H., Swart, H. D., & Stive, M. J. F. (2012). The morphodynamics of the wadden sea and its barrier island system. *Ocean & Coastal Management*, *68*, 39–57.

Whitehouse, R. J. S., Bassoullet, P., Dyer, K. R., Mitchener, H. J., & Roberts, W. (2000). The influence of bedforms on flow and sediment transport over intertidal mudflats. *Continental Shelf Research*, *20*(10-11), 1099–1124.

Wu, G., Shi, F., Kirby, J. T., Mieras, R., Liang, B., Li, H., & Shi, J. (2016). A pre-storage, subgrid model for simulating flooding and draining processes in salt marshes. *Coastal Engineering*, *108*, 65–78.

Yang, S. L., Li, H., Ysebaert, T., Bouma, T. J., Zhang, W. X., Wang, Y. Y., Li, P., Li, M., & Ding, P. X. (2008). Spatial and temporal variations in sediment grain size in tidal wetlands, yangtze delta: On the role of physical and biotic controls. *Estuarine, Coastal and Shelf Science*, *77*(4), 657–671.

Zhang, Q., Gong, Z., Zhang, C., Townend, I., Jin, C., & Li, H. (2016). Velocity and sediment surge: What do we see at times of very shallow water on intertidal mudflats? *Continental Shelf Research*, *113*, 10–20.

Zhu, S., Chen, Y., Yan, W., Xing, F., Li, R., Li, M., Shi, B., & Wang, Y. P. (2022). The hummocky patches and associated sediment dynamics over an accretional intertidal flat. *Frontiers in Earh Science*, *10*, 908351.

Zijl, F., Veenstra, J., & Groenenboom, J. (2018). *The 3d dutch continental shelf model - flexible mesh (3d dcsm-fm). setup and validation. report 1220339-000-zks-0042*. Deltares.

A

Subgrid modeling technique as described in Volp et al. (2013)

The subgrid method as described in Volp et al. (2013) takes into account small-scale variations in bed roughness and velocities by estimating subgrid-scale velocities. This estimate results in a 'friction depth'. Through the friction depth, variations in roughness and velocity at subgrid resolution are taken into account in calculations on the computational grid resolution. The discretization of the part of the momentum equation specific to the subgrid method as described in Volp et al. (2013) is outlined in this appendix.

The momentum balance in the x-direction is given in Equation A.1. In this balance, the inertia, advection of momentum, pressure, and friction forces (respectively) are present. $(uV)_t$ denotes inertia, and $\tilde{F}$ denotes a force normalized with density, which is assumed constant.

$$(uV)_t + \tilde{F}^x_{adv} + \tilde{F}^x_{pres} + \tilde{F}^x_{fric} = 0 \tag{A.1}$$

Especially the spatial discretization of the friction and advection forces are of relevance, as these are specific to this subgrid method. For future reference, the computational grid as in Volp et al. (2013) is given in Figure A.1. The grid is staggered, meaning that water level and momentum domains are offset by half a computational cell.

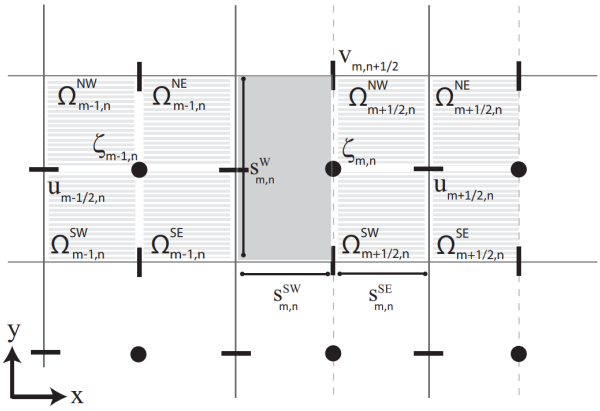

Figure A.1: Computational grid with water level and velocity points indicated. A water level domain (left) and momentum domain (right) are highlighted. Bed level subgrid not shown. Volp et al. (2013).

Momentum domains are covered by four quarter domains. Each quarter domain provides a contribution to the total bottom friction in a momentum domain. The bottom friction in a momentum domain is taken as the sum of the four quarter domain bottom friction contributions. The quarter domain bottom friction is calculated by establishing a relationship between velocities on the subgrid scale and the velocity on the scale of the quarter domain by using the following assumptions:

- a uniform flow direction within a quarter domain is assumed;
- a uniform friction slope within a quarter domain is assumed;
- the quarter domain scale velocity is defined as the volume average of the subgrid velocities.

By assuming a uniform flow direction, internal circulations, convergence, and divergence are excluded within the quarter domain. The formulation for a uniform friction slope is given in Equation A.2.

$$S = \frac{c_f u_p^2}{gH} = uniform \tag{A.2}$$

with:

S	friction slope	[-]
c_f	bottom friction	[-]
u_p	subgrid-scale flow velocity	[m/s]
H	water depth	[m]

The friction slope is the ratio between the bottom friction term and the water level gradient. In the case of steady flow, the friction slope equals the water level gradient and the bed slope. As such, the assumption has a physical basis. In essence, it is an assumption about the flow structure based on the relative importance of friction. When friction is dominant, this assumption plays a large role in converting subgrid-scale velocities to the velocity on the quarter momentum domain scale. However, when the relative importance of friction decreases, the influence of this assumption in deciding the computational cell velocity decreases as well. In the limit, for marginal importance of friction, the system of equations that describes the water movement reduces to the same system of equations used in non-subgrid models. Thus, in such a case the assumption of a uniform friction slope is as good as the assumption of a uniform velocity within a computational cell.

The uniform friction slope assumption again plays a role in calculating discharges. In the subgrid method as described in Volp et al. (2013), the discharge over the face of a water level domain is known (Figure A.1). Discharges over the faces of a momentum domain are not known and are therefore constructed from discharges over the faces of water level domains. The distribution of the discharge is constructed in such a way that continuity is guaranteed, and a uniform friction slope is assumed. This results in discharges over the faces of a momentum domain which are based on water depth and friction. By applying a uniform friction slope, the structure of the flow is assumed. The assumption plays a large role in constructing discharges over the face of a momentum domain when friction is dominant but plays a smaller role when the relative importance of friction decreases.

The wind-induced shear stress term in the x-direction in a quarter momentum domain is defined as:

$$\tilde{F}^x_{fric;wind} = \rho_a \iint C_d \, |\vec{u}_w - \vec{\chi}\vec{u}| (u^x_w - \chi^x u^x) \, d\Omega \tag{A.3}$$

using:

$$\chi^x = \max\left(1, \frac{u^x_w u^x}{gH}\right); \qquad \vec{\chi} = \begin{bmatrix} \chi^x \\ \chi^y \end{bmatrix} \tag{A.4}$$

with:

ρ_a	air density	[kg/m^3]
χ	correction factor	[-]
C_d	wind drag coefficient	[-]
u_w	wind velocity	[m/s]
Ω	quarter domain surface area	[m^2]

Wind has a large effect on thin water layers. To prevent wind from accelerating thin water layers to unphysical velocities, creating numerical instabilities, extra momentum losses are introduced through the correction factor χ. Only for small water depths and a large product of wind and water velocities is this factor larger than 1. In these cases, the wind shear stress is reduced. It should be noted that the formulation of the factor χ has not been validated. This is due to the difficulty of setting up an adequate validation, which would require measurements in shallow water and on wet-dry interfaces. While not validated, this factor is mathematically grounded in physics (Nelen & Schuurmans, n.d.-b). The denominator of this factor is the square of the critical velocity ($\sqrt{gH}$), which is the maximum velocity at which waves propagate linearly.

B

Bathymetric data processing

A description is given in this appendix of the operations performed to process bathymetric data. The bed level of the Dutch Wadden Sea and Ems-Dollard is measured in cycles of six years, with a single tidal basin being measured per year. This dataset is called the Vaklodingen dataset (Rijkswaterstaat, 2023). To schematize the model bed in the Wadden Sea and Ems-Dollard, the most recent available years of 2017 to 2022 were used. The dataset has a 20mx20m resolution. The resulting Digital Elevation Map (DEM) misses some data. Some single pixels were missing, and some areas of pixels were missing (Figure B.1, Figure B.2). Single pixels were supplemented using linear interpolation. Larger areas of missing pixels were supplemented with an older Vaklodingen dataset from around 1990 as this dataset was readily available. Where this operation introduced unrealistically large bed level gradients, smoothing was applied for a more realistic bathymetric profile. A gully that was not yet present in 1990 was manually added (Figure B.3).

The Wadden Sea/Ems-Dollard DEM was expanded to include part of the North Sea (to be able to use provided boundary conditions). Offshore bathymetric data from the KRW Slib model (Vroom et al., 2020) was used. The exact resolution of this bathymetric dataset varies, as it is expressed in longitude and latitude. Additionally, the data resolution near the coast is larger than further off the coast. The approximate resolution ranges from 200m near the coast to 400m a bit farther from the coast to 800m in the Northwest corner of the domain. The data was interpolated to the 20mx20m resolution of the Wadden Sea/Ems-Dollard DEM. Extrapolation was applied to the edges to align the bed level data with the square computational grid. The resulting Digital Elevation Map is shown in Figure B.4

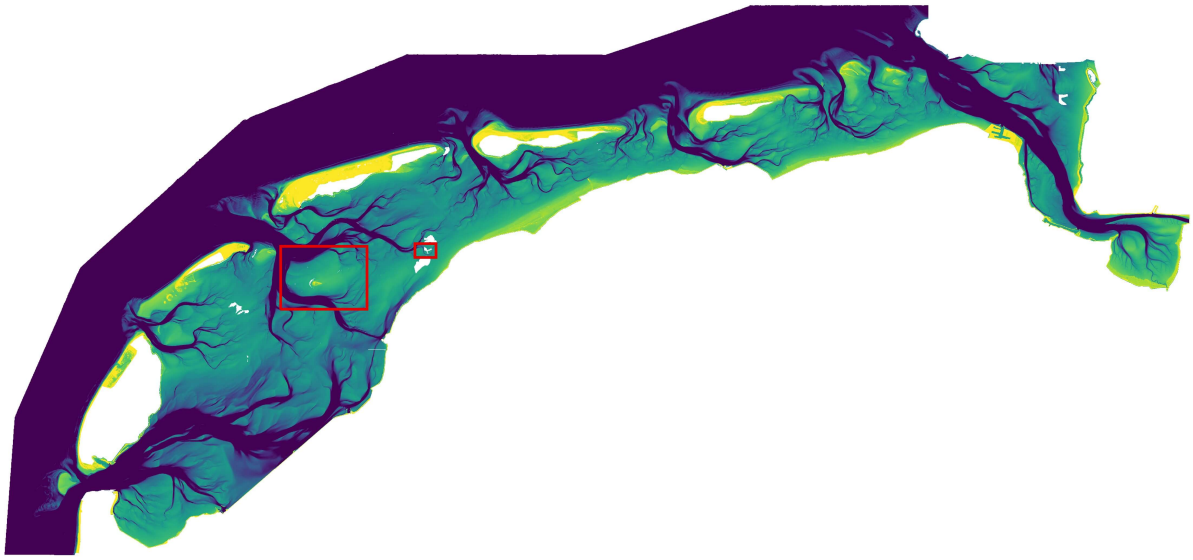

Figure B.1: Vaklodingen dataset 2017-2022. Some larger areas of missing elevation data are visible. Single missing pixels not visible on this scale. Red boxes indicate location of Figure B.2 and Figure B.3.

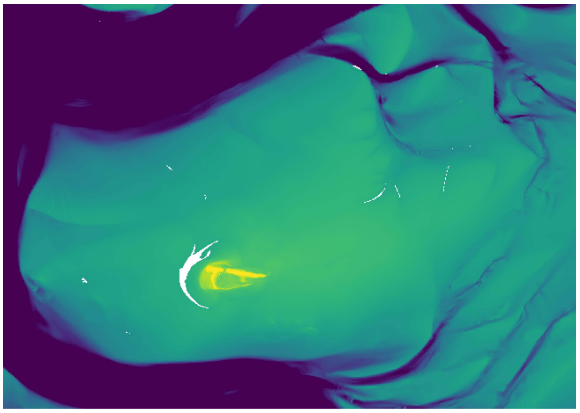

Figure B.2: Zoom of area indicated in Figure B.1. Individual missing data pixels are visible.

Figure B.3: Zoom of area indicated in Figure B.1. In the area of missing data, a channel was manually added.

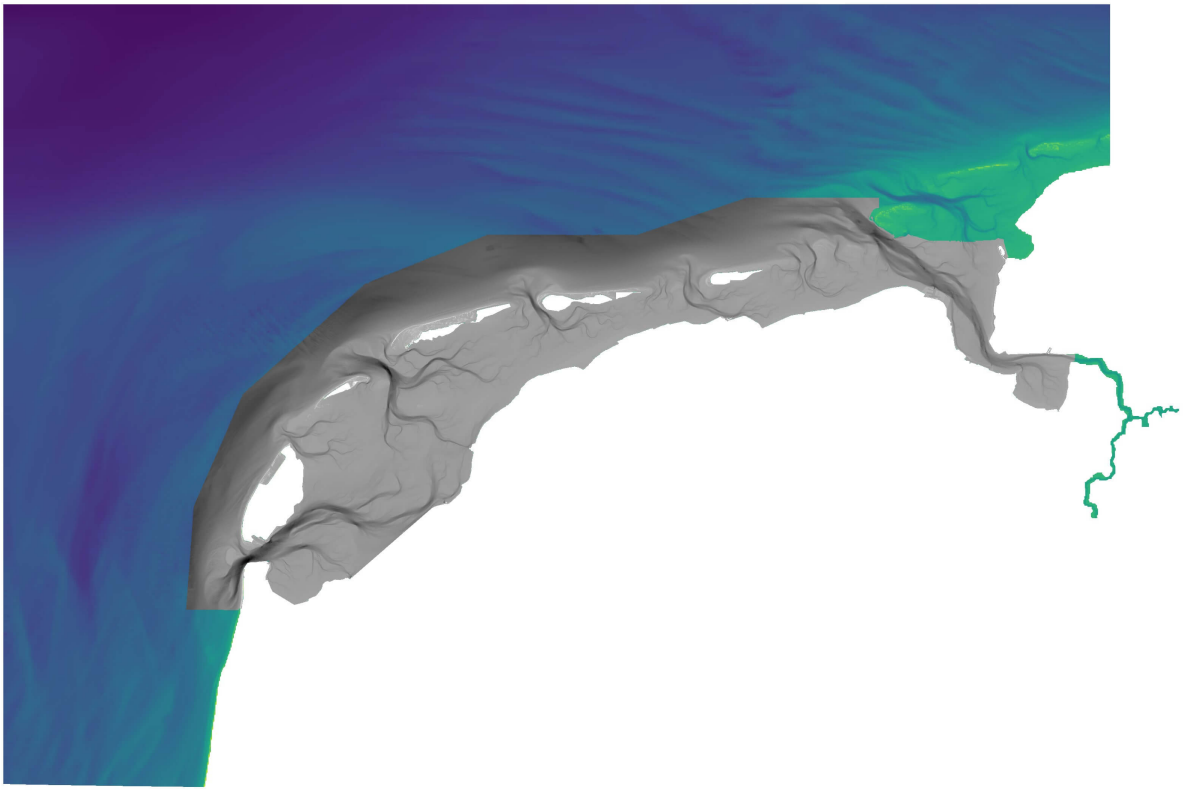

Figure B.4: Digital Elevation Map after expanding it with offshore bathymetric data from the KRW Slib model. Wadden Sea/Ems-Dollard DEM before extension shown in grey to highlight offshore data.

C

Grid resolution

In this appendix, the impact of computational grid resolution on simulated water levels is tested. Several locations are chosen to test the impact of grid resolution: the open sea, a tidal inlet, a tidal channel, the lower intertidal flat, and the upper intertidal flat (Figure C.1). Applied grid resolutions range from 320mx320m to 2560mx2560m. A grid resolution is used in the entire model domain and without further grid refinement.

Figure C.1: Comparison locations of water levels for different calculation grid sizes

At open sea, differences between simulated water levels are minor for all tested grid resolutions (Figure C.2a). In the tidal inlet and tidal channel, there are small differences between the 320mx320m simulation and the other simulations (Figure C.2b, Figure C.2c). At the intertidal flat, water levels of the 2560mx2560m and 1280mx1280m simulations substantially deviate from the 320mx320m simulation (Figure C.2d), Figure C.2e). The 640mx640m simulation has a deviation of the order of centimeters compared to the 320mx320m simulation.

Overall, water levels at open sea are represented well using a grid of 2560mx2560m. Simulated water levels in the Wadden Sea show dependence on the grid resolution. The water levels in the Wadden Sea with a 640mx640m grid resolution are fairly comparable to those in a simulation with a 320mx320m grid resolution. This, along with computational feasibility, are reasons to choose a 640mx640m grid combined with further grid refinement on the intertidal flats that are to be studied.

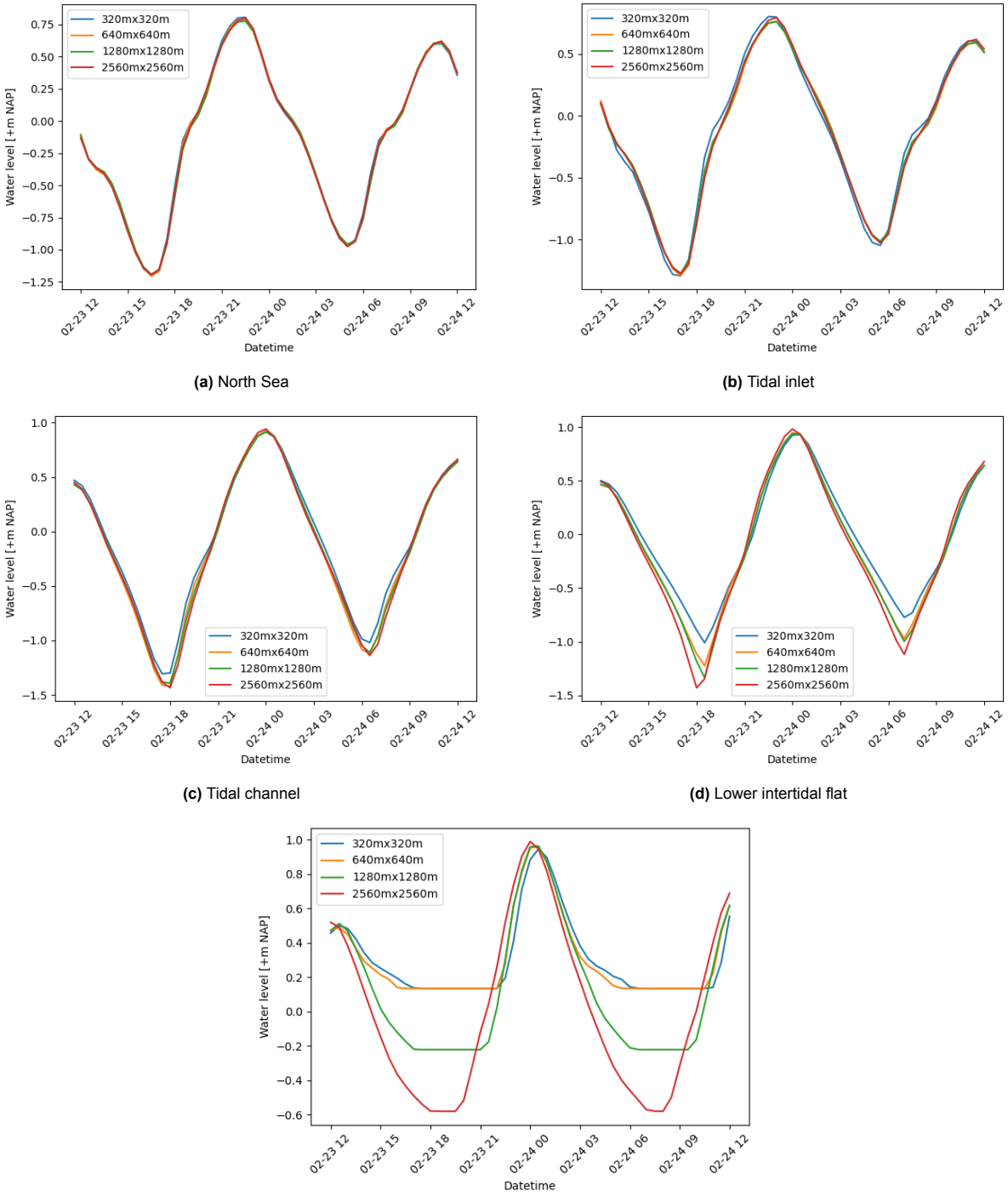

(a) North Sea

(b) Tidal inlet

(c) Tidal channel

(d) Lower intertidal flat

(e) Upper intertidal flat

Figure C.2: Water levels in simulations with different grid sizes at several locations in the Wadden Sea and a location in the North Sea. Exact locations indicated in Figure C.1.

D

Boundary condition

The implementation of the boundary condition is described in this appendix, along with an assessment of the quality of the boundary condition. The boundary condition is implemented using one-dimensional nodes in which a water level timeseries is imposed. A one-dimensional node interacts with the nearest two-dimensional water level node. This is schematized in Figure D.1. Due to the extrapolation applied to the edges of the model, the location of the provided water level boundary conditions does not align exactly with the sides of the model domain (Figure D.1a). This means that no water level is imposed on some computational cells on the edge of the model domain. These cells therefore turn into a closed boundary.

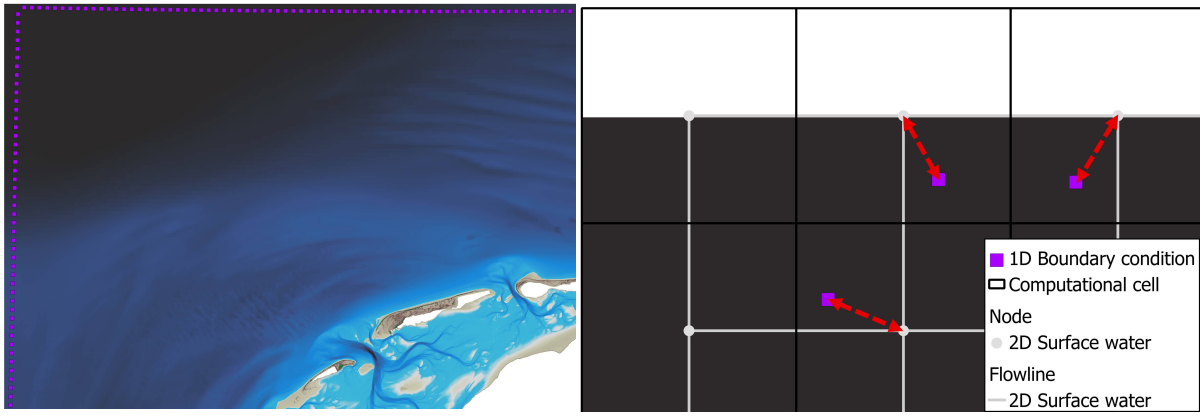

(a) One-dimensional boundary condition nodes in purple. Due to extrapolation of the model domain, these are not exactly on the edges of the model domain.

(b) One-dimensional boundary condition nodes with an indication of how these interact with the nearest two-dimensional computational grid node.

Figure D.1: Boundary condition nodes in the Northwestern corner of the model domain.

D.1. Assessment of boundary condition quality

The data of the water level boundary condition originates from the Dutch Continental Shelf (DCSM) Model (Zijl et al., 2018). It is assessed how well the boundary condition reproduces the conditions that actually occurred. To do so, the measured timeseries at the K14 platform is used. This platform is located relatively close to the model domain boundary. The closest node (index 218) is located roughly 8.2 km away from the K14 platform (Figure D.2). As both locations are in the 'deep water' regime, and due to their close proximity, water levels should be similar at both locations. Water levels across the boundary condition nodes are relatively smooth (Figure D.3a). It is therefore probable that if discrepancies occur between actual conditions at the K14 platform and boundary node 218, there is also a discrepancy between other boundary condition nodes and the actual conditions.

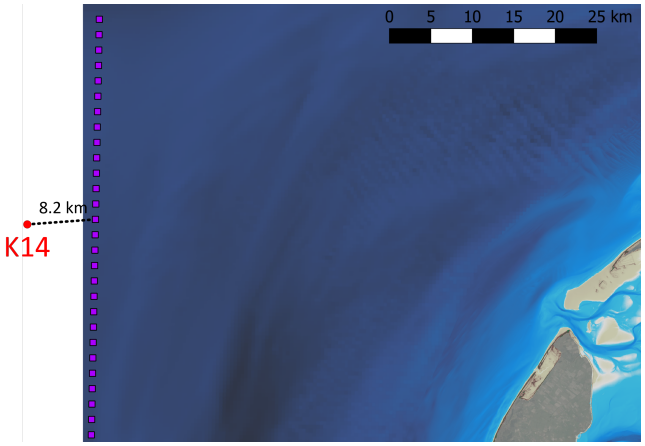

Figure D.2: Location of K14 platform, along with its distance to boundary condition node with index 218.

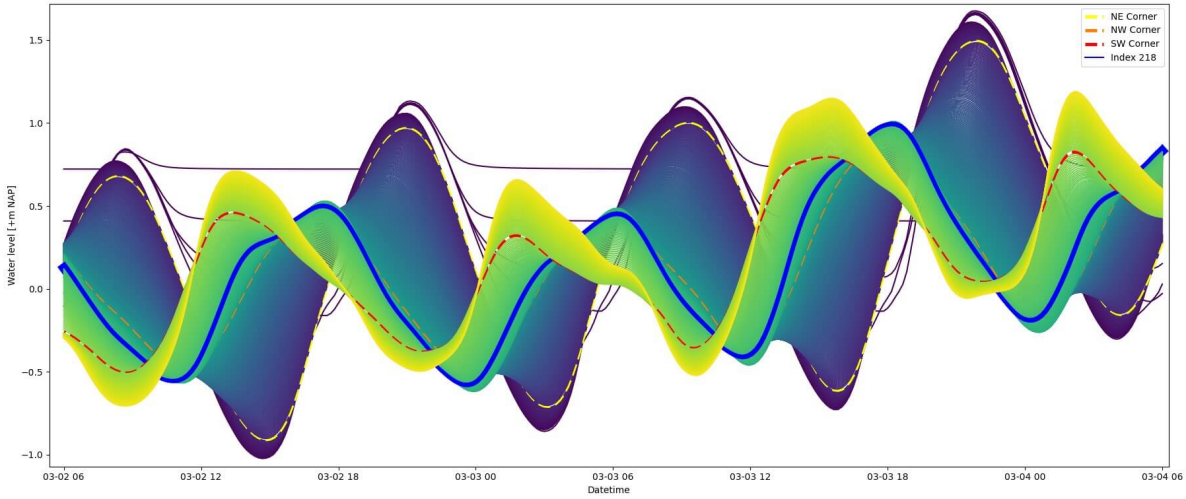

(a) Water level timeseries for all boundary condition nodes. Colors correspond to nodes with the same color in subfigure b. Timeseries corresponding to the corners of the model domain and node 218 are indicated with dashed lines for reference.

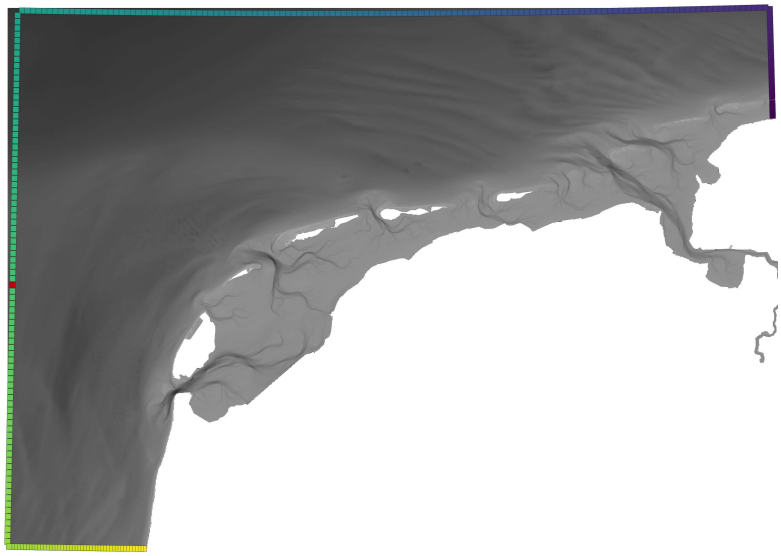

(b) Color-coded boundary condition nodes that correspond to water level timeseries in subfigure a. Node 218 indicated in red.

Figure D.3: (a) Water level timeseries across all boundary condition locations, (b) along with a map indicating the location of nodes.

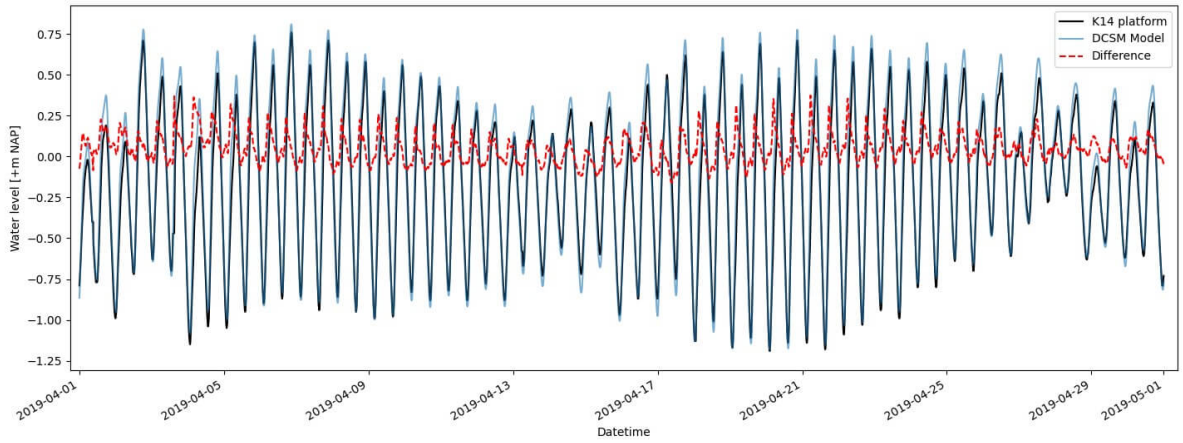

(a) April 1st - May 1st

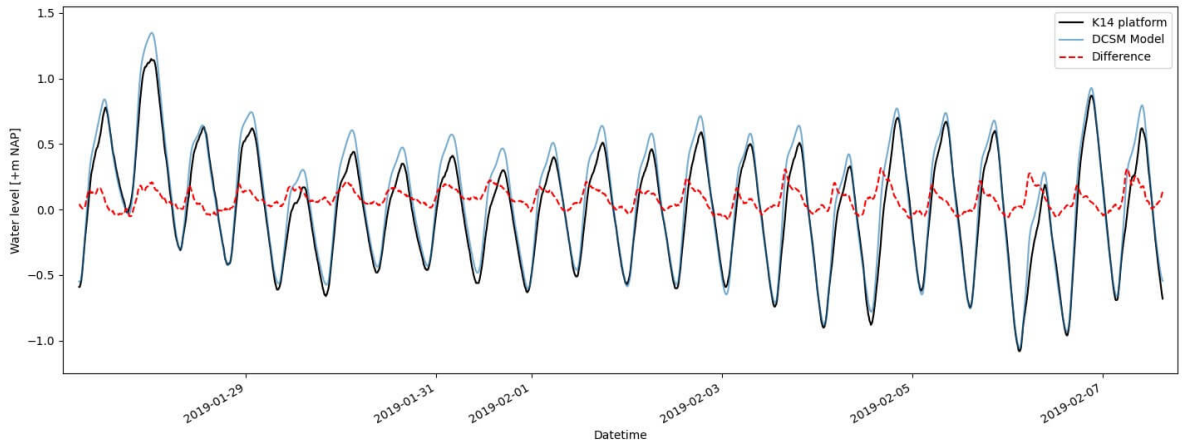

(b) February 27th - March 7th

Figure D.4: Water level timeseries of the measurements at the K14 platform, simulated water levels at boundary condition node with index 218, and the difference between these. Shown during two periods.

A comparison between the water levels measured at the K14 platform and those simulated in the DCSM Model is shown for two periods. To get an idea of the general trend, the entire month of April (Figure D.4a) is shown. For a clearer view of the timeseries, a shorter period in February/March (Figure D.4b) is shown. Over 2019, the mean of the absolute differences between the water level timeseries is 0.11m. During High Waters (HWs), the magnitude of the water level difference increases to approximately 0.2m-0.3m, with maximum water level differences of 0.4m. There seems to be a structural bias in HW levels. These tend to be slightly overestimated. There seems to be no structural bias in Low Water levels. While the overall fit is accurate to the order of a single decimeter, it is important to account for the difference between the boundary condition and actual conditions when analyzing model outcomes.

E

Freshwater discharges

Freshwater discharges for the Ems and measured sluice discharges at Den Oever, Kornwerderzand, and Lauwersoog were provided. The temporal resolution is 10 minutes for the Den Oever and Kornwerderzand sluices, and 15 minutes for the Lauwersoog sluice. Averaged over 2019, discharges at Den Oever and Kornwerderzand were roughly 220 m^3/s at both Den Oever (Figure E.1) and Kornwerderzand (Figure E.2), and about 50 m^3/s at Lauwersoog (Figure E.3). The Ems dataset is incomplete after April 19th. The only comparatively large sluice in the area of interest (Vroom et al., 2020) to be excluded is the Helsdeur sluice at Den Helder. Other large sluices that are not included are those at Spijksterpompen, Noordpolderzijl, and De Drie Delfzijlen, all in the Ems-Dollard estuary. As the Ems dataset was found to be incomplete, discharge from the Ems was also excluded. Aforementioned discharges are located far away from the area of interest. Therefore, the impact of omitting them is relatively small. This is supported by Duran-Matute et al. (2014) getting accurate model results in the Western Dutch Wadden Sea without including the Ems-Dollard in their model domain. Additional sluices with comparatively small discharges (some m^3/s; Vroom et al. (2020)) exist in the area of interest but were not included.

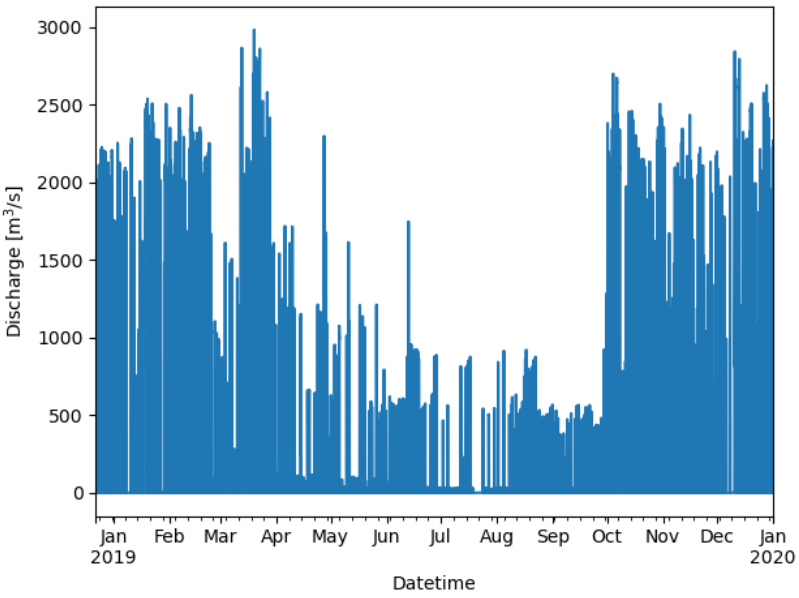

Figure E.1: Sluice discharge over 2019 at the Den Oever sluice.

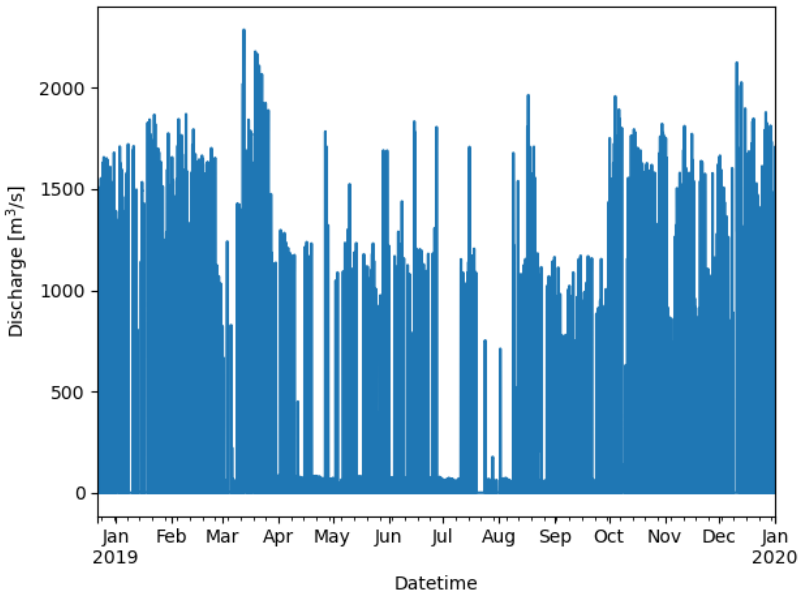

Figure E.2: Sluice discharge over 2019 at the Kornwerderzand sluice.

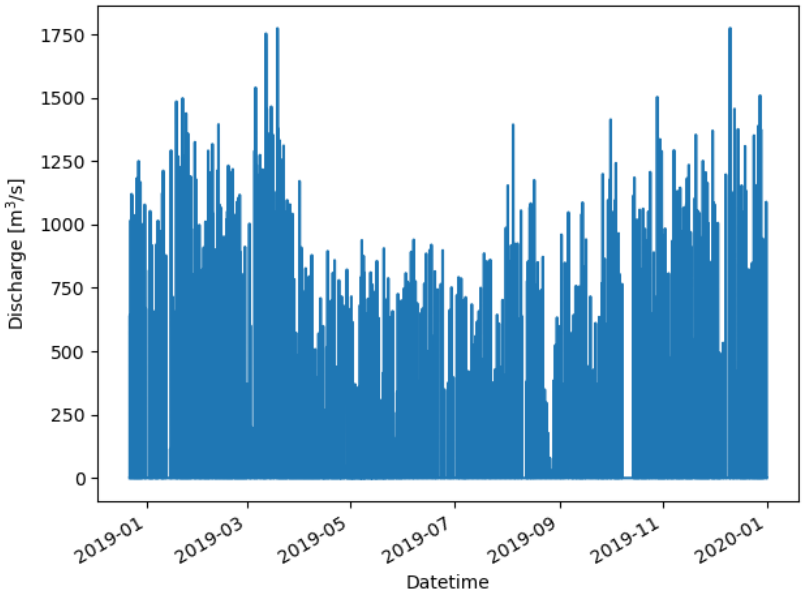

Figure E.3: Sluice discharge over 2019 at the Cleveringsluizen sluice.

F

Calibration

The large-scale water movement of the hydrodynamic model was calibrated. A full description of the calibration procedure is given in this appendix.

In the first calibration stage, water movement without wind forcing was calibrated. The period of February 25th to February 27th was chosen, as the wind forcing of 2.9 m/s is minimal compared to the 2019 mean wind velocity of 7.7 m/s. This means that the wind-induced water level set-up in the boundary condition is minimal. Furthermore, the wind-induced water level set-up in the Wadden Sea is minimal. During this calibration stage, no wind forcing was applied in simulations.

Bottom roughness was iteratively changed until simulated water levels represented actual water levels at measuring stations decently well. Both the Manning and Chézy roughness parameters were tested. Extremely unrealistic Manning values (in some sections n > 0.04) were required to get accurate model results. Therefore, the Chézy roughness parameter was used. Chézy roughness has an inverse relationship with the bottom roughness. A high Chézy roughness value indicates a relatively smooth bed.

The bottom roughness map after this calibration stage is shown in Figure F.1. A relatively high Chézy roughness value of 100 $m^{1/2}/s$ was used in a large part of the model domain. This is because a relatively smooth bed was required to increase the tidal range in the North Sea. Even so, the tidal range in the North Sea is slightly underestimated. This may be the consequence of excessive numerical damping.

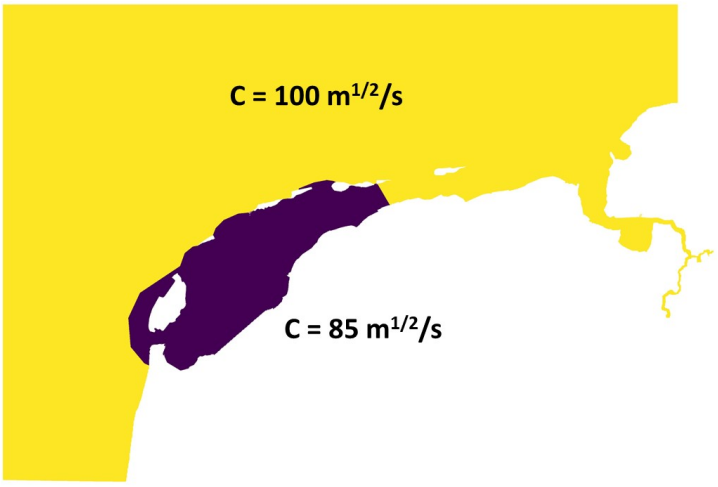

Figure F.1: Overview of bottom roughness throughout the model domain.

Many causes of numerical damping exist. Investigation pointed out that computational cell size (Appendix C) and time step had minimal impact on numerical damping. Probable sources of the excessive numerical damping are the implementation of the boundary condition and the 1st order accuracy of the advection scheme. Further research is required to identify the source of the excessive numerical damping.

The western Dutch Wadden Sea was assigned a Chézy roughness of 85 $m^{1/2}/s$. This was required to align the phase of the simulated tidal wave with the phase of the measured tidal wave at measurement stations in the western Dutch Wadden Sea. A rougher bed in the western Dutch Wadden Sea compared to the rest of the model domain is in line with prior modeling studies (e.g. van Weerdenburg et al. (2021) and Vroom et al. (2020)).

The representativeness of the bottom roughness is tested by comparing it to the modeling efforts of van Weerdenburg et al. (2021) and Duran-Matute et al. (2014), and to the roughness based on length scales of bedforms encountered in the Wadden Sea. It is not possible to make an exact comparison between the different models, as roughness formulations differ. Assumptions are required for a direct comparison. Therefore, the comparison between the different models is indicative. Van Weerdenburg et al. (2021) used a Manning roughness of n = 0.028 $s/m^{1/3}$ in the western Dutch Wadden Sea and n = 0.022 $s/m^{1/3}$ in the rest of the model domain. Duran-Matute et al. (2014) used a uniform bottom roughness length z_0 = 1.7mm. For this indicative comparison, water depths of <10m in the Wadden Sea and hydraulically rough flow are assumed. Using equations E.1, E.2, and E.3, the Chézy, Manning, and bottom roughness length values are converted to the Nikuradse roughness length (Table F.1).

$$C = \frac{1}{n} H^{1/6} \tag{F.1}$$

with:

C Chézy coefficient [$m^{1/2}/s$]
n Manning coefficient [$s/m^{1/3}$]

$$C = 18log(\frac{12H}{k_s}) \tag{F.2}$$

with:

k_s Nikuradse roughness length [m]

$$k_s = 30z_0 \tag{F.3}$$

with:

z_0 bottom roughness length [m]

Table F.1: Indicative values for Nikuradse roughness lengths in the western and eastern Dutch Wadden Sea in three different models.

Model	$\mathbf{k}_{wadden,west}$	$\mathbf{k}_{wadden,east}$
Present study	<2.3 mm	<0.3 mm
van Weerdenburg et al. (2021)	<146 mm	<24 mm
Duran-Matute et al. (2014)	51 mm	51 mm

The Nikuradse roughness length in the present model differs by one to two orders of magnitude compared to the modeling efforts of van Weerdenburg et al. (2021) and Duran-Matute et al. (2014). Differences are especially large in the eastern Dutch Wadden Sea. Length scales of bedforms encountered in the Wadden Sea are roughly a centimeter (Oost, 1995) and half a centimeter (van Straaten, 1951). These give a slight underestimation of the Nikuradse roughness, as the total bed roughness depends on form drag due to bedforms, sediment grain size, and sediment transport near the bed. Compared to the roughness length of measured bedforms, modeled roughness lengths in the present model are off by an order of magnitude. Though the comparison of Nikuradse roughness between different models and with encountered bedforms faces some difficulties, results indicate that the present model underestimates the actual bottom roughness.

Timeseries of resulting water levels are shown at six of the measuring stations and are compared to the actual water level (Figure F.2). In the North Sea, the tidal range is underestimated. This is visible in the Terschelling Noordzee plot. The measuring stations at Den Helder and in the barrier island harbors are relatively close to the North Sea, where the tidal range is underestimated. Therefore, the tidal range in the water level timeseries of the Den Helder and Vlieland haven measuring stations is also underestimated. The tidal range is captured fairly accurately at the Harlingen, Kornwerderzand, and Den Oever measuring stations, which are located farthest into the tidal Wadden Sea tidal basins. For these water levels to be accurate while starting off with an underestimated tidal range in the North Sea, the bottom roughness in the Wadden Sea must be lower than what it should be when the North Sea has the correct tidal range.

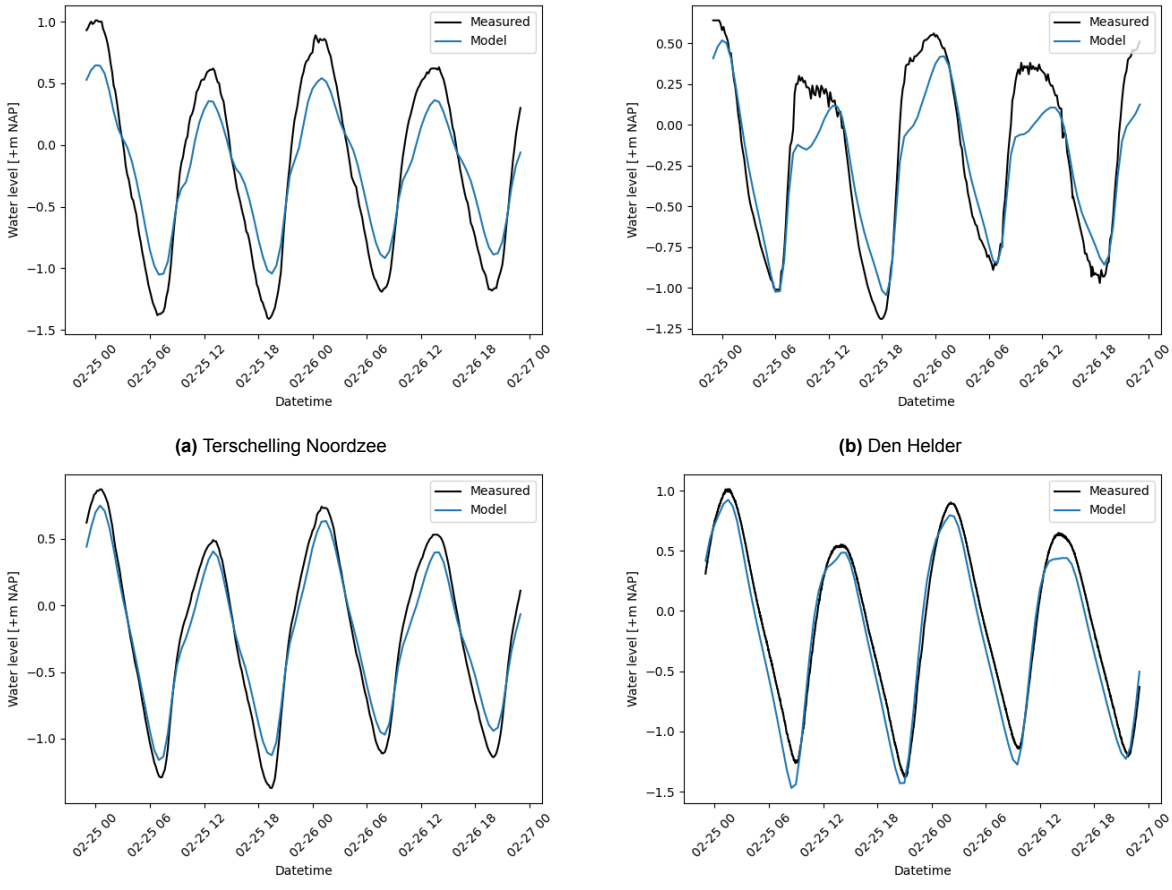

(a) Terschelling Noordzee

(b) Den Helder

(c) Vlieland haven

(d) Harlingen

Figure F.2: Simulated and measured water level timeseries without wind forcing at several measuring stations.

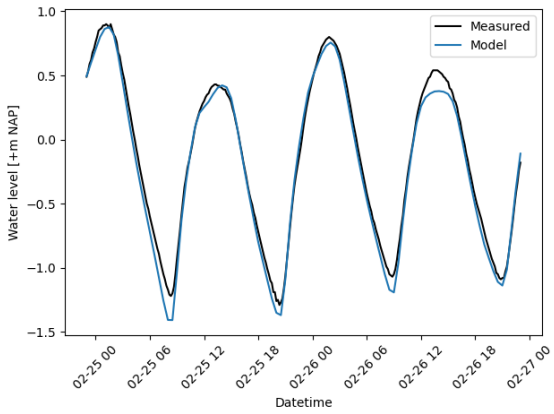

(e) Kornwerderzand buiten

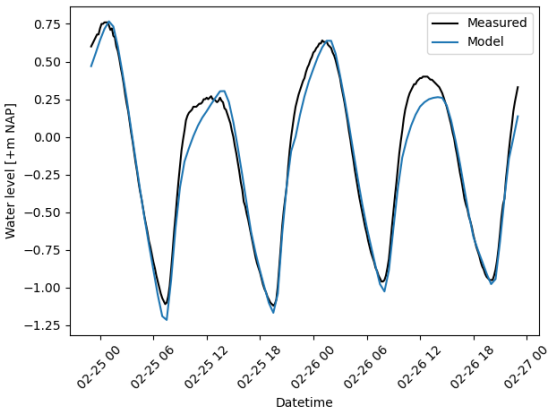

(f) Den Oever buiten

Figure F.2: Simulated and measured water level timeseries without wind forcing at several measuring stations (continued).

In the second calibration stage, the wind drag coefficient was calibrated during a period with windy conditions. The period of January 12th to January 18th was chosen. This is the week with the largest wind velocity in the 2019 wind record. The average velocity over this period was 11.8 m/s (Figure F.3). The wind direction was predominantly westerly. Westerly winds cause water level set-up in the Dutch Wadden Sea (Duran-Matute et al., 2016). The water level timeseries using different wind drag coefficients are shown at the Harlingen measuring station (Figure F.4). As this measuring station is located far into the Wadden Sea, wind has a pronounced effect on water levels. The main consequence of increasing the wind drag coefficient is that water levels are elevated. There is also a minimal shift in the timing of High Water (HW) and Low Water (LW).

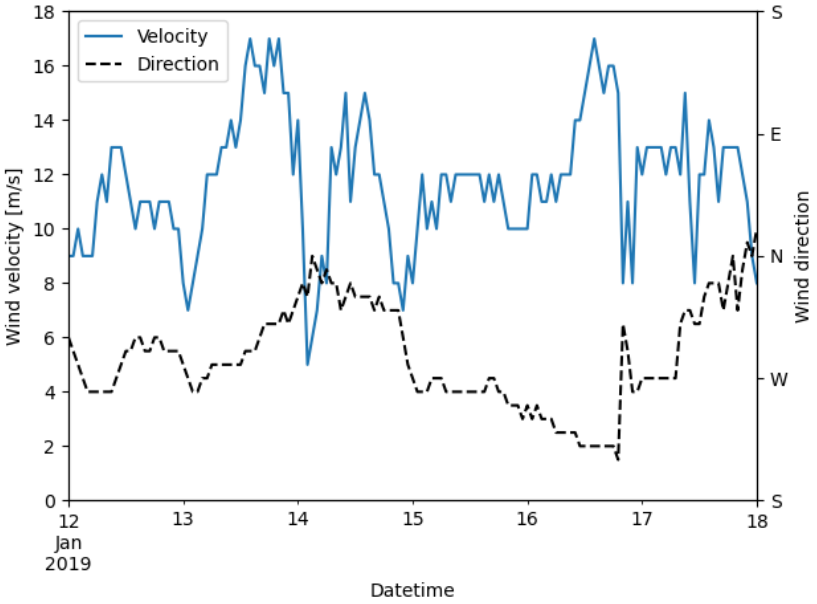

Figure F.3: Wind velocities and directions during the calibration phase with wind.

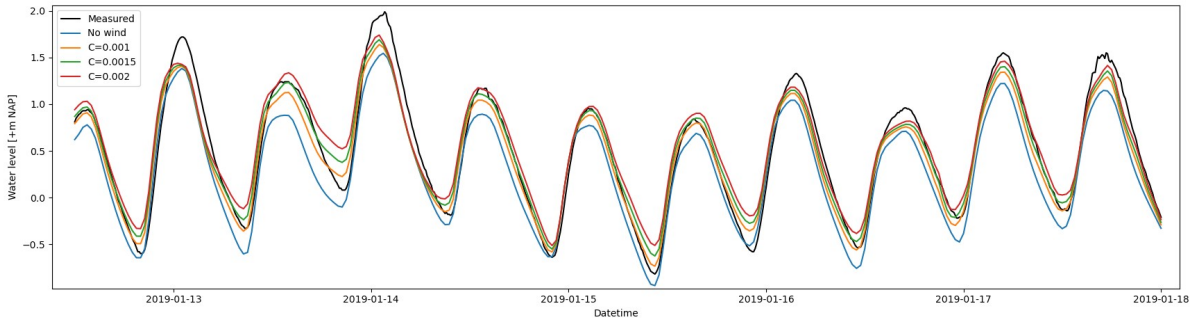

Figure F.4: Measured and simulated water level timeseries at the Harlingen measuring station for several different wind drag coefficients.

The performance of different wind drag coefficients is assessed using the Kling-Gupta Efficiency (KGE):

$$KGE = 1 - \sqrt{(r-1)^2 + (\gamma-1)^2 + (\beta-1)^2} \tag{F.4}$$

with:

r	correlation coefficient	[-]
γ	variability	[-]
β	bias	[-]

β is defined as:

$$\beta = \frac{\mu_s}{\mu_o} \tag{F.5}$$

with:

μ_s, μ_o	mean of simulated, measured timeseries	[m]

γ is defined as:

$$\gamma = \frac{\sigma_s}{\sigma_o} \tag{F.6}$$

with:

σ_s, σ_o	standard deviation of simulated, measured timeseries	[m]

The KGE metric tests how well a simulated signal represents an observed signal based on the correlation, variability, and bias criteria. The closer a value is to 1, the closer the simulated signal is to the observed signal. The KGE scores of Den Helder and Harlingen are decomposed (Figure F.5). At Harlingen, a wind drag coefficient of C = 0.0015 scores highest. The correlation and variability are comparable across the three different simulations. However, C = 0.0015 scores best, as the mean of the simulated water levels is close to the mean of the measured water levels. The scores of the C = 0.001 and C = 0.002 simulations are lower due to (respectively) a structural underestimation ($\beta < 1$) and structural overestimation ($\beta > 1$) of water levels. At Den Helder, the measured timeseries for C = 0.002 scores better than the water level timeseries for C = 0.0015 and C = 0.001 (Figure F.5a). The three simulations show comparable variability and correlation. All three simulations structurally underestimate water levels. The highest wind drag coefficient of C = 0.002 increases water levels more than the other wind drag coefficients. This leads to the highest KGE score. When interpreting the KGE metric, it is important to remember that the wind drag coefficient is not the only variable upon which system behavior depends. Compensating a water level underestimation caused by the chosen bottom roughness profile by overestimating the wind drag coefficient can worsen the overall simulated behavior.

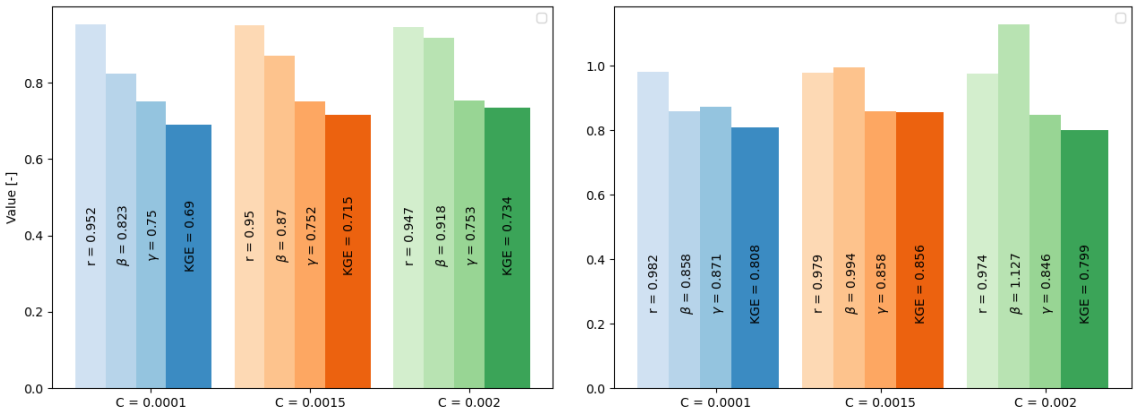

(a) Den Helder **(b)** Harlingen

Figure F.5: Decomposition into correlation, bias, and variability of the KGE scores at two measuring stations.

The sum of KGE scores over all measuring stations is shown in (Figure F.6). The sum of scores is highest for C = 0.0015. When only considering the measuring stations in the western Dutch Wadden Sea, the sum of scores for C = 0.0015 is highest as well. The value of C = 0.0015 is adopted for the wind drag coefficient.

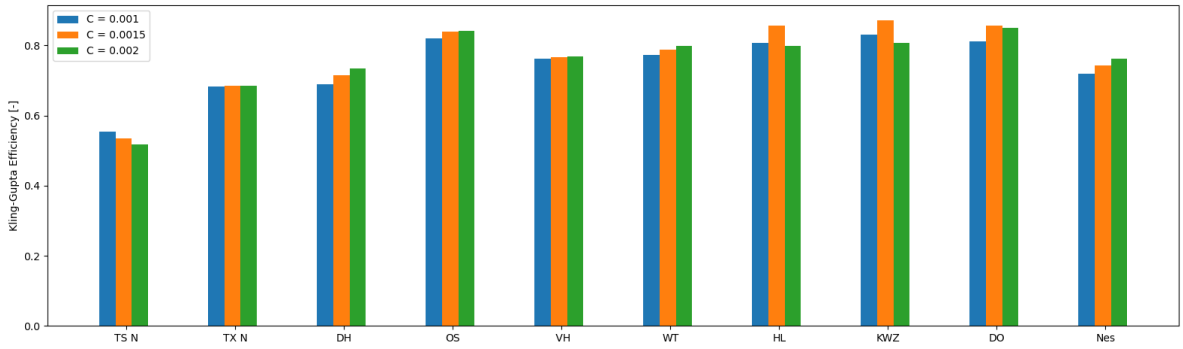

Figure F.6: KGE scores for wind drag coefficients C = 0.0005, C = 0.001, and C = 0.0015. Considered measuring stations are (from left to right) Terschelling Noordzee (TS N), Texel Noordzee (TX N), Den Helder (DH), Oudeschild (OS), Vlieland Haven (VH), West-Terschelling (WT), Harlingen (HL), Kornwerderzand (KWZ), Den Oever (DO), and Nes.

Due to the limited time scope of this project, the extent of the calibration was limited. It is very probable that bottom roughness maps exist for which water movement better represents reality. Short periods were used to calibrate the model. Possibly model parametrizations were chosen that show optimal performance during these periods, but that do not generalize well to the entire year of 2019. To increase the reliability of the calibration, it is advisable to calibrate for more periods and/or for longer periods.

G

Validation of large-scale water movement

The large-scale water movement of the hydrodynamic model was validated. A full description of the validation procedure is given in this appendix.

The model is validated for the first 6 months of 2019. This suffices, as model scenarios were subsequently formulated only during this period. The wind rose for this period is shown in Figure G.1. The wind climate during the validation period is comparable to the long-term wind climate in the Netherlands. The dominant wind direction is westerly to southwesterly.

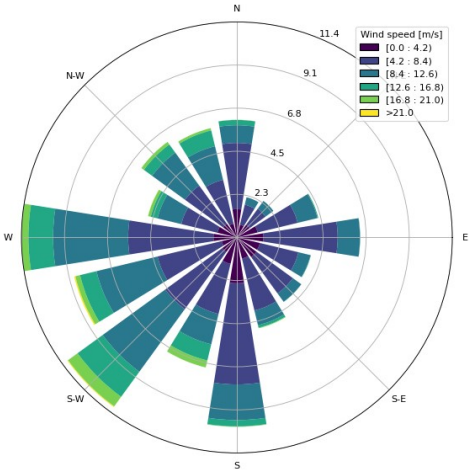

Figure G.1: Wind rose over the validation period 2019-01-01 to 2019-07-01. Labels indicate percentages.

The model is validated using two methods. A harmonic analysis is performed. However, harmonic analysis assumes that the tide consists entirely of the summation of tidal harmonic constants. This assumption is not entirely appropriate in a shallow area like the Wadden Sea, where wind-induced water level set-up and set-down affect the propagation of tidal constants (Duran-Matute et al., 2014). Therefore, the entire tidal signal is analyzed as well.

The M2 constituent is the most important constituent in the mainly semi-diurnal tide along the Dutch coast. The M4 and M6 constituents are the shallow-water constituents that arise from the M2 constituent. Non-linear tidal propagation generates the M4 constituent and friction generates the M6 constituent (Bosboom & Stive, 2021). The M2, M4, and M6 constituents of the simulated and measured water level timeseries were calculated using a harmonic analysis (Table G.1), and plotted in Figure G.2.

The relative amplitude deviation was calculated by dividing the amplitude difference by the average of the measured and simulated amplitude: $\frac{|a_{mea}-a_{sim}|}{\frac{1}{2}(a_{mea}-a_{sim})}$. The measured and simulated amplitudes are represented equally in the denominator through which the amplitude is normalized. This prevents results from becoming skewed if the amplitude of one of the signals is substantially larger than the amplitude of the other signal.

Table G.1: Harmonic analysis of M2, M4, and M6 tidal constituents in model and measured timeseries.

	M2				**M4**				**M6**			
	Measured		Model		Measured		Model		Measured		Model	
Location	A [m]	ϕ [deg]	A [m]	ϕ [deg]	A [m]	ϕ [deg]	A [m]	ϕ [deg]	A [m]	ϕ [deg]	A [m]	ϕ [deg]
Terschelling Noordzee	0.88	52.9	0.58	64.4	0.084	151.2	0.066	171.1	0.048	247.2	0.038	210.0
Texel Noordzee	0.76	10.2	0.52	25.4	0.095	53.0	0.062	55.3	0.079	172.6	0.071	160.8
Den Helder	0.64	9.0	0.48	29.5	0.102	41.1	0.084	33.5	0.057	168.3	0.047	155.3
Oudeschild	0.62	33.4	0.56	46.5	0.088	71.8	0.075	68.4	0.041	204.3	0.034	195.6
Vlieland haven	0.78	57.2	0.64	64.0	0.048	134.5	0.027	154.9	0.048	234.2	0.040	223.5
West-Terschelling	0.77	71.0	0.67	71.1	0.056	146.9	0.034	148.4	0.045	265.5	0.042	247.1
Harlingen	0.82	97.2	0.80	91.0	0.115	266.4	0.117	247.7	0.041	31.8	0.056	18.2
Kornwerderzand	0.76	78.6	0.76	77.9	0.066	206.7	0.080	192.8	0.038	338.7	0.051	332.2
Den Oever	0.65	50.7	0.63	59.6	0.091	120.3	0.089	110.6	0.043	260.5	0.043	249.0
Nes	0.94	99.3	0.75	98.7	0.095	198.7	0.074	237.2	0.052	339.1	0.051	316.6

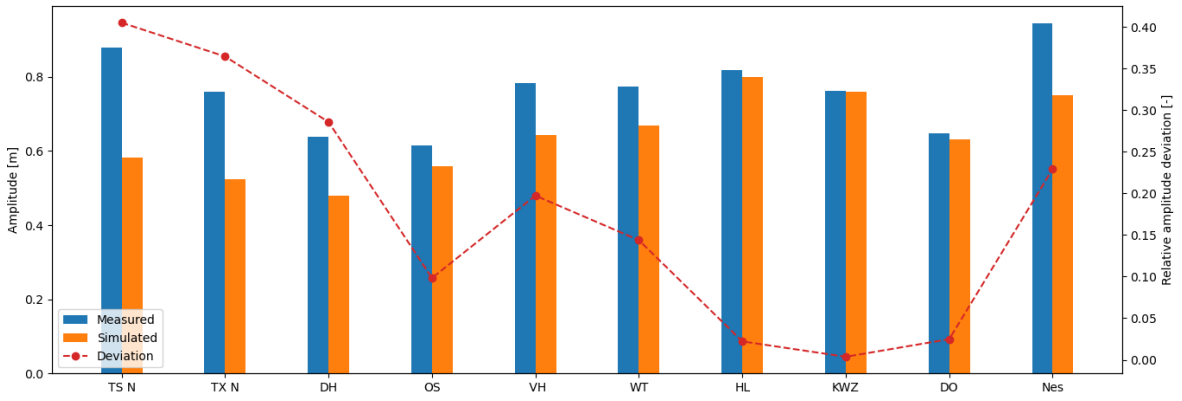

(a) M2 constituent.

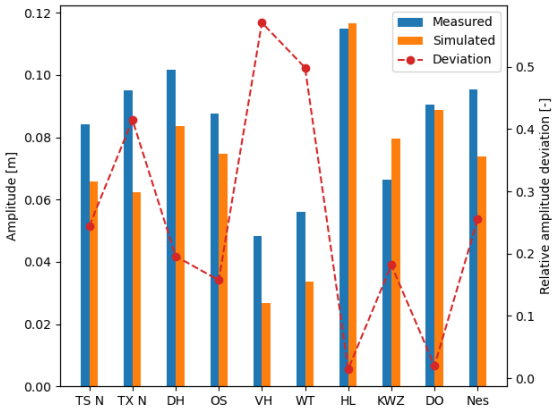

(b) M4 constituent.

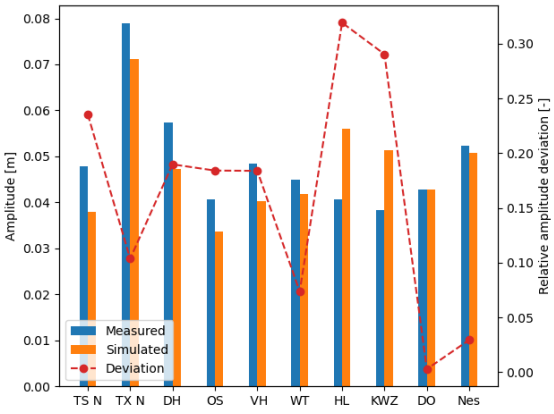

(c) M6 constituent.

Figure G.2: Relative amplitude deviation between the simulated and measured constituents M2, M4, and M6. Considered measuring stations are (from left to right) Terschelling Noordzee (TS N), Texel Noordzee (TX N), Den Helder (DH), Oudeschild (OS), Vlieland Haven (VH), West-Terschelling (WT), Nes, Harlingen (HL), Kornwerderzand (KWZ), and Den Oever (DO).

At measuring stations in the western Dutch Wadden Sea, the simulated M2 constituent generally deviates from the measured M2 constituent in the order of a single decimeter. The maximum deviation in the western Dutch Wadden Sea is 16 centimeters at the Den Helder measuring station. The deviation is larger in the North Sea, in the order of multiple decimeters. The maximum deviation of 30 centimeters occurs at the Terschelling Noordzee measuring station. Due to the close proximity to the North Sea, the underestimation of the M2 constituent in the North Sea leads to an underestimation of the M2 constituent at Den Helder and in the barrier island harbors. At the three measuring stations farther into the western Dutch Wadden Sea (Harlingen, Kornwerderzand, and Den Oever), the simulated M2 constituent is overestimated. The phase of the simulated signal is within 10 degrees of the measured signal at most measuring stations (Table G.1). However, there is a large deviation in the measured and simulated phase of the M2 constituent at Den Helder (20.4°) and Oudeschild (13.0°).

The amplitude of the M4 constituents generally follows the pattern of the M2 constituents. The M4 constituent is generated through non-linear propagation of the M2 constituent. Where the M2 constituent is underestimated, the M4 constituent is generally also underestimated. Deviations are in the order of centimeters. The M6 constituent is slightly underestimated in and near the North Sea. Farther into the western Dutch Wadden Sea, the M6 constituent is overestimated by up to 32%. This suggests that the underestimation of the M2 constituent in the North Sea is compensated by an overestimation of friction in the western Dutch Wadden Sea. Phase differences of the M4 and M6 constituents are larger than the phase differences of the M2 constituent.

The entire tidal signal is analyzed in addition to the harmonic analysis. A snapshot of the water level timeseries at the Vlieland haven measuring station is shown during March (Figure G.3a) and over the entire validation period (Figure G.3b). This location is chosen as the discrepancy between measured and simulated timeseries is average compared to all measuring stations, and the location in the Vlie basin is relevant for flow to the area of interest. The water level timeseries generally show good agreement with the measured water level timeseries. The model does a good job of capturing the wind-induced variability of water levels. This is exemplified by how water levels are elevated during the periods of March 4th - March 5th, March 13th - March 14th, and March 17th - March 19th.

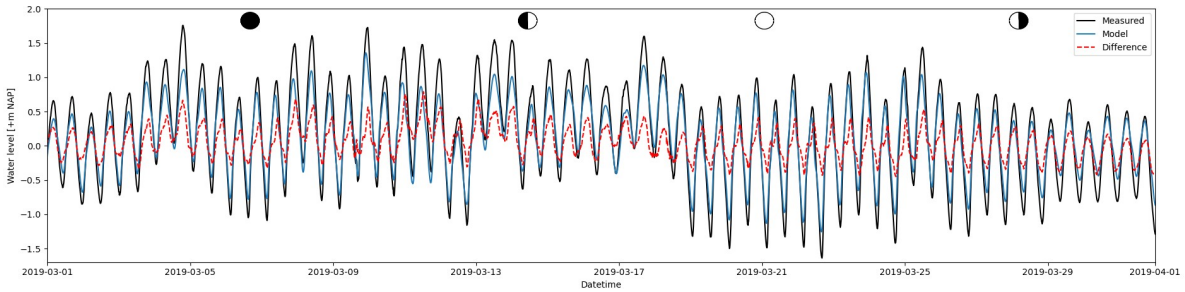

(a) March 1st - April 1st.

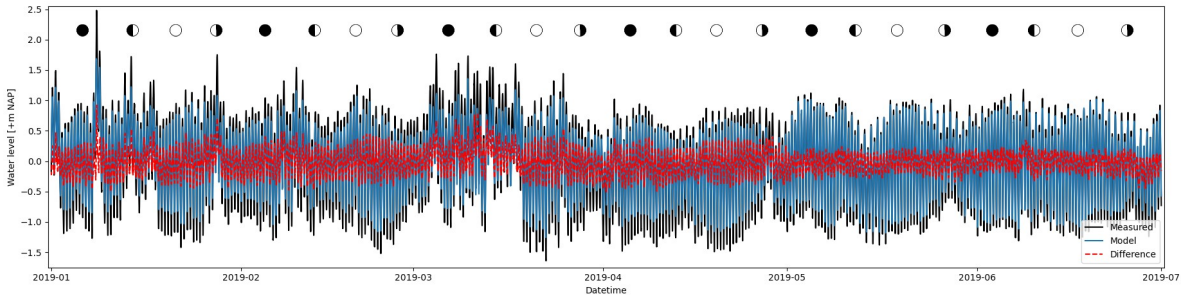

(b) The entire validation period.

Figure G.3: Measured and simulated water level timeseries at the Vlieland haven measuring station, and the difference between these. Shown over the entire validation period and in the month of March. Moon phases are shown to indicate the phase of the spring-neap tidal cycle.

There is a structural underestimation of the tidal range. Most High Water (HW) levels are not high enough, and Low Water (LW) levels are not low enough. The underestimation of tidal range worsens around neap tide. As can be seen from March 26th onward, especially the LW levels are overestimated around neap tides. The reason for this was not identified. During the validation period, the difference between simulated and measured water levels tends to structurally increase around neap tide at all measuring stations. Besides the underestimation of neap tidal ranges, no periods of structurally worse model performance were identified (e.g. during certain wind events).

Simulated water levels were found to be roughly within a single decimeter of the measured water levels in the western Dutch Wadden Sea. Towards the North Sea, model accuracy decreases. There is an underestimation of the tidal range in the North Sea. In the western Dutch Wadden Sea, this underestimation is compensated by lower bed friction compared than if the tidal range in the North Sea were correct.

H

Comparison of AT, NS, and HR scenarios

The impact of subgrid modeling technique on flow patterns on the scale of an intertidal flat is investigated. To do so, scenarios Higher-Resolution (HR), Average Tide (AT), and Interpolated Bathymetry (IB) are compared. The model schematizations of these scenarios differ in the area indicated in purple in Figure H.1. Outside of this area, model schematizations are identical. The hydrodynamics outside of the indicated area serve as a 'boundary condition' for hydrodynamics inside the indicated area. For a fair comparison between the three scenarios, the boundary condition should be consistent across the three scenarios. In this appendix, it is investigated how consistent this boundary condition is across the three scenarios.

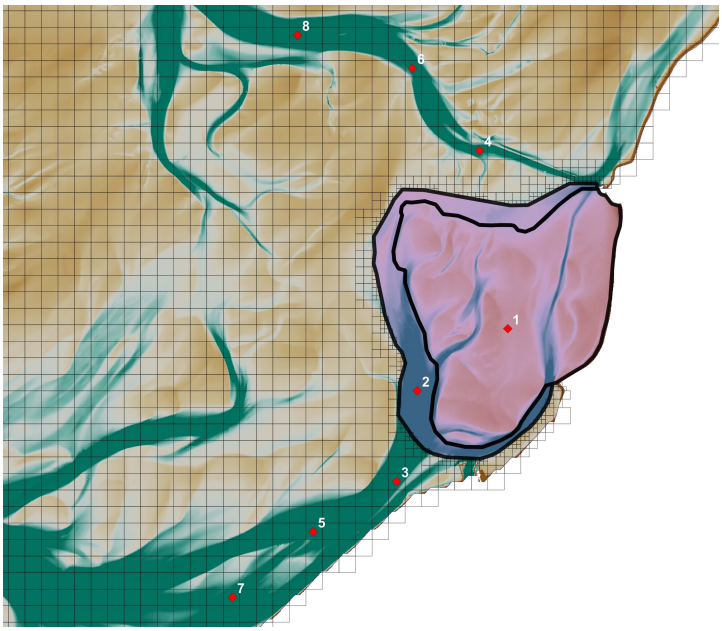

Figure H.1: Locations at which water level timeseries are compared. Area within which model schematizations differ indicated in purple. This area is divided into the intertidal flat area, and the area with tidal channels directly next to the intertidal flat which has a twice as large computational cell size. Computational grid indicated outside of the area in which model schematizations differ.

To investigate the consistency of the 'boundary condition', water level timeseries of the three scenarios are plotted at several points, along with the absolute difference in water levels. Average tidal conditions without wind forcing are simulated, as the comparison of flow patterns at the intertidal flat across the

three scenarios is performed during these conditions (chapter 4). Eight points are chosen (Figure H.1). Points 1 and 2 are placed in the area of interest, respectively on the intertidal flat and in a tidal channel. These points show the differences that occur in the area of interest. Points 4 to 8 are placed in the tidal channels leading up to the intertidal flat, as these play a significant role in dictating the hydrodynamics in the area of interest.

Large water level differences occur across the scenarios at point 1 (Figure H.2), which is on the intertidal flat in the area of interest. Several things stand out. At point 2, the differences $|\eta_{HR} - \eta_{AT}|$ and $|\eta_{HR} - \eta_{IB}|$ are comparable, indicating that the bed level averaging of the tidal channels directly next to the intertidal flat has only a minor effect on simulated hydrodynamics. Water level differences at all points from 2 to 8 are generally less than 1cm over the entire tidal cycle, except for a peak of roughly 2 cm during the rising tide. Compared to the differences that occur at the intertidal flat, these water level differences are relatively small. The differences between the water level timeseries decrease with distance from the intertidal flat (e.g. from point 3 to 5 to 7).

To conclude, hydrodynamics within the area of interest have a slight effect on the boundary condition that dictates the flow in the area of interest. However, the impact on water levels is relatively small, as it is in the order of a single centimeter and is small compared to the differences that occur between the scenarios at the intertidal flat. The boundary condition across the three scenarios is relatively consistent.

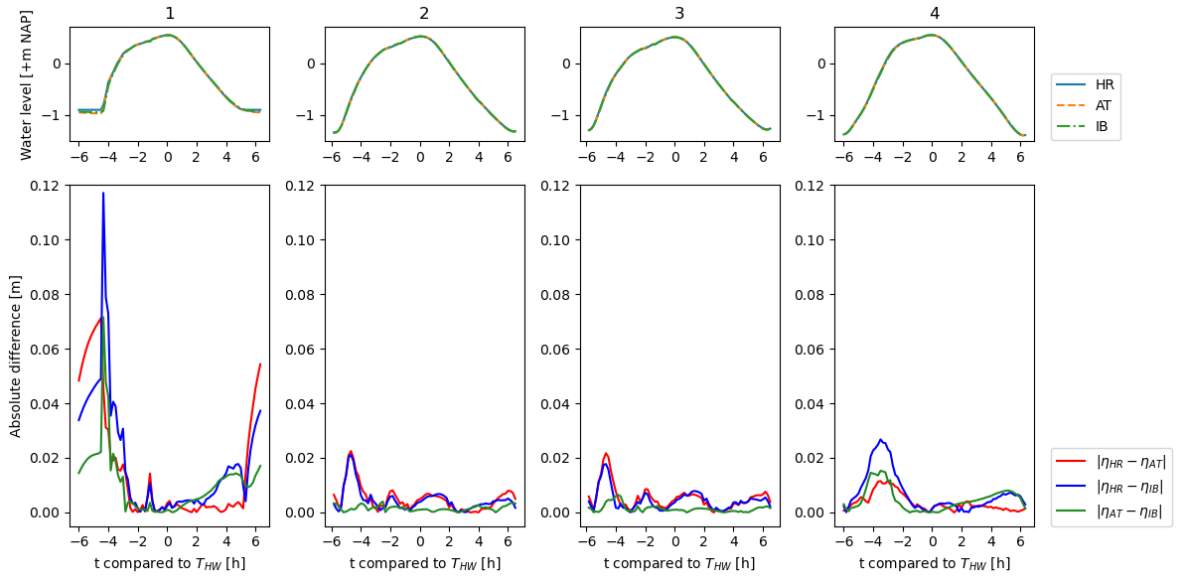

(a) Points 1 to 4

Figure H.2: Comparison of water level timeseries in scenarios HR, AT, and IB, along with differences between the timeseries. Locations indicated in Figure H.1.

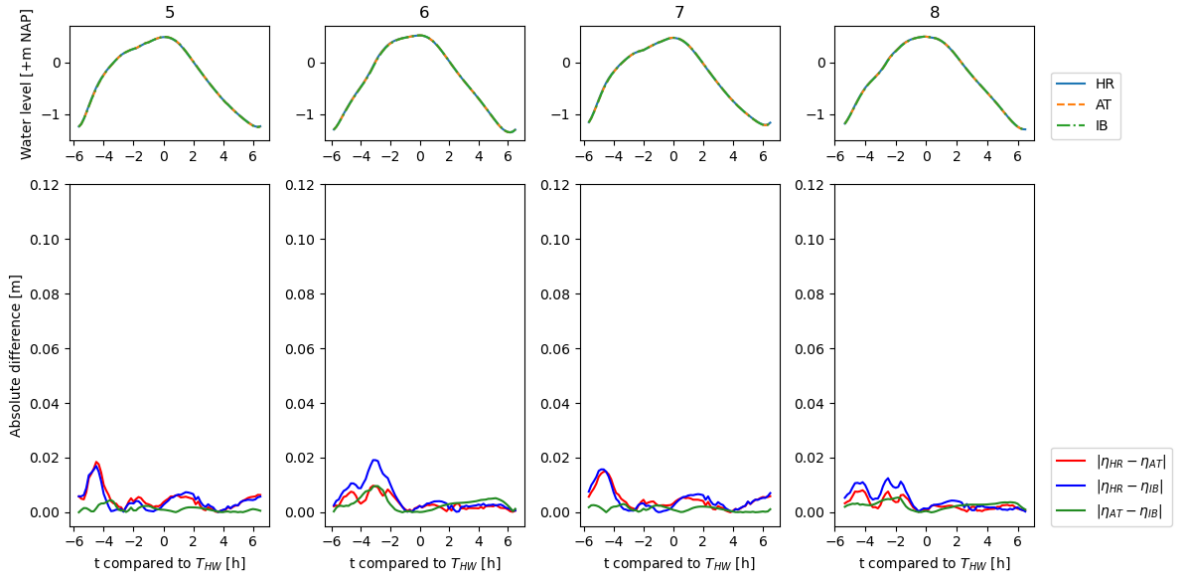

(b) Points 4 to 8

Figure H.2: Comparison of water level timeseries in scenarios HR, AT, and IB, along with differences between the timeseries. Locations indicated in Figure H.1 (continued).

I

Kornwerderzand spring-neap tidal cycle plots

In this appendix, spatial plots of velocities and water level differences compared to the mean water level in the domain are shown at the Kornwerderzand intertidal flat. Model outcomes of scenarios Spring Tide (ST) and Neap Tide (NT) are shown and compared to Average Tide (AT).

The spatial distribution of the water level gradients in ST (Figure I.2) is almost identical to that of AT (Figure 6.2). As a consequence, the direction of velocity vectors is very comparable to the direction of velocity vectors in AT. A problem arises when comparing the AT and NT tides. The NT water level timeseries is less asymmetrical in time than the AT water level timeseries (Figure I.3g). The tides are compared with the moment that High Water (HW) occurs as a reference point. This causes a misalignment between the tidal waves. The moment of Low Water (LW) differs by about an hour. It does not make sense to compare the velocities and water level gradients at different phases of the tidal cycle. The comparison between the AT and ST also suffers from this issue, but to a lesser extent as the tidal waves have a comparably asymmetrical shape.

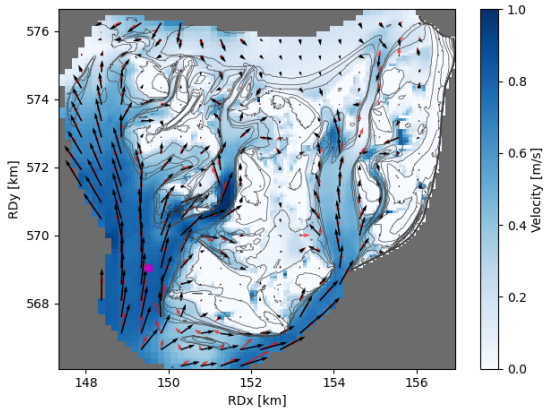

(a) t_1: Ca. 2 hours after LW.

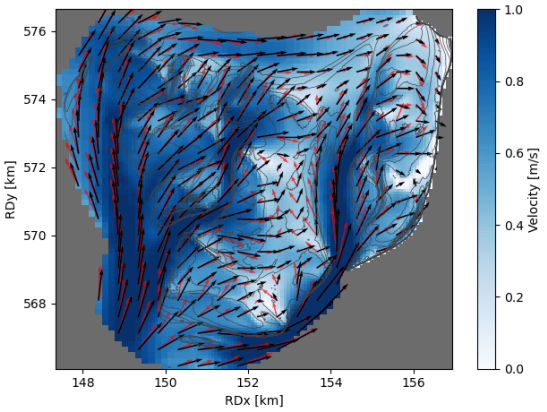

(b) t_2: Rising tide.

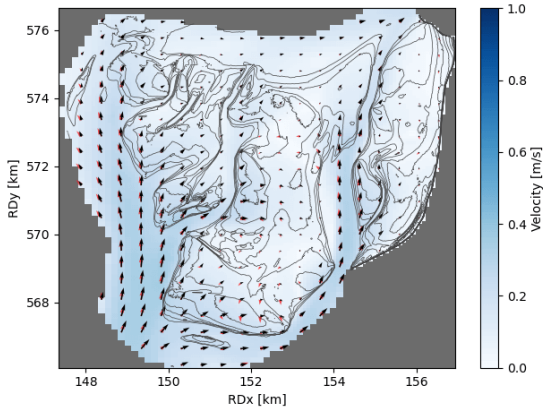

(c) t_3: Ca. 1.5 hours before HW.

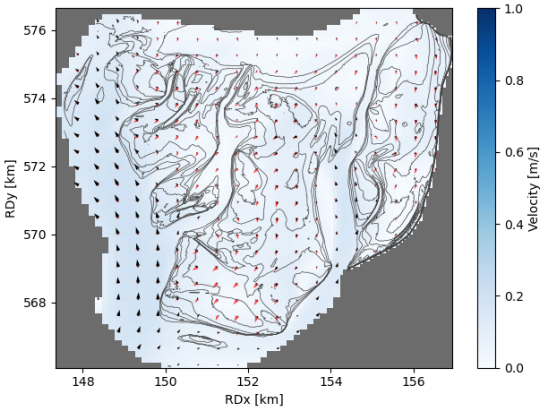

(d) t_4: High Water.

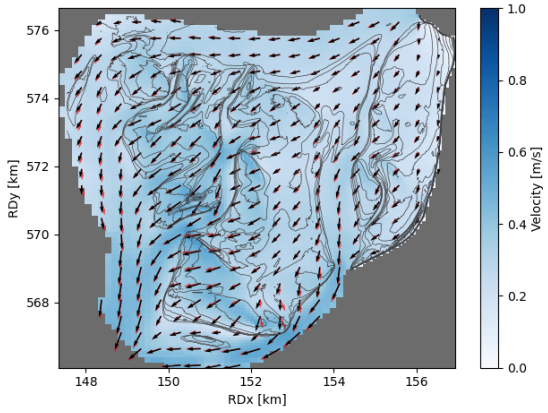

(e) t_5: Falling tide.

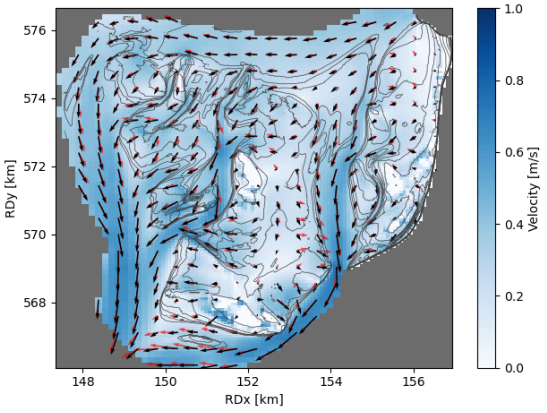

(f) t_6: Ca. 2 hours before LW.

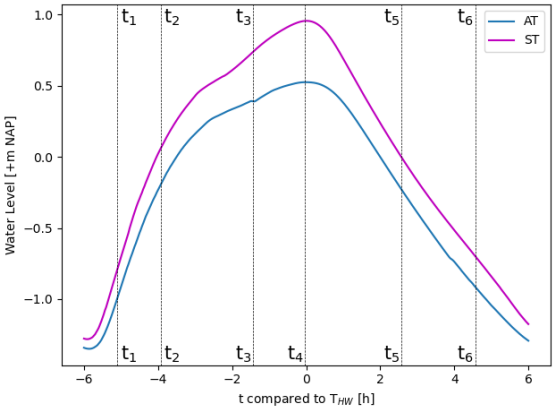

(g) Overview of instances in the AT and ST tidal cycle at which snapshots are shown. Location of water level timeseries indicated in subfigure a.

Figure I.1: Snapshots of vector velocities at the Kornwerderzand intertidal flat at different moments. Velocity vectors in reference scenario AT indicated in red; velocity vectors in ST indicated in black. Subfigure captions refer to tidal phases of AT.

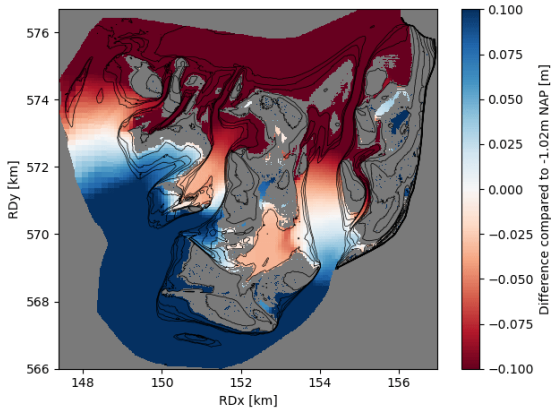

(a) t_1: Ca. 2 hours after LW.

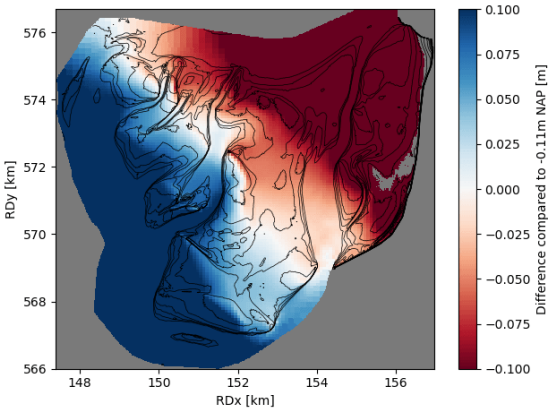

(b) t_2: Rising tide.

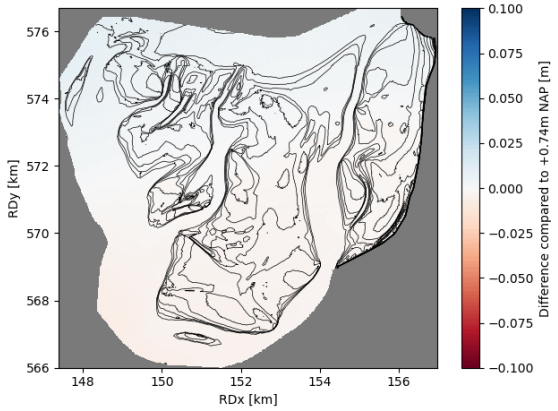

(c) t_3: Ca. 1.5 hours before HW.

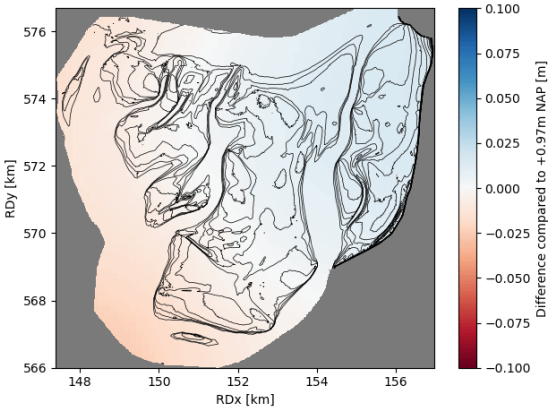

(d) t_4: High Water.

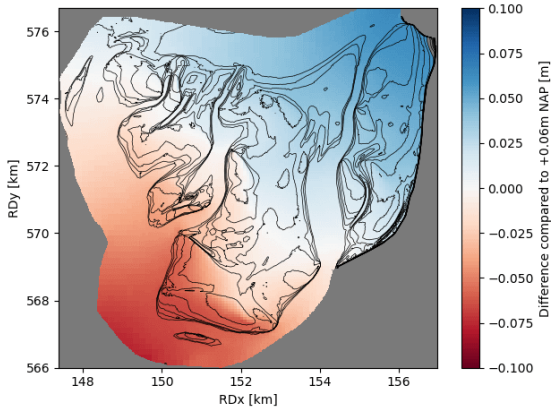

(e) t_5: Falling tide.

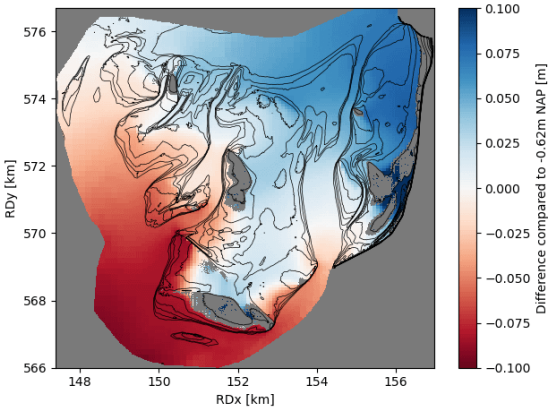

(f) t_6: Ca. 2 hours before LW.

Figure I.2: Snapshots of water level differences compared to the mean water level at the Kornwerderzand intertidal flat at different moments in ST. Figure I.1g gives an overview of the instances in the tidal cycle at which snapshots are shown. Subfigure captions refer to tidal phases of AT.

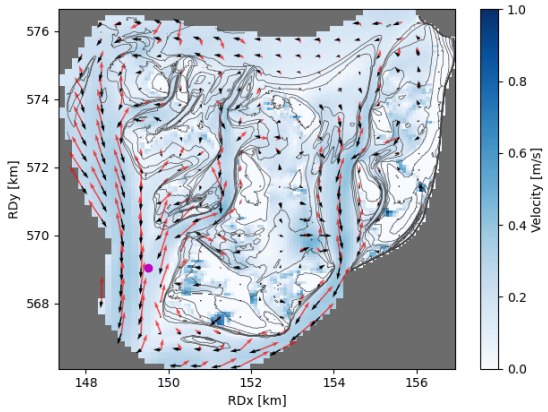

(a) t_1: Ca. 2 hours after LW.

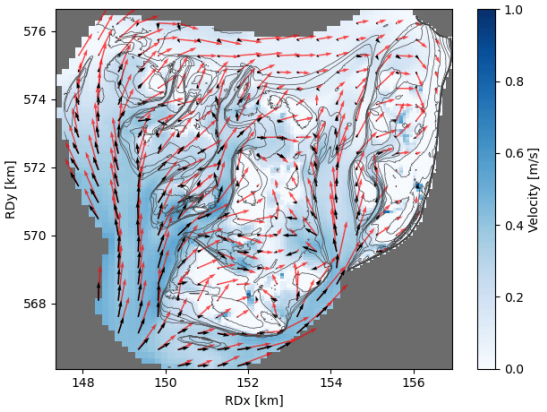

(b) t_2: Rising tide.

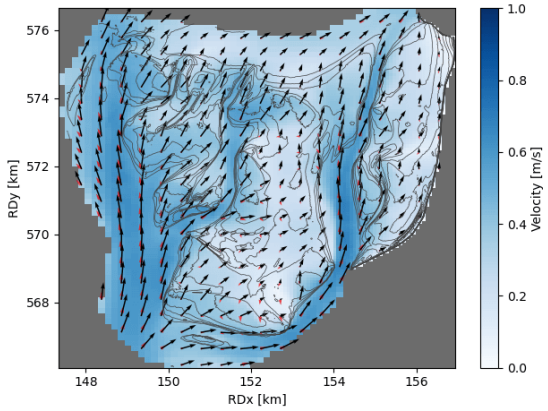

(c) t_3: Ca. 1.5 hours before HW.

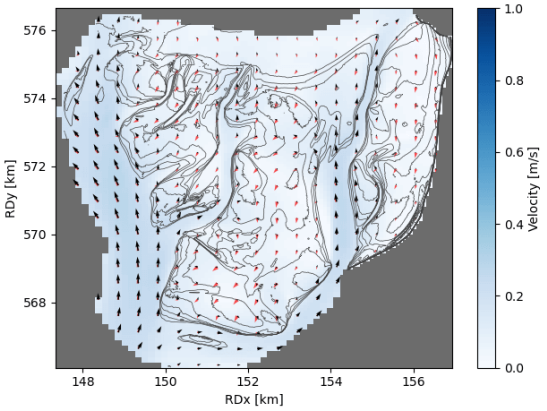

(d) t_4: High Water.

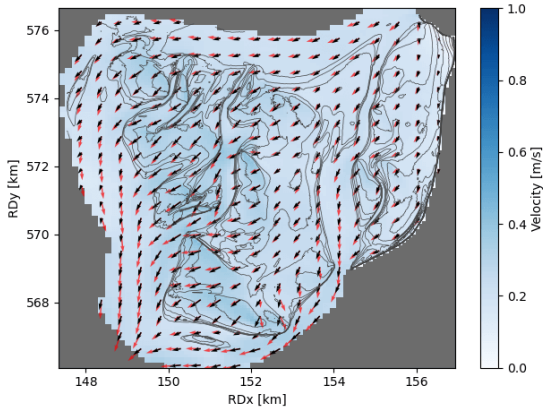

(e) t_5: Falling tide.

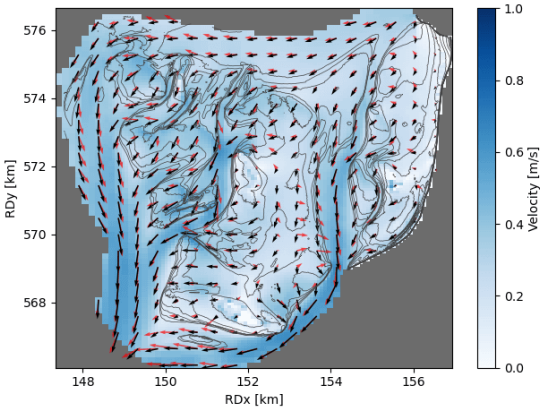

(f) t_6: Ca. 2 hours before LW.

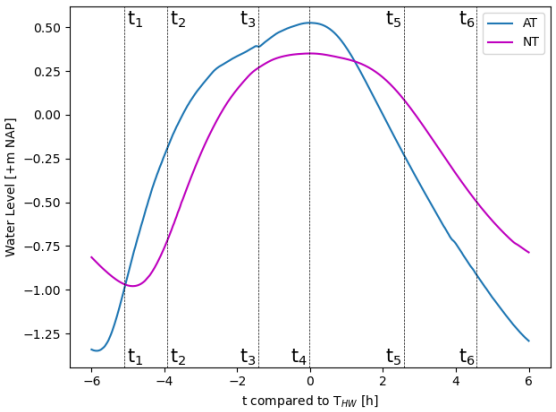

(g) Overview of instances in the AT and NT tidal cycle at which snapshots are shown. Location of water level timeseries indicated in subfigure a.

Figure I.3: Snapshots of vector velocities at the Kornwerderzand intertidal flat at different moments. Velocity vectors in reference scenario AT indicated in red; velocity vectors in NT indicated in black. Subfigure captions refer to tidal phases of AT.

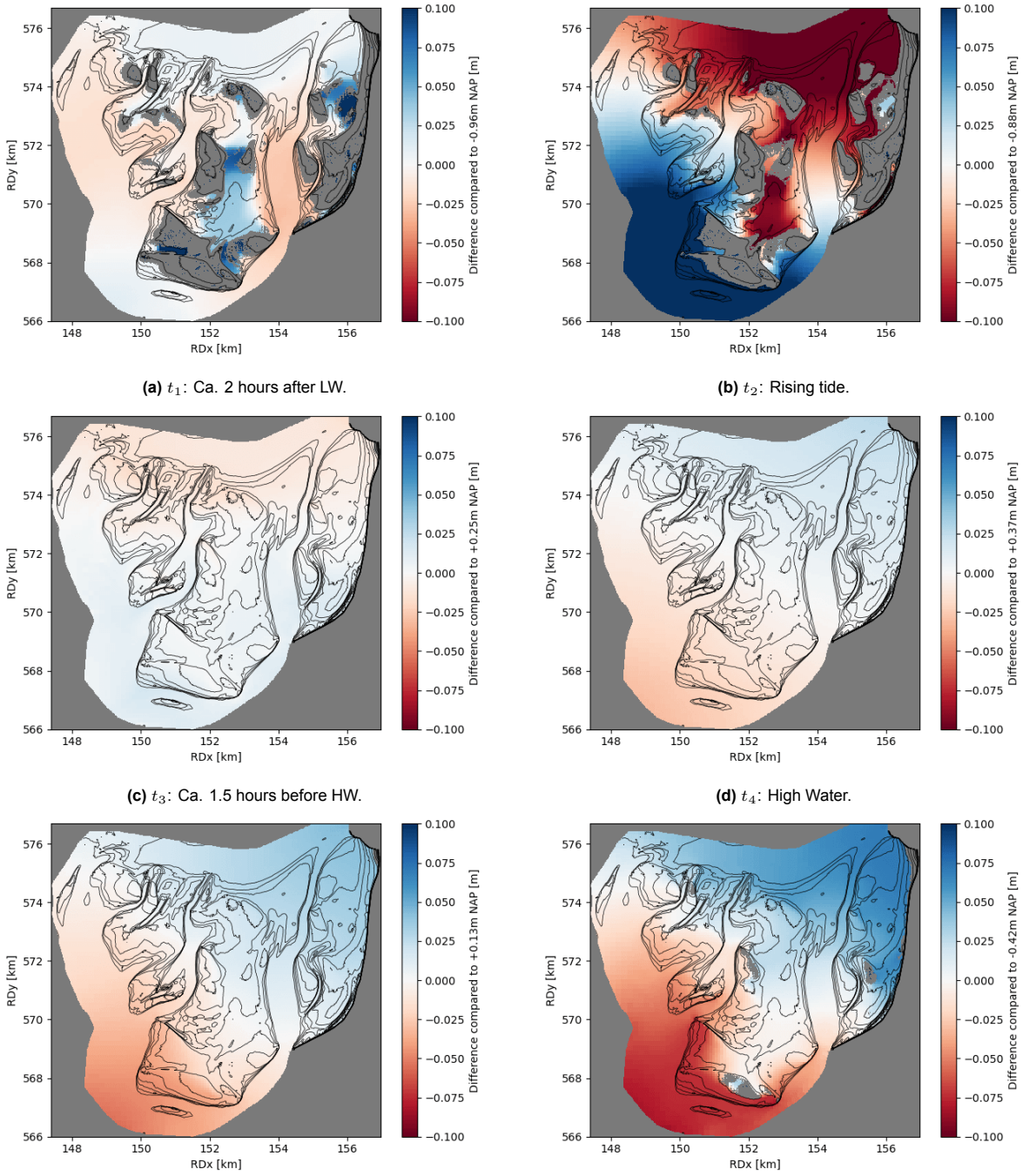

(a) t_1: Ca. 2 hours after LW.

(b) t_2: Rising tide.

(c) t_3: Ca. 1.5 hours before HW.

(d) t_4: High Water.

(e) t_5: Falling tide.

(f) t_6: Ca. 2 hours before LW.

Figure I.4: Snapshots of water level differences compared to the mean water level at the Kornwerderzand intertidal flat at different moments in NT. Figure I.3g gives an overview of the instances in the tidal cycle at which snapshots are shown. Subfigure captions refer to tidal phases of AT.

J

Detailed GBO flow patterns

In this appendix, the flow patterns at the Griend-Ballastplaat-vlakte van Oosterbierum (GBO) intertidal flats complex in absence of wind forcing are treated in more detail than in the main text. Scenarios Average Tide (AT), Spring Tide (ST), and Neap Tide (NT) are used. Specific discharges are tracked across several transects. Velocities at several measurement points are analyzed, and exposure times are shown. The influence of the spring-neap tidal cycle on specific discharges, velocities, water levels, and exposure times is analyzed.

To gain an understanding of the hydrodynamics at the GBO complex, several transects and measurement points are placed (Figure J.1). Transects are placed in several gullies (GBT2, GBT4, GBT5) and on the edges of the intertidal flat (GBT1, GBT3) to assess how the specific discharge varies. Non-zero specific discharges start flowing through GBT2 and GBT4 earlier than through GBT1 and GBT3 and keep flowing through these transects for longer. This again highlights the important role in conveying discharge onto the intertidal flat during flood, and off of the intertidal flat during ebb. The specific discharge through transect GBT5 is low, as this transect is located roughly in the middle where the flow from the north and south meet. The flow direction through the transect fluctuates.

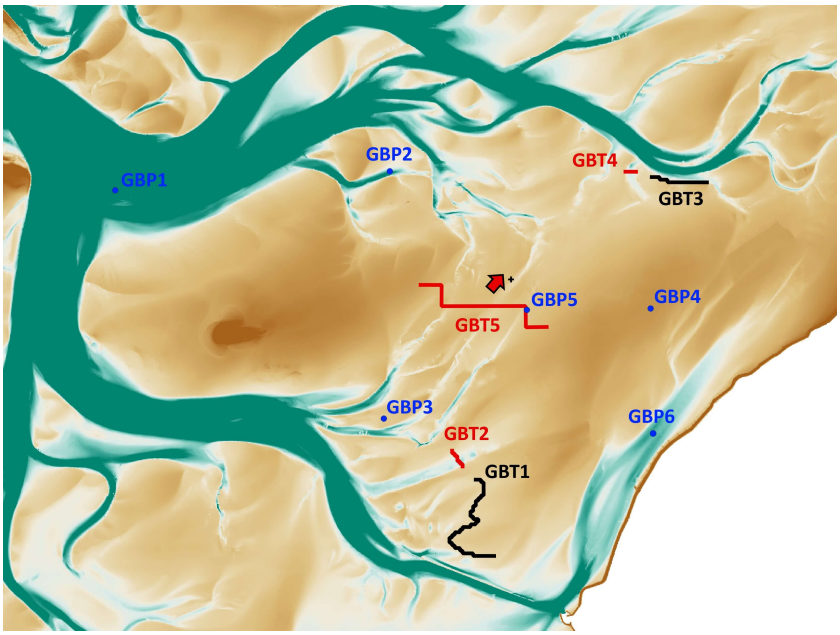

Figure J.1: Location at which transects and measurement points are placed. GBT1 and GBT3 placed at the MLW[1] contour. GBT2 and GBT4 placed in a gully. GBT5 placed at the approximate location where flow from the north and south meet. Flow onto the intertidal flat defined as positive.

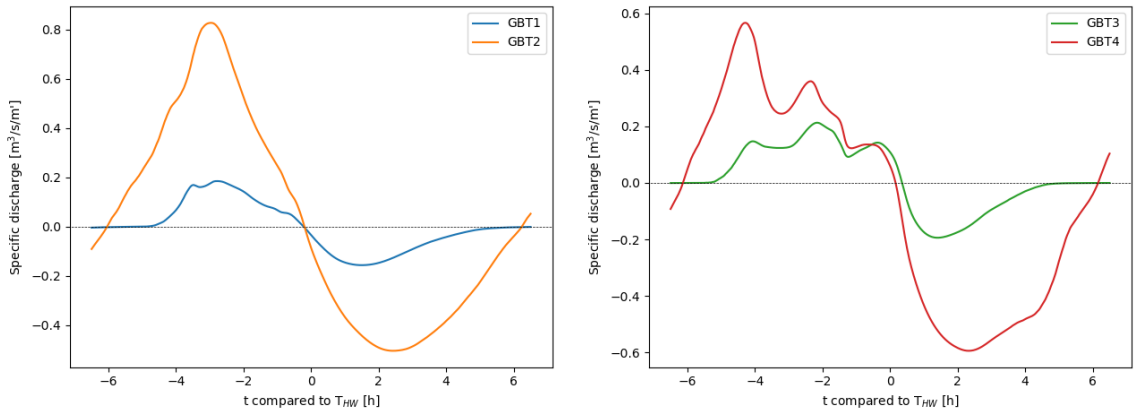

(a) Southern edge transect GBT1 and southern gully transect GBT2. **(b)** Northern edge transect GBT3 and northern gully transect GBT4.

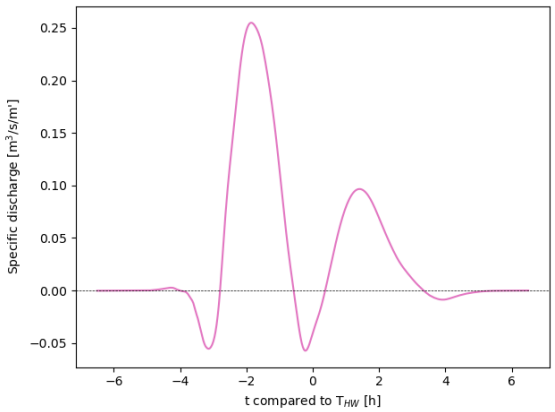

(c) Middle gullies transect GBT5.

Figure J.2: Discharge through several transects at the GBO complex in AT. Exact locations indicated in Figure J.1.

To study how velocities differ over the complex, velocity, and water level points are placed on the lower intertidal flat (GBP3), the upper intertidal flat (GBP4), and the lower intertidal flat where flow from the north and south converges (GBP5). The overall velocities are largest at GBP3, on the lower intertidal flat. Here, there are again four velocity peaks; just after inundation, during the maximal rising rate of the tide, during the maximal falling rate of the tide, and just before drying. Velocity peaks at GBP5 are somewhat lower, as this location inundates from two directions and drains in two directions. Velocities at GBP4 are markedly lower due to its higher elevation. At the moment that GBP4 inundates, the rate at which the tide rises is smaller than when GBP3 inundates. GBP4 dries before the maximal falling rate of the tide. Because the rising and falling rates at GBP4 are small, water level gradients and subsequently flow velocities are smaller than at GBP3.

[1]Average LW at the Harlingen measuring station over the validation period (-1.03m NAP).

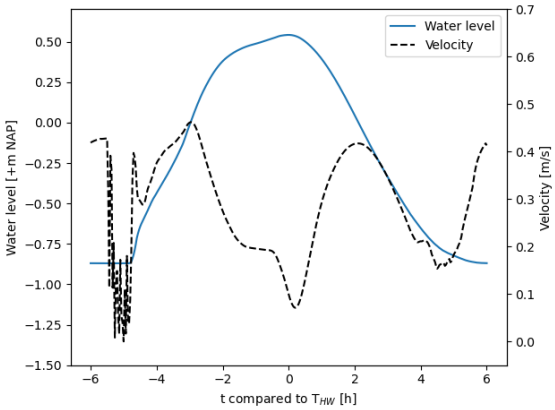

(a) Lower intertidal flat location GBP3.

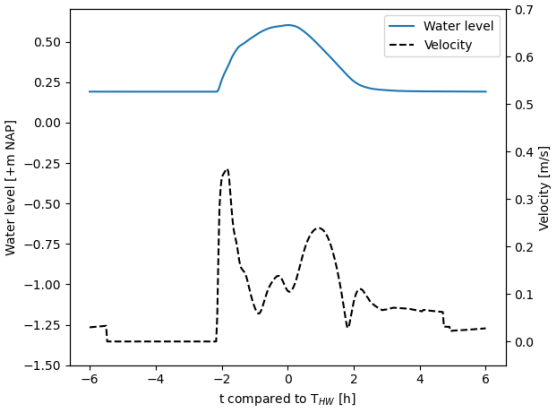

(b) Upper intertidal flat location GBP4.

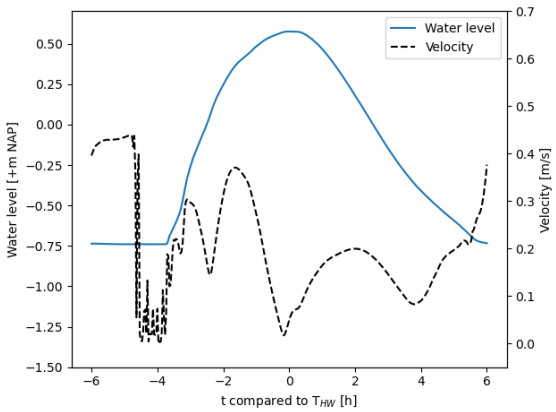

(c) Middle lower intertidal flat location GBP5.

Figure J.3: Water levels and velocities at several points on the GBO complex in AT. Exact locations in Figure J.1.

The exposure times at the GBO complex in AT are shown in Figure 6.6a. At the GBO complex, exposure times are longer than at the Kornwerderzand intertidal flat due to the higher bed elevations of the GBO complex. The highest elevations on the Grienderwaard do not inundate, while the highest elevations on the vlakte van Oosterbierum are exposed for roughly 8 hours. The relationship between exposure time and bed elevation is investigated to assess to what extent exposure time depends on the detailed flow patterns. Figure J.4b shows a scatter plot of the elevation of all 20mx20m bed pixels and their respective exposure times. Both the GBO complex and the Kornwerderzand intertidal flat are shown. There is a larger scatter in the data of the GBO complex. Water levels differ more strongly over the GBO complex than at the Kornwerderzand intertidal flat, as the GBO complex stretches from the coast to near the tidal inlet while the Kornwerderzand is a relatively small part of its tidal basin. This probably causes the larger spread in the exposure times of the GBO complex. Estimating exposure times at the GBO complex with a rigid lid approach would result in even less accurate exposure times than at the Kornwerderand intertidal flat. To accurately estimate exposure times at larger intertidal flat complexes, the need for simulations that resolve the detailed flow pattern is even stronger than at smaller intertidal flat complexes.

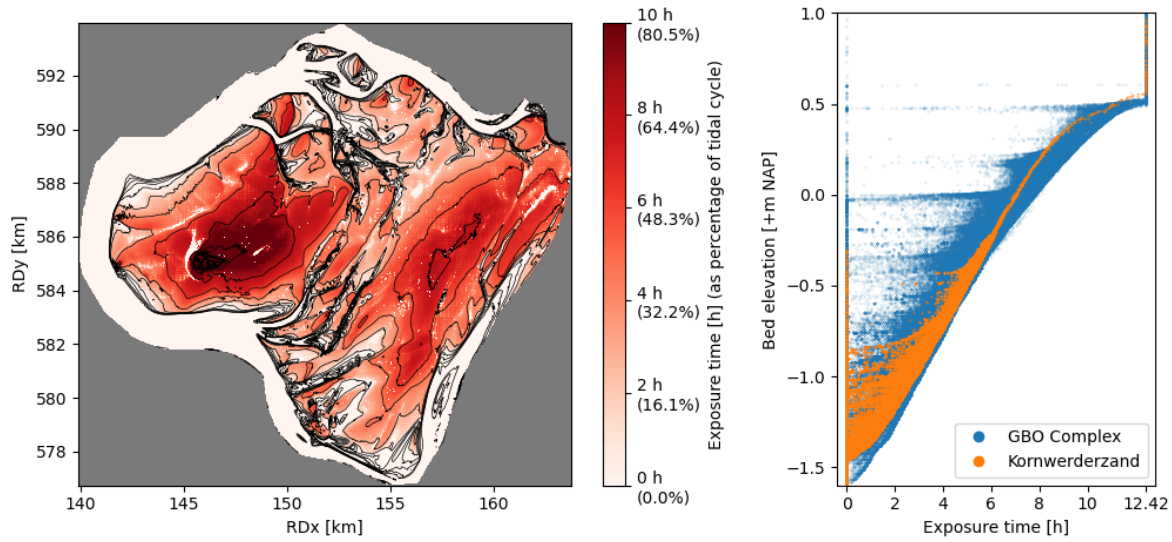

(a) Exposure time.

(b) Scatter plot.

Figure J.4: Exposure time and scatter plot of exposure time against bed elevation at the GBO complex in AT.

J.1. Spring-neap tidal cycle

Water levels in ST, AT, and NT are shown at locations GBP1 and GBP6 (Figure J.1) in Figure J.5. In all three simulations, the water level timeseries at GBP1 are relatively symmetrical in time. This location is close to the tidal inlet. The water level timeseries at GBP6 differ in how asymmetrical they are in time. This shows there is a difference over the spring-neap tidal cycle in how the tidal flood wave deforms further into the tidal basin. The discharge through transects GBT1 and GBT2 is shown in Figure J.6. There seems to be a relationship between the specific discharge peaks through a transect and the High Water (HW) level of the tide in which it occurred (Figure J.5), similar to the Kornwerderzand intertidal flat and in de Vet et al. (2018).

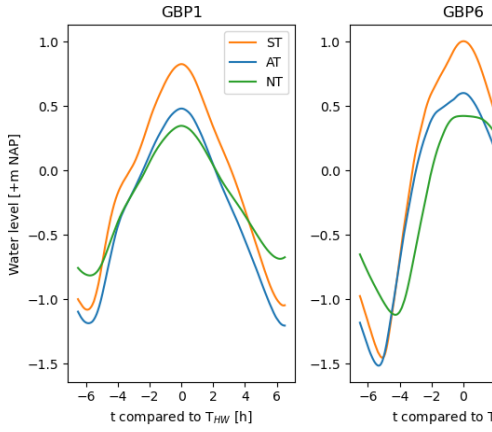

Figure J.5: Water levels in ST, AT, and NT at GBP1 and GBP6 (see Figure J.1 for location).

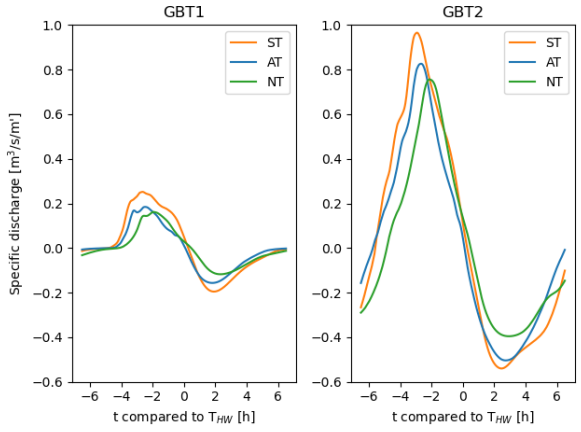

Figure J.6: Specific discharges through southern edge transect GBT1 and southern gully transect GBT2 in ST, AT, NT. (see Figure J.1 for location).

The difference in exposure time of NT and ST compared to AT are shown in Figure J.7a and Figure J.7b. The lower elevations are exposed for a shorter period of time in NT due to the higher Low Water (LW) level. The higher elevations of the Grienderwaard and vlakte van Oosterbierum are exposed for a longer period of time in AT than in NT. This contrasts with findings at the Kornwerderzand intertidal flat in NT. This difference occurs because the highest GBO complex elevations exceed the HW level of NT, but the highest Kornwerderzand elevations do not exceed the HW level of NT. In ST, the exposure

time of the GBO complex almost uniformly decreases compared to AT. The difference is largest near Griend island, where intertidal flat elevations are too high to flood in AT.

To assess the impact of the neap-tidal cycle on the detailed flow pattern, water levels and velocities are tracked over the tidal cycle at several points (Figure J.7c). The velocity peaks corresponding to the rising tide in ST are larger than in AT. The velocity peaks corresponding to the falling tide in NT are smaller than in AT. The velocity plots of GBP3 and GBP4 again show that if the rate at which the tide rises or falls is larger, velocities increase. A decrease in the rate at which the tide rises or falls leads to decreased velocities. At GBP6, where velocities converge, this does not hold.

Apart from the major differences between the GBO complex and Kornwerderzand intertidal flat treated in the main text, some minor differences were identified in this appendix. Due to the larger water level differences at the GBO complex, there is a larger spread in exposure times. Furthermore, the impact of the spring-neap tidal cycle on exposure times differs from what was observed at the Kornwerderzand intertidal flat, due to the higher elevations of the GBO complex. Besides this, flow patterns at the GBO complex in absence of wind forcing behave very similarly to those observed at the Kornwerderzand intertidal flat.

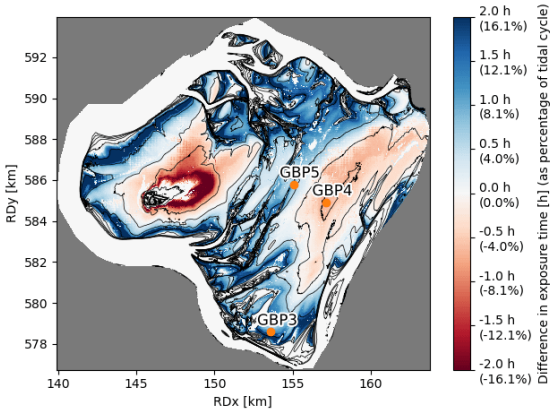

(a) Difference in exposure time between AT and NT. Positive values indicate AT has a longer exposure time. Subfigure c locations indicated for reference.

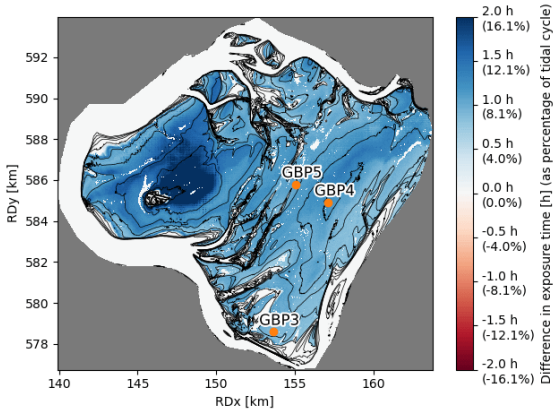

(b) Difference in exposure time between AT and ST. Positive values indicate AT has a longer exposure time. Subfigure c locations indicated for reference.

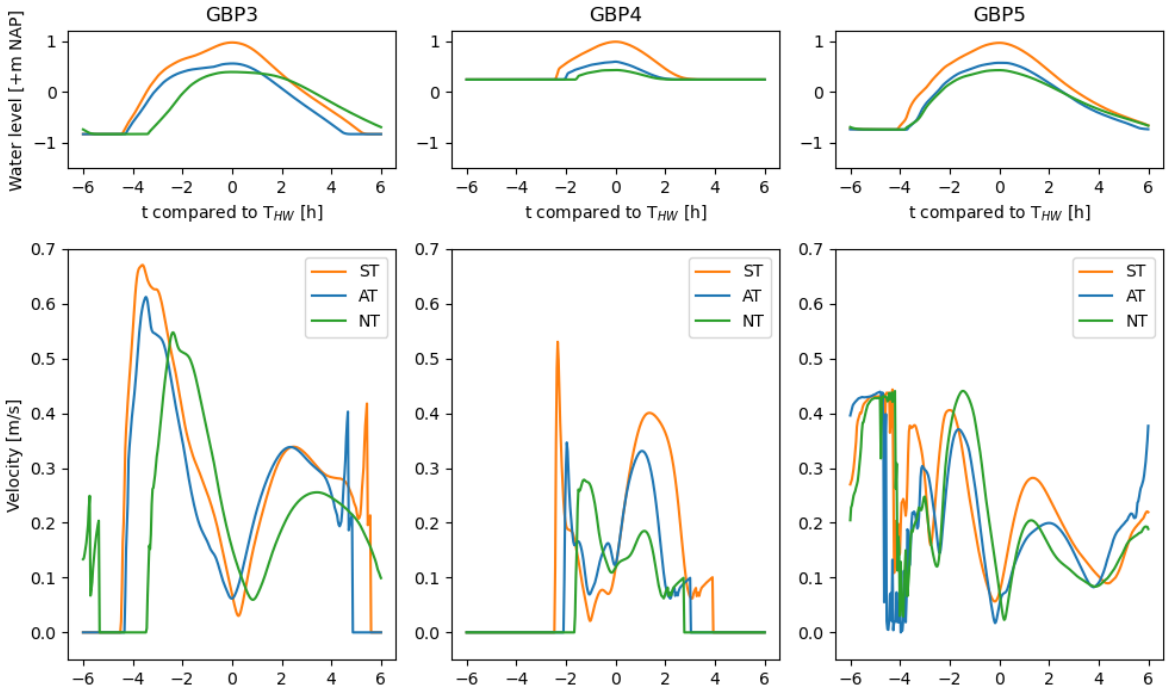

(c) Water levels and velocities at GBP3 (lower intertidal flat), GBP4 (upper intertidal flat), GBP5 (lower intertidal flat where flow from north and south converges) Locations indicated in subfigures a and b.

Figure J.7: Spatial differences in exposure time at the Kornwerderzand intertidal flat between (a) NT and AT, (b) as well as NT and AT, (c) along with point measurements of velocity and water level in ST, AT, and NT.